

Air-Coupled Ultrasound Inspection as a New Non-Destructive Testing Tool for Quality Assurance

Von der Fakultät Maschinenbau der Universität Stuttgart
zur Erlangung der Würde eines Doktor-Ingenieurs (Dr.-Ing.)
genehmigte Abhandlung

vorgelegt von
Dipl.-Ing. Rainer Stößel
geboren am 13.11.1970 in Bamberg

Hauptberichter: Prof. Dr. rer. nat. habil. G. Busse
Mitberichter: Prof. Dr. I. Yu. Solodov
Tag der mündlichen Prüfung: 01. September 2003

Institut für Kunststoffprüfung und Kunststoffkunde
der Universität Stuttgart

2004

Acknowledgements

Many persons contributed directly or indirectly to the successful completion of this study, which was completed while I was working for the Institute for Polymer Testing and Polymer Science (IKP) in the department of Non-Destructive Testing (ZfP) at the University of Stuttgart.

First I give special thanks to Prof. Dr. rer. nat. habil. Gerd Busse, head of the ZfP department, who supported this study in many ways. Among other things, he provided very helpful scientific discussions, ideas, the freedom of scientific work, his trust, and his personal support. He also gave a valuable critical review of the thesis. It is a great pleasure and honour to have worked for him and with him because he always stands behind his PhD students.

Next I give special thanks to Prof. Dr. Igor Yu. Solodov, Moscow State University and visiting professor at the University of Stuttgart, for the great support. He provided very valuable input in the field of non-linearity and was the second reviewer of the thesis which I appreciate very much as well as his collegiality.

Another big thanks goes to my colleagues at the IKP and especially those in the department of Non-Destructive Testing. Both the scientific interaction and the personal time together are unforgettable. A special appreciation goes to Dr.-Ing. Nils Krohn and Dipl.-Ing. Klaus Pfeleiderer, my two office mates, for their friendship and support in many ways.

The personal support of many people in the Stuttgart and Bamberg areas contributed immensely to the successful completion. Mr. Steffen Wolff, Juergen, and Brigitte Henkel are valued friends who provided support just by being there and providing companionship. Also Manfred and Inge Pfander were very kind and supportive friends. I want to thank Prof. Dr. Gary Cunningham, formerly professor at the Stuttgart Institute of Management and Technology, for many helpful discussions and assistance with the English language. I also appreciate the motivation he gave me.

Finally I would like to thank my mother Marga Stoessel for her support during the years.

Contents

CONTENTS	5
LIST OF ABBREVIATIONS AND ACRONYMS	8
ABSTRACT	12
KURZFASSUNG	14
1 INTRODUCTION	16
1.1 Quality assurance	16
1.2 Quality assurance and non-destructive testing	18
1.3 State of the art of non-destructive testing techniques	20
1.3.1 <i>Non-destructive testing using optical methods</i>	21
1.3.2 <i>Non-destructive testing using radiography and x-ray methods</i>	22
1.3.3 <i>Non-destructive testing using microwave methods</i>	23
1.3.4 <i>Non-destructive testing using thermal methods</i>	24
1.3.5 <i>Non-destructive testing using vibration methods</i>	26
1.3.6 <i>Non-destructive testing using ultrasound methods</i>	28
1.4 Scope of the thesis	29
2 LINEAR ACOUSTICS	32
2.1 Fundamentals of elastic theory	34
2.2 Wave propagation in liquids and gases	37
2.2.1 <i>Hydrodynamic equations</i>	38
2.2.2 <i>Equation of state for liquids and gases</i>	38
2.3 Wave equation for plane wave propagation	41
2.4 Reflection and transmission of waves at a plane boundary	42
2.5 Transmission of a normal incident wave through a plate	48
2.6 Matching layer	53
2.7 Acoustical attenuation	55
2.7.1 <i>Sound attenuation in gases and liquids</i>	55
2.7.2 <i>Sound attenuation and scattering in solids</i>	57
2.8 Focusing of ultrasound beams	59
3 NON-LINEAR ACOUSTICS	61
3.1 “Classical” non-linear acoustics	61
3.1.1 <i>“Classical” non-linear behaviour of gases and liquids</i>	61

3.1.2	<i>“Classical” non-linear behaviour of solids</i>	62
3.1.3	<i>Wave form distortion</i>	63
3.1.4	<i>Generation of higher harmonics</i>	64
3.2	“Non-classical” non-linear acoustics	65
3.2.1	<i>Normal traction driven interfaces</i>	66
3.2.2	<i>Tangential traction driven interfaces</i>	67
4	BASIC ULTRASOUND TESTING TECHNIQUES	70
4.1	Coupling media and coupling techniques	71
4.2	Reflection technique	73
4.3	Through-transmission technique	74
4.4	Scanning techniques and imaging of ultrasound signals	75
5	AIR-COUPLED ULTRASOUND INSPECTION METHOD	81
5.1	Fundamental considerations	81
5.2	Air-coupled ultrasound device	82
5.2.1	<i>Transmitting part of the equipment</i>	82
5.2.2	<i>Receiving part of the equipment</i>	85
5.3	Performing measurements with linear ACU inspection	87
5.4	Performing measurements with non-linear ACU inspection	93
6	APPLICATIONS	95
6.1	Wood	95
6.1.1	<i>Solid wood</i>	96
6.1.2	<i>Wood veneer sample</i>	100
6.2	Carbon Fibre Reinforced Plastic (CFRP)	100
6.2.1	<i>Impact Damage</i>	101
6.2.2	<i>Delamination</i>	108
6.2.3	<i>Repaired CFRP-structure</i>	111
6.3	Cure monitoring of epoxy resin and detecting disbonds in adhesive joints	112
6.4	Honeycomb sandwich structures	115
6.5	Multi-Layer Ceramics	117
6.5.1	<i>Monitoring the production process of C/C-SiC</i>	118
6.5.2	<i>Heterogeneous distribution of Si and SiC</i>	119
6.5.3	<i>Delaminations</i>	120
6.5.4	<i>Disbond</i>	121
6.6	Shape adaptive Structures – “Smart Structures”	122
6.6.1	<i>Detection of delaminations and structures in shape adaptive components</i>	123
6.6.2	<i>Detection of cracks in shape adaptive structures</i>	128
7	CONCLUSIONS AND IMPLICATIONS	131

7.1	Conclusions	131
7.2	Implications.....	134
8	REFERENCES.....	137

List of Abbreviations and Acronyms

<i>A</i>	amplitude
<i>a</i>	aperture radius [m]
<i>a</i>	middle-to-middle distance between the two rods
A/D	analog/digital
ACU	air-coupled ultrasound
a_{ex}	thermal expansion coefficient [1/K]
<i>AL, AB</i>	sound absorption in air and of the sample [dB]
<i>B</i>	non-linear bulk modulus of elasticity [N/m ²]
BE	back-wall echo or back surface reflection
C	carbon
<i>C</i>	elastic constant [N/m ²]
<i>c</i>	phase velocity [m/s]
C/C	carbon-carbon ceramic
C/C-SiC	carbon-carbon silicon carbide
c_0	velocity [m/s]
CAN	contact acoustic non-linearity
CFRP	carbon fibre reinforced polymer
<i>CL</i>	two-way transducer conversion loss [dB]
c_p	molar specific heat capacity of an ideal gas at constant pressure [J/(mol K)]
c_v	molar specific heat capacity of an ideal gas at constant volume [J/(mol K)]
<i>d</i>	distance [m]
DE	discontinuity echo or inclusion reflection
<i>DL</i>	diffraction losses in air [dB]
<i>E</i>	potential energy [eV]
<i>E</i>	energy [Nm], [J]
<i>E(t)</i>	excitation signal, driving signal
EC	European Community
EE	entry echo or front surface reflection
<i>EL</i>	“excess” propagation losses [dB]
ESPI	Electronic Speckle Pattern Interferometry
<i>f</i>	frequency [Hz], [1/s]
<i>F</i>	force [N]
F_a	attractive force [N]
f_f	focal length [m]
FMEA	Failure Mode and Effect Analysis
F_p	force [N] caused by pressure on a surface
F_r	repulsive force [N]
GFRP	glass fibre reinforced polymer

<i>I</i>	intensity [W/m ²]
<i>J_n</i>	<i>n</i> -th-order (first kind) Bessel function
<i>k</i>	wave number [1/m]
<i>K</i>	bulk modulus of elasticity [N/m ²]
<i>k</i>	Boltzmann's constant: $k = 1.3807 \cdot 10^{-23}$ J/K
<i>l_f</i>	length of the focal tube [m]
<i>m</i>	mass [kg]
<i>m</i>	ratio of two acoustical impedances
<i>M</i>	acoustic Mach number
<i>M₀</i>	amplitude Mach number
<i>n</i>	number of moles $n = 6.022 \cdot 10^{23}$ mol ⁻¹
<i>n</i>	natural number
<i>n</i>	empirical parameter of the TAIT equation
NDT	non-destructive testing
<i>NF</i>	"noise factor" (range 1-10)
NH ₃	ammoniacal gas
Ni	nickel
OLT	optical lockin thermography
<i>p</i>	pressure [Pa]
<i>P</i>	pressure [Pa]
<i>P_a</i>	available transmitter power [W]
PAD82	analogue-digital converter board
PMMA	polymethylmethacrylate
<i>Q</i>	heat [J]
<i>q</i>	cooling coefficient [1/s]
QMS	quality management system
<i>R</i>	universal gas constant: $R = 8.314 \cdot 10^{-3}$ J/(K kmol)
<i>R</i>	reflection coefficient
<i>r</i>	radius [m]
<i>R</i>	output loading resistance of the signal generator or amplifier [Ω]
<i>R</i>	radius of the curvature of a focused transducer [m]
<i>R_φ</i>	reflection coefficient (related to potential of particle velocity)
<i>R(t)</i>	response
<i>r₀</i>	equilibrium radius [m]
<i>r_f</i>	radius of the focal spot [m]
<i>R_I</i>	reflection coefficient (related to intensity)
<i>R_p</i>	reflection coefficient (related to pressure)
<i>R_v</i>	reflection coefficient (related to particle velocity)
<i>s</i>	ratio of densities
<i>S</i>	surface [m ²]
<i>S/N</i>	signal-to-noise ratio

Si	silicon
Si ₃ N ₄	silicon nitride
SiC	silicon carbide
SM	surrounding medium
SPC	statistical process control
T	absolute temperature [°K]
t	time [s]
T	transmission coefficient
T_I	transmission coefficient (related to intensity)
T_p	transmission coefficient (related to pressure)
T_v	transmission coefficient (related to particle velocity)
U	internal energy [J]
u	particle displacement [m]
U_B	binding energy [eV]
U_B	binding energy [eV/atom]
UBP	ultrasound burst phase thermography
ULT	ultrasound lockin thermography
v	particle velocity [m/s]
V	volume [m ³]
V	peak-to-peak voltage [V]
W	work [J]
x -	x-coordinate [m]
x_a	apparent width [m]
x_D	discontinuity distance [m]
x_t	true width [m]
y -	y-coordinate [m]
Z	acoustical impedance [kg/m ² s]
z -	z-coordinate [m]
Δf	effective bandwidth of the receiver electronics [Hz]

Greek letters

η	coefficient for inner friction (viscosity [Pa s], [Ns/m ²], [g/(ms)])
φ	potential of the particle velocity [m ² /s]
Θ	expansion of volume
γ	adiabatic exponent
δ_{ik}	Kronecker symbol ($\delta_{ik} = 1$ for $i = k$ and $\delta_{ik} = 0$ for $i \neq k$)
α	absorption coefficient [1/m]
α_r	absorption coefficient [1/m] related to inner friction
α_{st}	absorption coefficient [1/m] related to radiation of heat
β	rotation angle [°]
β_2	second-order acoustic non-linearity coefficient
ε	deformation, strain
ε^0	contact static strain [-]
ε_h	loss factor [-]
λ	wave length [m]
λ_s	wave length of the shear wave [m]
λ_h	thermal conductivity [W/(m K)]
λ_l	Lamé coefficient [N/m ²]
μ_l	Lamé coefficient [N/m ²]
π	circle number $\pi = 3.14\dots$
ρ	density [g/m ³]
ρ_0	equilibrium density [g/m ³]
σ	stress [N/m ²]
ω	angular frequency [Hz], [1/s]

Abstract

Conventional ultrasound inspection has been a standard non-destructive testing method for a long time. In most cases, though, a liquid coupling medium, such as water or gel, is required because of the huge impedance mismatch at a solid-air boundary. The physical contact with a liquid medium is a drawback because it prevents ultrasound inspection of many important materials. Modern industry, however, has a growing need for new, improved and remote non-destructive testing techniques for the inspection of new kinds of materials.

This thesis describes the use, advantages, limitations, and applications of a commercially available remote air-coupled ultrasound testing system that has been implemented in an accredited non-destructive testing laboratory (EN ISO/IEC 17025 : 2000). One of the objectives of the study, therefore, is to discover whether air-coupled ultrasound conforms to standards of modern quality assurance by comparing requirements of modern standards with the possibilities of this new advanced technique. The results are also compared with other non-destructive methods to discover if air-coupled ultrasound testing can compete with current techniques. First, the possibilities of linear air-coupled ultrasound inspection in through-transmission mode are investigated. In this case the equipment is used in its standard mode and ultrasound images (A-, B-, C-scan images) are performed. Second, the measuring technique is further developed to operate in the non-linear mode. This latter method uses the non-linear behaviour of defects for fast and selective imaging. Therefore, the excitation of a sample by injection of a sinusoidal wave using external or internal sources produces higher harmonics at the damaged area. By using these harmonics, defect-selective imaging is performed in which only the defect itself appears. In the case of non-linear air-coupled ultrasound, the sample is excited at frequencies that have the centre frequency of the air-coupled narrow band receiver as an overtone. When the receiver scans across the sample, it responds selectively to the higher harmonics.

In this study, high performance materials, components, and processes that are close to actual applications and that are difficult or impossible to measure with water are inspected. Results of air-coupled ultrasound imaging performed on fibre-reinforced plastics, water sensitive materials (e.g. C/C-SiC ceramic or wood), and smart structures are

presented in order to reveal delaminations, impacts, and growth of internal defects. Further measurements of monitoring the curing process of epoxy resin and of the manufacturing process of the new high temperature resistant C/C-SiC ceramic are presented. In addition, results are shown in which the actuator in shape-adaptive structures is used as transmitter and the receiver of the air-coupled system is used to record the signals. Thus it is possible to detect defect areas of the piezo actuators.

Analysing the results and by comparing them with other non-destructive testing methods demonstrates that air-coupled ultrasound inspection is a promising new technique that is suitable for modern quality assurance and one that can compete with other non-destructive testing methods.

Kurzfassung

Herkömmliche Ultraschalluntersuchung ist seit langer Zeit eine Standardmethode der zerstörungsfreien Prüfung. In den meisten Fällen wird aufgrund des großen Impedanzunterschiedes an einer Festkörper/Luft Grenzschicht ein flüssiges Koppelmedium (beispielsweise Wasser oder Koppelgel) benötigt. Dieser direkte Kontakt ist jedoch ein Nachteil, da er Ultraschallmessungen an vielen wichtigen Materialien unmöglich macht. Zur Untersuchung neuartiger Werkstoffe hat die heutige Industrie jedoch ein wachsendes Bedürfnis für neue, weiterentwickelte und berührungslose zerstörungsfreie Prüfverfahren.

Diese Arbeit beschreibt den Einsatz, die Vorteile, die Grenzen und die Anwendungen eines kommerziell erhältlichen luftgekoppelten Ultraschallsystems, welches in ein akkreditiertes Prüflabor (EN ISO/IEC 17025: 2000) eingebunden worden ist. Eine der Zielsetzungen dieser Arbeit ist deshalb herauszufinden, ob luftgekoppelter Ultraschall die Standards der modernen Qualitätssicherung erfüllt. Die geschieht durch den Vergleich der Forderungen heutiger Standards mit den Möglichkeiten dieser neuen fortschrittlichen Technik. Die Ergebnisse werden gleichfalls mit weiteren zerstörungsfreien Methoden verglichen, um zu beurteilen, ob luftgekoppelter Ultraschall mit gegenwärtigen Verfahren konkurrieren kann. Zuerst werden die Möglichkeiten des linearen luftgekoppelten Ultraschalls in Transmissionskonfiguration untersucht. Dabei wird die Messeinrichtung in ihrem Standardmodus verwendet und Ultraschallbilder (A-, B-, C-Bilder) aufgezeichnet. Dann wird die Messtechnik weiterentwickelt, um sie im nichtlinearen Modus zu betreiben. Diese letztere Methode verwendet das nichtlineare Verhalten von Fehlstellen für eine schnelle und selektive Darstellung von Defekten. Eine sinusförmige Anregung (externe oder interne Anregungsquelle) erzeugt höhere Harmonische in den geschädigten Bereichen. Die Verwendung dieser Harmonischen ermöglicht eine defekt-selektive Darstellung, in der nur die Fehlstellen selbst abgebildet werden. Im Fall des nichtlinearen luftgekoppelten Ultraschalls wird die Probe mit Frequenzen angeregt, die die Mittelfrequenz eines luftgekoppelten schmalbandigen Empfangsprüfkopfs als Oberton haben. Beim Abrastern der Probe reagiert der Prüfkopf selektiv auf die höheren Harmonischen.

In dieser Arbeit werden Hochleistungswerkstoffe, Bauteile und Prozesse untersucht, die nah an praktischen Anwendungen sind und die schwer oder überhaupt nicht mit Wasser untersucht werden können. Es werden Ergebnisse von luftgekoppelten Ultraschall präsentiert, die an faserverstärkten Kunststoffen, wasserempfindlichen Werkstoffen (beispielsweise C/C-SiC Keramik oder Holz) und an formadaptiven Strukturen durchgeführt wurden, um Delaminationen, Impactschäden und das Wachstum innerer Fehlstellen zu erfassen. Darüber hinaus werden Messungen dargestellt, bei denen der Aushärtvorgang von Epoxidharz und der Produktionsprozess der neuen hochtemperaturbeständigen C/C-SiC Keramik überwacht wird. Weiterhin werden Ergebnisse gezeigt, bei denen der Aktor einer adaptiven Struktur als Sender verwendet wird und die Signale mit dem Empfänger der Luftultraschallanlage aufgezeichnet werden. Auf diese Weise ist es möglich, fehlerhafte Bereiche eines Piezoaktors zu finden.

Durch die Betrachtung der Ergebnisse und deren Vergleich mit weiteren zerstörungsfreien Testmethoden wird gezeigt, dass luftgekoppelter Ultraschall eine vielversprechende neue Technik ist, die für moderne Qualitätssicherung geeignet ist und die mit anderen zerstörungsfreien Methoden konkurrieren kann.

1 Introduction

1.1 Quality assurance

According to the Codex Hammurabi of King Hammurabi of Babylon, 1700 B.C. [1,2], if a master builder built a house for someone, and the construction was not well done so that the house collapsed and killed the owner, the master builder would be killed too (§ 229). If, as a result, property is also destroyed, the master builder must replace the damaged property. Furthermore, because the master builder has not built the house well enough, he must rebuild it at his own cost (§ 223). This law is obviously very strict and clearly describes what has to be done and who is responsible. In 1985 the council of the European Community (EC) announced a “similar code” for product liability within the EC. Article 1 specifies that the manufacturer of a product is responsible for damage caused by a fault of the product [3]. The motivation of this guideline was to establish equal trading conditions within the EC, free movement of goods, and to unify customer rights in Europe. The principle of this guideline is that the guilt is independent of liability of the manufacturer. The consequence for Germany is the product liability law of 1989 (edited in 2002) [4]. This law has been one of the reasons why companies increased their efforts in the field of quality control and then developed quality assurance. In addition to the legal reasons mentioned above, a major aim of quality assurance is to establish cost-effective techniques and methods that ensure customers receive quality and faultless goods and thus enhance their satisfaction. This involves:

- examining the processes,
- ensuring that processes are fully understood,
- identifying a few critical checks along the way, and
- ensuring that a reject is not being produced.

As a consequence, quality assurance offers control at each step of the process so that it is very difficult to produce a defective item. If faults exist, they are identified and corrected before any further value is added [5]. Furthermore, quality control itself loses importance. All efforts to increase the quality of a good are combined in a quality management system (QMS) of a company [6]. It is important that a QMS has an effect on an entire company [7] (people, processes, tools, management) because 75 % of the

faults of a product are made during design, development, and process planning, while 80 % of the failures are corrected during quality control and during use (Figure 1).

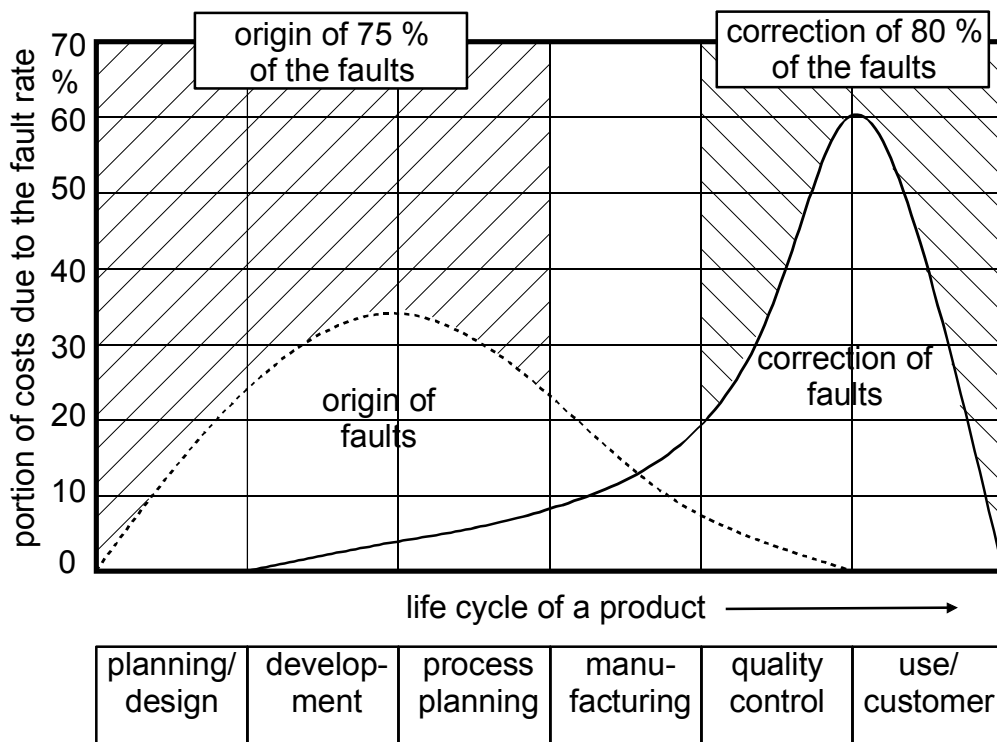


Figure 1: Origin and correction of faults [8].

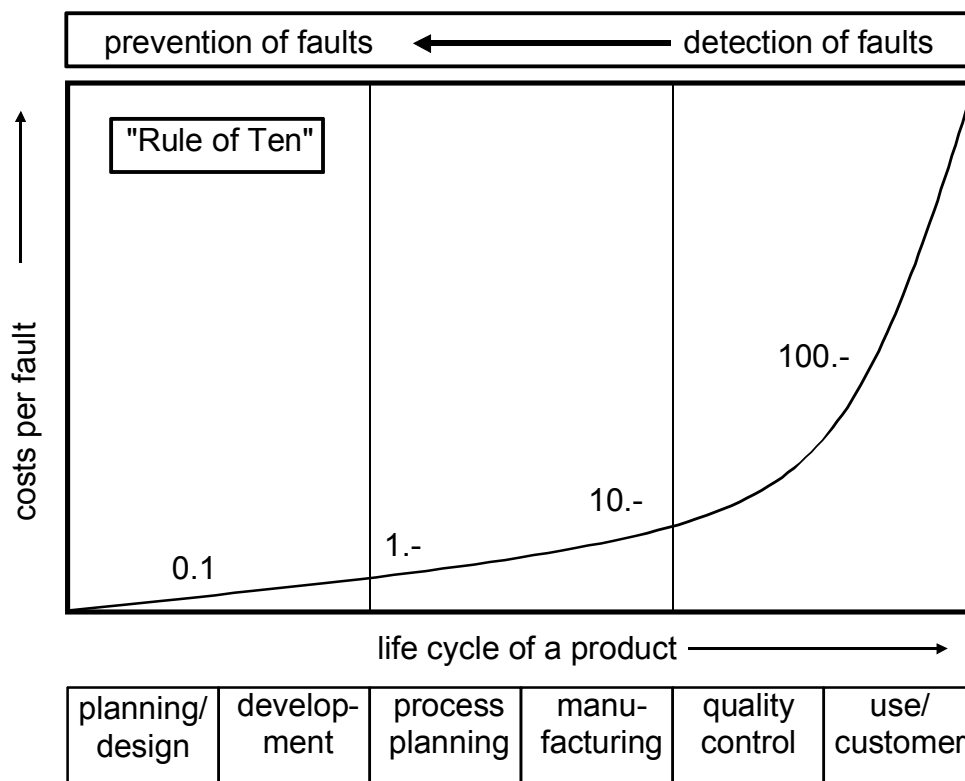


Figure 2: "Rule of Ten" [1].

From the viewpoint of cost efficiency, the “Rule of Ten” states that it is much cheaper to correct a fault in the early stages of a product’s life cycle (Figure 2). Destructive testing of items and materials is one tool for quality assurance. It consumes time and money, however, because the product must be taken out of production, treated, and inspected. Afterwards, the part cannot be taken back into the manufacturing process or used for further tests because it has been destroyed by such activities as tensile testing, cutting, or disassembling it into pieces. This destruction is an especially important disadvantage for inspecting high value goods and components, those that are difficult to manufacture, and those that are already in use.

1.2 Quality assurance and non-destructive testing

Non-destructive testing (NDT) techniques offer new possibilities because the good is not destroyed, and is usually inspected in a remote, fast, and reliable way. As mentioned above, though, modern thinking is not to examine as much as possible and sort out defective products in order to assure that only faultless products are sold. Instead, the major aim is to optimise the entire process so that quality is produced and not achieved by examination. Therefore, non-destructive testing techniques can be used readily in early stages such as development, process planning, and manufacturing. In the development stage, the decision can be made about how an item is inspected, what are the critical parts, and whether the components need to be adjusted to the requirements of a testing technique. In the pre-production process, samples with artificial defects that are close to possible ones can be used to qualify the inspection methods. Next, after first tests of use or operation, components need to be inspected to make sure that no defect occurred. During and after the production process, non-destructive testing techniques are applicable to monitor the process itself and the results achieved. After a product such as an automobile or airplane is delivered to customers, it is important to inspect safety-relevant components like high-performance brake disks or airplane structures after a certain period of time. NDT methods are increasingly more common in this field because in most cases the components even do not need to be removed.

A general example of how non-destructive testing can be used as a tool for quality assurance is described by a cross-linked feedback loop (Figure 3). The controlled vari-

ables of each loop are quality and a faultless product. The controlled system is affected by seven main disturbances:

- the production environment,
- the employees themselves,
- the materials used,
- the tools themselves,
- the method,
- the management, and
- the measuring techniques for the parameters.

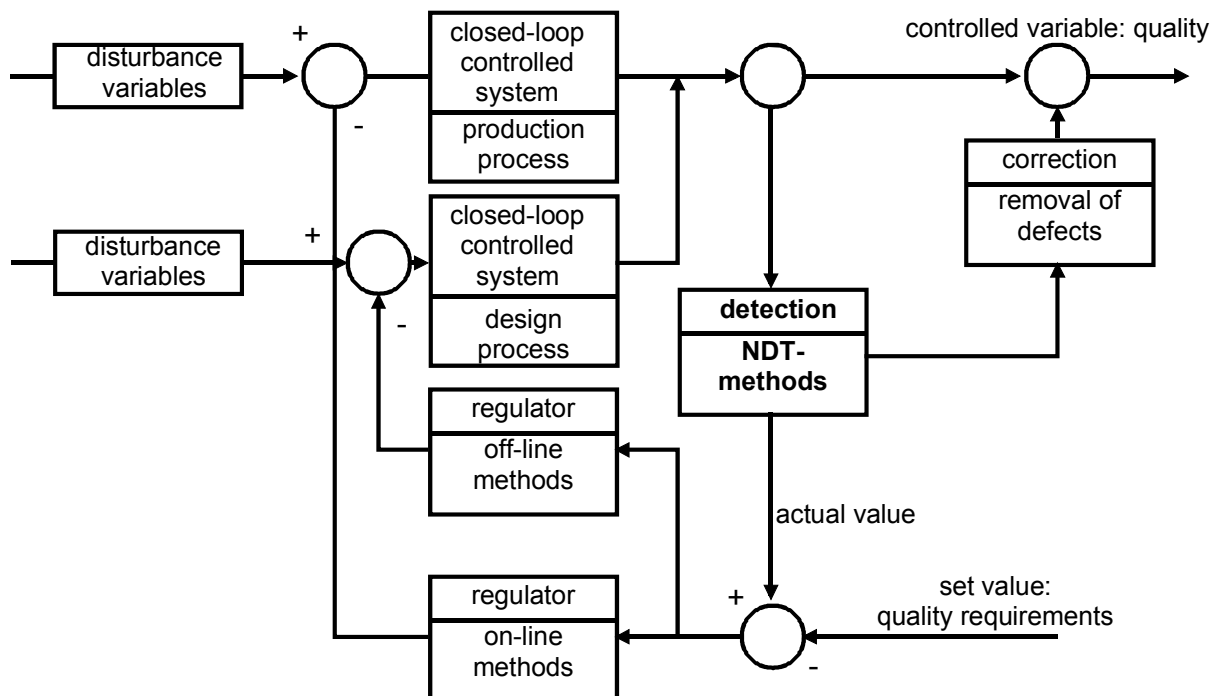


Figure 3: Cross-linked feedback loops of quality assurance and the position of NDT methods inside the loop.

For detection of faults, NDT methods can be used. These methods provide an actual value that is related to the quality. This value is compared by a regulator with the set value that is connected to the quality requirements. This regulator sets the values for on-line and off-line methods. On-line methods have a direct influence on the production process. Off-line methods such as Statistical Process Control (SPC) and Failure Mode and Effect Analyses (FMEA) [9] have an indirect control on the production line over the long run because of changes made during the design of a product. One of the topics of FMEA is the calculation of a risk failure priority number of a potential defect. This number includes an approximation of the importance and of the occurrence of the failure as

well as of the probability of the failure detection. Therefore, it is important to choose the appropriate technique and also to know the limitations of the method.

The introduction has discussed faults and non-destructive testing methods in general. The following section describes the most common non-destructive methods and their applications.

1.3 State of the art of non-destructive testing techniques

The general form of all non-destructive testing techniques is that a sample is excited and the response is detected (Figure 4). The excitation $E(t)$ of a sample can be performed with many kinds of waves with different frequencies, by many kinds of fields, and by particles. The most common forms are light sources, oscillation sources, sound waves, thermal waves, x-ray, electric, and magnetic fields. The response $R(t)$ of a sample, indicated by reflected, transmitted, deflected, penetrated, or emitted signals, is affected by changes in geometry such as variations of thickness, by the material itself, and by possible faults such as cracks, delaminations of layers, disbonding of adhesive joints, or corrosion. The signals received are either used directly for evaluation or compared with the excited signals or with the signal pattern of a faultless (defect-free) reference sample.

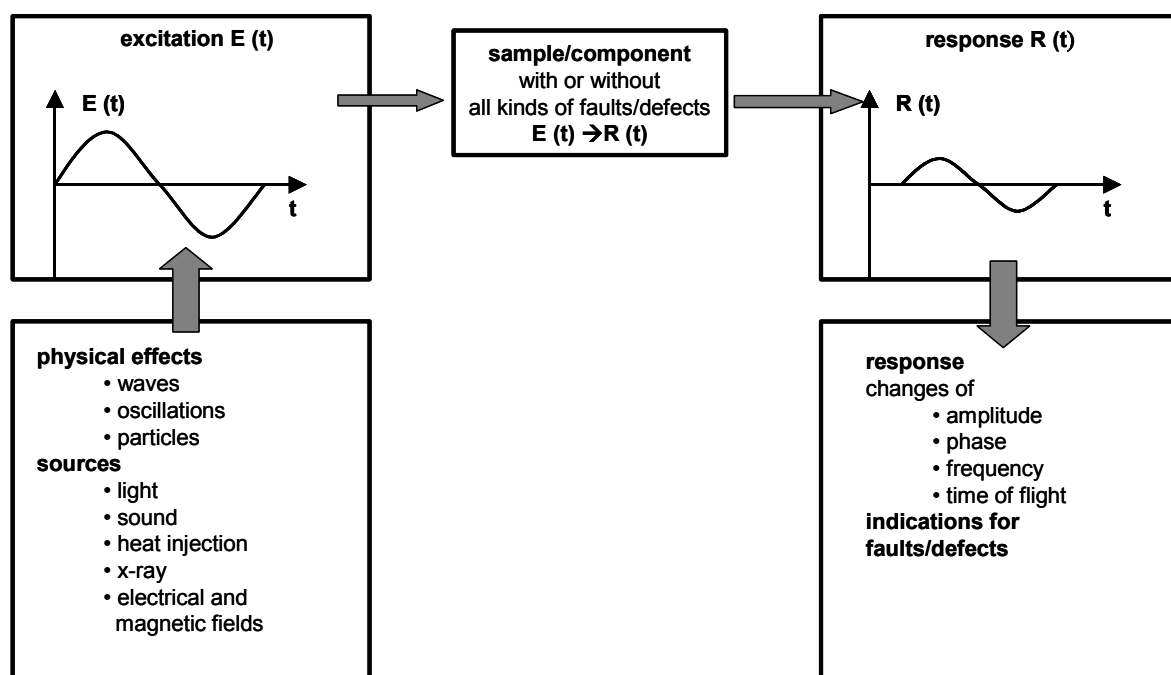


Figure 4: General form of non-destructive testing techniques [10].

1.3.1 Non-destructive testing using optical methods

Description: Perhaps the oldest non-destructive technique is inspection by the naked-eye (visual examination). The sample is excited by a light source such as the sun or lamps. The reflected light is detected by human eyes. This is still one of the most common methods used in industry. It has its limitations, though, because only visible defects but no hidden defects can be found, and human beings can concentrate on very monotonous work for only a short period of time before the work becomes routine. One of the 14 demands for quality management of W.E. Deming is to reduce routine work [11]. As a consequence, visual examination as an inspection method has limited applications.

Microscopy is another well known optical method. With a microscope, not only is optical magnification possible but also stresses inside of photoelastic materials are visible (polarizing microscopy). The photoelastic effect is based on the fact that the speed of light varies for different polarization directions. Macromolecule chains of polymers become oriented because of external or of internal strains that cause a preferred orientation. This process results in differences in the speed of light. With the help of two polarizers (one polarizer before the optical transparent sample, one polarizer behind the sample, and with a 90° - difference in polarization direction), light and black patterns can be detected that are dependent on the distribution of stresses.

The Moiré-effect and methods related to interference fringes are used to detect local changes of deformation caused by local heating, by external stresses, or by under-pressure. The Electronic-Speckle-Pattern-Interferometry (ESPI) is based on the technique in which a sample with a diffuse-reflecting surface is irradiated by an unfocused laser beam. With the help of optical components and a CCD-camera, the reflected laser light is recorded. By superimposing the reflected beam onto a reference laser beam, interference fringes are generated, which create an image with a grainy structure ("speckles"). For small deformations, the speckles are coupled to the deformation of the surface. The resulting image, evaluated by calculating the change of phase of images taken at different deformation steps, shows fringes of the same deformation patterns. As a result, deformations can be detected. By the use of different set-ups of the speckle-interferometer, it is possible to monitor deformations perpendicular to the surface (out-of-plane) or tangential to the surface (in-plane). Out of three images (x-, y-

and z- direction), the vector field of the three-dimensional displacement of the surface can be evaluated [12,13,14]. The disadvantage of this method is that the environment (e.g. vibrations, turbulences of the air, and unavoidable heating of the sample) may have a major negative influence on the results. Modern quality assurance demands reliable and easy-to-perform methods. Therefore, this technique is more suitable for research and for special purposes than for regular use during production process. Shearography is less sensitive to perturbations because it detects gradients of local deformations [15].

Applications of optical methods:

- visual examination/microscopy
 - opaque materials: defects on the surface (visible cracks, corrosion, local heterogeneities, roughness)
 - transparent materials: internal defects (e.g. cracks, holes) and inner stress fields caused by discontinuities
- Moiré-effect, Speckle-Pattern Interferometry, Shearography
 - surface deformations caused by visible or non-visible defects close to the surface (cracks, stresses, delaminations, impact damage, misorientations, local variations of stiffness)

1.3.2 Non-destructive testing using radiography and x-ray methods

Description: Five years before W. C. Roentgen (1895) discovered x-rays, the scientist A. W. Goodspeed from Philadelphia and the photographer B. Jennings made x-ray images of coins in through-transmission mode without knowing the significance [16,17]. Today the classic x-ray transmission technique is well known in such areas as medicine, security checks at airports, and NDT. X-ray inspection is a standard NDT technique for both metal and non-metallic components [18] and is an important as well as a reliable method used in industry for quality assurance as a process control tool. The images are made in through-transmission because x-rays transmit solids almost without deflection and the intensity of the beam is reduced proportionally to the 3rd power of the atomic number of the material. Because of the lower atomic number of polymers compared to metals, the absorption coefficient is low so that the contrast of x-ray images is also low. Boundaries of delaminations, cracks, and similar defects have almost no effect on the x-ray beam. As a result, in order to detect cracks that are open to the surface, a contrast medium with a high atomic number and that penetrates into the open crack is used. To increase the resolution of x-ray images, the beam can be fo-

cused to a diameter of a few micrometers (“micro-focus technique” [19]). Similar to refraction of light caused by prisms or by lenses, x-ray beams are also refracted at boundaries, such as pores or fibres, because of the wave behaviour (x-ray refraction technique). The refraction effects of x-rays, however, have a much lower extent than the refraction effects of light [20,21].

Applications of x-ray methods:

- classical radiography for inspection of
 - tubes and pipes
 - weldings

- micro-focus technique for inspection of
 - components for which high resolution is needed (e.g. inspection of microprocessors, plugs or all kinds of microelectronic items)

- x-ray refraction for detection of
 - inner surfaces
 - microcracks (density and orientation)
 - broken glass- and carbon fibres
 - fibre disbonding

1.3.3 Non-destructive testing using microwave methods

Description: The uses of microwaves for radar applications and microwave ovens are well known. Their use for non-destructive testing, however, is barely known. Because microwaves are electromagnetic waves, the physical laws for refraction, reflection, and scattering can also be applied to them. As compared to light, microwaves have a much larger wave length (up to a factor 10^5). Many polymer materials are almost transparent at such long wave length and as a result inspection is easily performed in this spectral region. The penetration depth depends on the dielectric loss factor and on the frequencies used [22]. Differences in material properties (like heterogeneities) and in density cause a change of signal that can be detected. Also changes in the polarisation of microwaves are used to detect local variations of anisotropy. Because of the skin-effect, the penetration depth of microwaves inside metals is low. As a result, only defects close to surfaces can be detected. The primary advantages of microwave testing techniques are that measurements can be performed contact-free and with single-sided access (e.g. with open-ended rectangular wave guides [23,24]). Additionally, the injection moulding process for manufacturing plastic parts, for example, can be monitored

by microwave sensors to record the filling of the forms and the cooling down of the melt [25]. These two points have a significant influence on the quality and the shape of plastic parts. Thus, with the inspection of microwaves, two of the principles of modern quality assurance can be fulfilled: first processes must be fully understood and second processes must have the ability to produce faultless parts [26].

Applications of microwave methods:

- monitoring
 - the curing process of resin
 - the moisture content of a variety of materials
 - changes in defects in glass fibre reinforced polymers
- detection of
 - delaminations
 - corrosion
- measuring glass fibre orientation of reinforced polymers

1.3.4 Non-destructive testing using thermal methods

Description: Thermography uses the property that every object with a temperature of above 0° Kelvin emits a continuous frequency spectrum of electromagnetic waves (based on Planck's radiation law). An infrared camera, such as a thermal focal plane array camera, detects a certain frequency range. The radiation intensity measured depends on the temperature of the sample and on the emission coefficient of the surface. If this coefficient is approximately constant over the entire surface, the image of a thermal camera primarily displays the temperature distribution. A thermal image is a sensitive indicator of heat flow, changes of temperature, and hidden structures. Because the inspection takes place in a remote and a non-contact way, thermography is an important method for non-destructive evaluation. Also, for process control, production monitoring, and for quality assurance, thermography is a primary technique for applications in which heat (e.g. alloy mould) is involved. Because this method relies on detection of anomalies in the temperature pattern, there might be artefacts caused by air turbulence or reflections from the environment. These artefacts may hide critical anomalies caused by defects.

An infrared camera can also be used to detect a thermal wave [27]. This wave, described as space-time dependence of temperature modulation, behaves like other waves and is both transmitted and reflected at thermal boundaries. An intensity-modulated radiation (temperature modulation) is induced from the outside onto the sur-

face and propagates into a sample by absorption. The thermal wave reflected at inner boundaries interferes with the temperature modulation on the surface. By performing Fourier analyses, magnitude and phase images are calculated from a sequence of images taken during modulated irradiation. The magnitude image is less sensitive than the phase image because it is affected by infrared emission, by heterogeneities of the surface, and by heterogeneities of optical radiation. This disadvantage is avoided by using phase-angle images. Also in comparison to the magnitude image, the depth range is almost doubled [28,29,30,31]. Lockin thermography [32,33,34, 35,36] makes use of this technique of evaluating magnitude and phase images. Thermal waves can be generated either by external excitation like sinusoidally modulated lamps (optical lockin thermography, OLT) or by internal excitation caused by such sources as an attached modulated ultrasound source (ultrasound lockin thermography; ULT [37]). The acoustic wave is transmitted into the sample from which it is reflected at boundaries (e.g. surfaces) until the wave hits a defect that is able to generate heat by hysteretic effects, by friction of crack tips, or by friction of delaminations. Instead of sinusoidal modulated sources, a short sonic burst (ultrasound burst phase thermography, UBP [38]) can be used. The frequency spectrum of the detected heat changes and the cooling-down period provide information about the depth where defects are located. The advantage of UBP is the reduced measurement duration time. ULT and UBP are defect-selective methods because only signals from a defect are detected.

For quality assurance, fast and defect-selective techniques are essential to reduce cost, to help understand processes, and to reduce inspection time. Thermography cameras, especially for lockin-methods of NDT applications, are still quite expensive. As a result, these techniques are used primarily for high value components or safety-relevant components.

Applications of thermal methods:

- classic thermography for monitoring of
 - mould profiling (e.g. alloys)
 - plastic extrusion
 - paper web processes
 - paper plate manufacturing

- optical lockin thermography (OLT) for
 - detection of
 - disbonded stringers

- cracks, delaminations
- hidden corrosion
- disbonding of layers and adhesive joints
- loosen rivets and screws
- hidden heterogeneities inside materials
- monitoring of the integrity of structures
- inspecting of paint thickness

- ultrasound lockin thermography (ULT) and ultrasound burst phase thermography (UBP)
 - defect-selective imaging of delaminations, impacts cracks, broken stringers, and disbonding

1.3.5 *Non-destructive testing using vibration methods*

Description: In addition to visual examination, vibration methods have been well known for a long time. Classic methods consider only linear behaviour that is described by Hooke's law. Some common examples are:

- Thumping melons and listening to the response to discover if they are ripe or not.
- Tapping ceramic cups and plates to find out if there are cracks.
- Knocking with coins on wall tiles to identify loose tiles.

In industry, classic vibrometry is used to inspect running machines components like gear boxes to detect imbalances or turbulences. Another example is knocking on wheels of railway vehicles to detect cracks. These techniques employ natural frequencies, bending modes, resonant frequencies, and the width of peaks in the frequency spectrum as well as acoustical impedance. All of these effects are linked with mechanical properties, such as velocity, density, stiffness, or damping, that are important for the quality of an item. Local changes in mechanical properties that might be related to potential defects cause changes in the values measured, such as shifts of resonance frequencies or broadening of peaks (damping). Results are achieved by comparing the values measured with those of a faultless sample. The disadvantage of these techniques are that spectral changes can be caused by sources other than defects (such as changes in geometry caused by the manufacturing process) and that it is difficult to distinguish among the sources. Also, because of standing wave fields and nodes, there is no constant sensitivity over the entire sample and defects may not be found. If the only objective is to identify faultless components, though, vibrometry offers many possibilities.

If the inspection is performed only by tapping, such as on melons, ceramics, or tiles, and “recording” the response with the human ear, the test is subjective and depends on the experience of the person doing the testing. Therefore, from the viewpoint of quality assurance, such a procedure can only provide a hint and is not suitable to qualify a potential defect because of the subjective impressions of people. To avoid this disadvantage, reliable excitation sources, recording equipment, and data processing are needed. Excitation can be performed either by external sources, such as hammers, shakers, piezo-electric actuators, or by internal sources, such as embedded actuators or running a machine or component that needs to be inspected. To record signals, microphones and analogue or digital equipment for data processing can be used. The disadvantage of using microphones is that sound sources of the environment may affect the signals received. To overcome this disadvantage, a laser vibrometer can be used and the frequency spectrum as well as natural frequencies can be evaluated.

In comparison to classic (linear) methods, new and interesting techniques like non-linear vibrometry use non-linearity for selective detection of defects independent of geometry. One example of non-linear effects is clapping in old automobiles. Clapping can be caused by loose and moving boundaries due to such causes as loose screws. The moving interaction of boundaries is a source for higher harmonics (overtone caused by non-linear behaviour). It is interesting to note that if screws would be fastened, then there would be no higher harmonics. For non-linear inspection of samples, resonant excitation must be avoided so that a constant sensitivity over the entire sample is achieved by missing standing wave patterns. A scanning laser-vibrometer that monitors the frequency spectrum at each pixel on the surface of a sample can be used to image local non-linearity. By using the level of a certain overtone for imaging, areas of non-linear behaviour (potential defects) are selectively displayed [39]. Thus, non-linear vibrometry is an interesting tool for quality assurance when quick and reliable decisions must be made.

Applications of vibrometry methods:

- linear vibrometry for
 - detection of
 - defects in valves
 - loose joints
 - heterogeneities
 - cracks

- recording of bending modes
- non-linear vibrometry (defect-selective imaging method) for
 - detection of
 - delaminations of laminates
 - impact damage of laminates
 - disbonded stringers
 - cracks
 - hidden corrosion
 - disbonding of adhesive joints
 - hidden heterogeneities inside materials
 - inspection of shape adaptive structures

1.3.6 Non-destructive testing using ultrasound methods

Description: In 1929, when the use of ultrasound for non-destructive testing was first published by S. Sokoloff, it was not known if ultrasound inspection would be successful nor if it would be able to compete with radiography [40]. Today, ultrasound inspection methods are powerful tools for non-destructive testing and are widely used in industry because high resolutions are possible depending on the chosen frequency (100 kHz – 20 MHz) and because measurements are relatively easy to perform with commercially available equipment [41,42]. The basic process, described in more detail in chapter 4, involves ultrasound waves being launched by a transducer into a sample and either the reflected wave is recorded by the same transducer (reflection technique) or the wave that is transmitted through the sample is recorded by a second transducer on the opposite side (through-transmission technique). Because of additional acoustic boundaries of potential defects (difference in acoustic impedance; section 2.4), the wave is partly reflected and partly transmitted. The reflection technique has the advantage that only single-sided access is needed, and if the sound velocity of the material is known, the depth of a defect can be calculated. The through-transmission technique is used for highly sound-absorbent materials because the sound must pass through the sample only once. Because of the huge impedance mismatch between solid and air, a liquid coupling medium, especially for high frequencies, is needed. For one-point measurements, a gel coupling medium is sufficient. For scanning techniques, however, the entire sample must be immersed in liquid, as in a water tank, for constant coupling conditions. This restriction is the major disadvantage because it is not a remote technique. In industry, there is a growing need for dry-contact or non-contact inspection. Therefore, major ongoing attempts in the non-destructive testing community seek to fulfil this

need. Recently, improvements in electronics and in transducer design allow air-coupled measurements to be performed with sufficient signal-to-noise ratio (chapter 5).

Applications of ultrasound methods:

- ultrasound inspection for
 - detection of
 - cracks
 - heterogeneities
 - delaminations of laminates
 - impact damage of laminates
 - corrosion
 - inspection of
 - weldings
 - fibre matrix interaction

1.4 Scope of the thesis

Non-destructive testing is one of the most important means to detect, verify, and to qualify the quality of items. When applied during all stages of a product's life-cycle from design to operation, it has always been an integral and central part of quality assurance. NDT techniques must provide reliable and accurate testing as well as confidence to the test results. These methods must meet the requirements of customers and regulatory bodies for the safety of all kinds of applications. Each of the NDT techniques described in section 1.3 plays its role in this field. Each technique is suitable for specific purposes and there is no general method that covers all. The most important requirement for all techniques is that test objects are not affected by these methods and that the techniques have no influence on the results (Figure 3). Conventional ultrasound has limitations because a liquid coupling medium is needed and because the test object must be kept in a water tank if scanning measurements are needed. Water may penetrate the sample and therefore influence the test object. For further heat treatment of an item or for monitoring of processes like the curing process of epoxy resin, this use of liquid is a major disadvantage. Also immersion in water may affect the ultrasound propagation inside water sensitive materials, and thus influences the signal received, especially if the time dependence of water diffusion is considered.

Air-coupled ultrasound (ACU) overcomes these limitations and offers new possibilities because it is a non-contact method. Air-coupled techniques were proposed about three

decades ago but not brought into practice because of inadequate equipment [43,44]. Recently, improvements in electronics and in transducer design permit air-coupled measurements to be made with sufficient signal-to-noise ratio [45,46,47]. Commercially available equipments from various manufacturers are currently used mostly at universities for scientific purposes but some industry applications exist already.

The scope of this study is to establish and to integrate ACU measuring techniques into the NDT lab of the Institute for Polymer Testing and Polymer Science (IKP) and to investigate both the potential and the limitations of this new technique for industrial applications. Furthermore, this study will verify whether ACU inspection meets the standards for modern quality assurance and is able to be used as a new tool. Therefore, a variety of different materials and components will be inspected and the results compared with those of other NDT techniques.

- Wood samples were chosen because conventional ultrasound techniques using water are not appropriate so that many ongoing investigations attempt to find suitable NDT techniques.
- Carbon fibre reinforced polymers (CFRP) are being used more frequently in the automotive and aerospace industries for safety-relevant components. Because of layer structures, new potential defects like impact damage and delamination of layers are possible and need to be inspected.
- Gluing of components is replacing other joining techniques for certain applications. Thus, it is important to monitor the curing process of epoxy resin to find out if it is possible to distinguish among different mixing ratios and to detect debonded interfaces. For this kind of inspections, remote techniques are appropriate.
- Components made out of Honeycomb structures are used for such things as airplanes or helicopters. The focus in this work has been to detect disbond between skin and cells as well as to detect inclusions like resin agglomerations or water.
- Reinforced ceramics have a high temperature resistance and thus are a material that is ideal for brake discs of sports cars and for heat protection shields of space ships. The manufacture of reinforced ceramics components requires new and im-

proved processes. Processes that are safe and fully understood are one of the primary objectives of quality assurance so that this new manufacturing method is being monitored with ACU. Because there are several heat treatment steps, inspections of the process in a water bath would not be possible. Not only the manufacturing but also most likely potential defects need to be examined.

- Shape adaptive structures are used in industrial applications because of their adjustable mechanical properties. To make these properties possible, piezoelectric actuators are embedded in glass fibre reinforced polymer (GFRP) or in CFRP-components. One of the main inspection approaches of these structures is to use the embedded actuator itself as the excitation source for NDT methods (health monitoring). A non-contact technique like ACU is able to receive the transmitted signals.

The samples used for this study were provided mostly by industrial sources and by other institutions that have a strong interest in new methods and are seeking reliable testing. As a result, it is feasible to work on real NDT problems.

For the primary quality assurance issues, easy-to-handle techniques are needed that are uncomplicated, produce reliable results, and allow fast decisions. As discussed above, defect-selective NDT methods like ULT or non-linear vibrometry offer these outcomes. Ultrasound measurements performed with contact technique on small samples with nearly ideal defects to detect non-linearity and imaging with ultrasound microscopy [48] have been described in literature. Thus, the idea rose as to whether non-contact, non-linear ACU inspection can be applied for defect selective imaging on materials of practical importance and used in industrial applications today. Because conventional ultrasound methods are widely used and well known in industry, it is unproblematic to establish this new air-coupled technique. Such techniques have not been established to date to any appreciable extent because of the lack of knowledge about possible applications.

2 Linear Acoustics

The field of acoustics covers generation, propagation, and receiving of sound [49]. Sound waves with frequencies higher than human beings can hear are called ultrasound waves. Depending on their age, human beings can hear frequencies up to 20 kHz. Table 1 presents a classification of different ranges of sound waves.

frequency range	classification of waves
$0 < f < 20 \text{ Hz}$	infrasound waves
$16 \text{ Hz} < f < 20 \text{ kHz}$	audible waves
$20 \text{ kHz} < 1 \text{ GHz}$	ultrasound waves
$f > 500 \text{ MHz}$	hypersound waves

Table 1: Classification of acoustic waves according to frequency range [50].

The classification scheme makes sense, however, if different uses and origins of the sound waves are considered. Infrasound waves, for example, are generated by earthquakes. Audible waves are used by human beings for vocal communication and are also generated by such things as musical instruments like pianos, drums, or organs. Ultrasound has its applications in the field of material testing and in medicine. Also, in nature, bats and dolphins use ultrasound waves for orientation.

There are several known types of wave forms. The two most common are longitudinal and transversal waves. For longitudinal waves, the displacement of particles occurs in the same direction as the wave propagation (Figure 5).

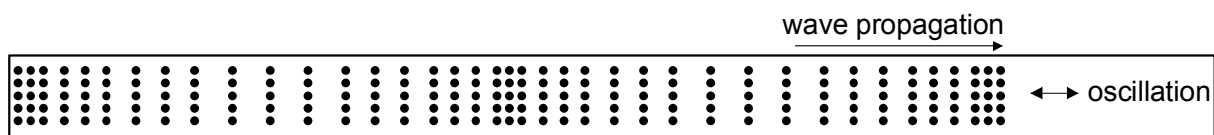


Figure 5: Propagation of a longitudinal wave.

This type of wave is related to a local change of pressure and density. These changes cause resetting forces that are needed so that the particles vibrate back to their equilibrium position. For transversal waves, particles oscillate transversally to the direction of wave propagation (Figure 6) and therefore do not cause a local change of density or pressure. As a result, transversal waves cannot propagate in liquids or gases because

resetting forces are not present. In solids, however, resetting forces are present because of solid bindings.

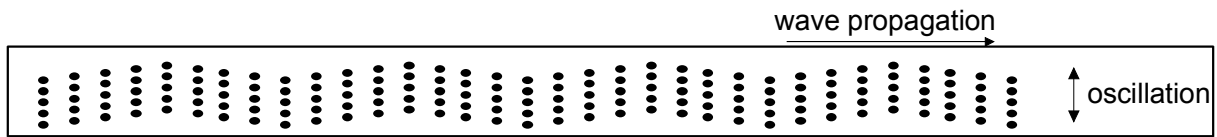


Figure 6: Propagation of a transversal wave.

ACU inspection in this study is performed in through-transmission mode, at normal incidence, and at a frequency of 450 kHz. Therefore, the focus in this chapter is on incident waves, on longitudinal wave propagation in liquids and in air, and on reflection as well as on transmission of waves at acoustical boundaries.

The starting place to describe sound wave propagation by particle vibration is the binding media through which the waves propagate. The curve of the energetic potential of an atom (ion) plotted against the distance (radius r) of a neighbouring atom (ion) is shown in Figure 7.

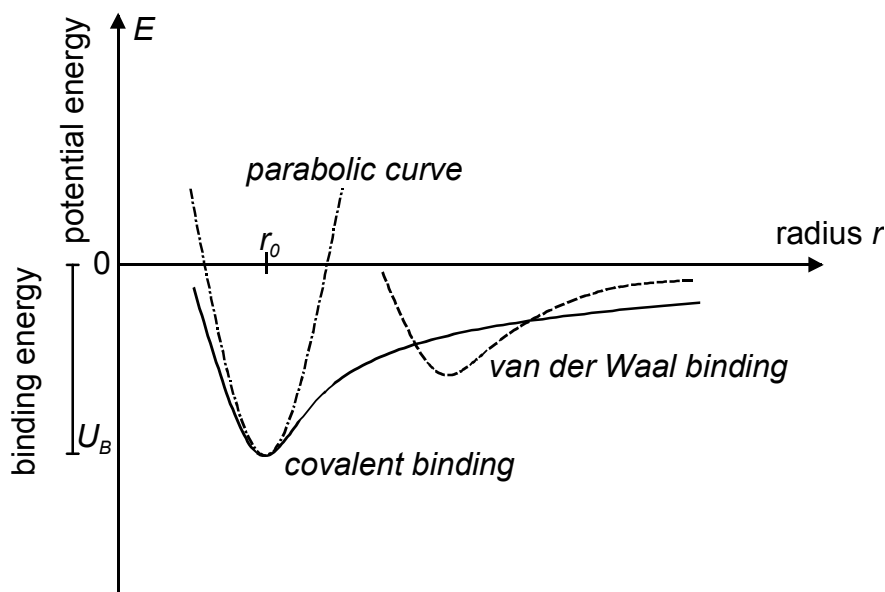


Figure 7: Principal potential energy curve of particles.

The potential energy curve $E = \int (F_r + F_a) dr$ is the integral of the sum of two types of forces that interact with each other [51,52]. The first type is repulsive forces ($F_r \sim r^{-12}$) that are caused when electron shells are deformed due to compression. The second type is attractive forces ($F_r \sim r^{-6}$) caused by either covalent bonding forces, by Coulomb forces of ions, or by dipole interaction (van der Waals forces). The minimum of

the potential energy curve is the binding energy U_B between two particles ranging between

- 0.01 eV/atom - 0.2 eV/atom for van der Waals bonding,
- 1 eV/atom - 7 eV/atom for covalent bonds,
- 1 eV/atom - 8 eV/atom metallic bonds, and
- 3 eV/atom - 15 eV/atom for ionic (electrostatic) bonds.

As values become higher, the curve of the potential energy becomes narrower. As a result, it is easier to deform materials along the direction of dipole forces than along the direction of ionic binding. The deformation modulus (e.g. Young's modulus or bulk modulus of elasticity) is a factor of the force with which a medium responds to deformation, is proportional to the second derivative of the potential energy curve, and therefore proportional to its curvature. In general, repulsive forces have a shorter effect over distance than attractive forces so that the resulting potential energy curve is not symmetrical. The value of r_0 is the equilibrium distance (radius). For small oscillations (elastic deformation and linear behaviour) about the potential minimum r_0 , the run of the curve can be approximated by a parabolic curve. For higher displacements u the oscillation becomes non-symmetrical because of the run of the potential curve. This leads to a non-linear behaviour of the media. Because of existing coupling among particles, particles next to the displacement u also oscillate but with a time delay. Thus, a wave is able to propagate. Wave propagation in general is accompanied with changes of density ρ , pressure p , particle displacement u , and particle velocity v .

2.1 Fundamentals of elastic theory

The propagation of waves in different kinds of media (only continua are considered) is accompanied by a periodic displacement of particles u of this media out of their equilibrium and by elastic forces. To describe wave propagation by elastic theory, the particle is regarded as an infinitesimally small volume element (including a number of atoms) which is considered to be homogeneous. In the regular stage, the particles are in their equilibrium which is caused by inner molecular forces. The position is described by the vector \bar{r} . The displacement of a particle (or volume element) out of its equilibrium is expressed by the vector \bar{u} . The descriptions are based on infinitesimally small deformations and linear behaviour. These estimates are possible because the deformation

caused by ultrasound wave propagation is considered to be infinitesimally small in the first approximation.

The three-dimensional deformation of an infinitesimally small volume element is described by the strain tensor

$$\varepsilon_{ik}(x_1, x_2, x_3) = \frac{1}{2} \left(\frac{\partial u_i}{\partial x_k} + \frac{\partial u_k}{\partial x_i} \right) \quad (i, k = 1, 2, 3). \quad (2-1)$$

The tensor ε_{ik} is symmetrical and therefore a transposition to the principal strain axis is feasible. Then all shear components are 0 and one obtains

$$\varepsilon_{ii} = \varepsilon_{ik} \delta_{ik} \quad (i, k = 1, 2, 3), \quad (2-2)$$

in which δ_{ik} represents the Kronecker Symbol ($\delta_{ik} = 1$ for $i = k$ and $\delta_{ik} = 0$ for $i \neq k$).

If a volume element which has edges parallel to the principal axis is deformed, the angles between the edges do not change while the length of each edge changes to $1 + \varepsilon_{11}$, $1 + \varepsilon_{22}$, and $1 + \varepsilon_{33}$. Therefore, the volume change becomes

$$\Theta = \frac{dV - dV_0}{dV_0} = \frac{dV}{dV_0} - 1 = \frac{(1 + \varepsilon_{11})(1 + \varepsilon_{22})(1 + \varepsilon_{33}) dx_1 dx_2 dx_3}{dx_1 dx_2 dx_3} - 1. \quad (2-3)$$

If the non-linear terms are neglected (for infinitesimally small deformation) the change of volume can be expressed as

$$\Theta \approx 1 + \varepsilon_{11} + \varepsilon_{22} + \varepsilon_{33} - 1 \quad (2-4)$$

$$\Theta = \varepsilon_{11} + \varepsilon_{22} + \varepsilon_{33} \quad (2-5)$$

$$\Theta = \frac{\partial u_1}{\partial x_1} + \frac{\partial u_2}{\partial x_2} + \frac{\partial u_3}{\partial x_3} = \text{div } \vec{u}. \quad (2-6)$$

As a result, the equation of continuity can be written as

$$\frac{d\Theta}{dt} = \text{div } \vec{v}. \quad (2-7)$$

The vector

$$\vec{v} = \frac{d\vec{u}}{dt} \quad (2-8)$$

describes the velocity (time derivative of the displacement u) of the infinitesimally small volume element. Velocity v and displacement u are both dependent on position and time.

Inside a non-deformed body, all mechanical forces are in equilibrium with each other. Thus, the sum of all forces of one volume element is 0 and does not have an effect on the surrounding volume elements. As a result of deformation and because of intermolecular forces, elastic tensions arise. The symmetrical second-order stress tensor (Figure 8)

$$\sigma_{ik}(x_1, x_2, x_3) = \begin{bmatrix} \sigma_{11} & \sigma_{12} & \sigma_{13} \\ \sigma_{21} & \sigma_{22} & \sigma_{23} \\ \sigma_{31} & \sigma_{32} & \sigma_{33} \end{bmatrix} \quad (2-9)$$

characterizes the entire stress state of a body element at x_1, x_2, x_3 . By a coordinate transformation the shear stresses vanish, so that in the new coordinates one obtains only diagonal elements

$$\sigma_{ii} = \sigma_{ik} \delta_{ik} \quad (i, k = 1, 2, 3). \quad (2-10)$$

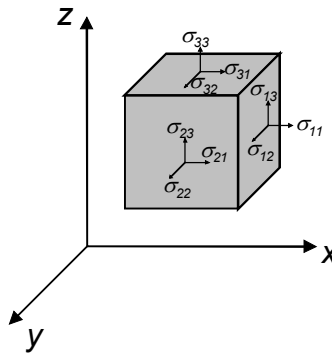


Figure 8: Stresses and their directions affecting a volume element.

If the sum of the force vectors at a volume element is not equal to zero, then the forces are not compensated and the volume element (particle) is accelerated reciprocally to its mass. This leads to the equation of motion in acoustics

$$\frac{\partial \sigma_{ik}}{\partial x_k} = \rho \frac{dv_i}{dt}, \quad i, k = 1, 2, 3 \quad (2-11)$$

which describes the general changes of tension along the axis with the acceleration dv_i/dt . The acceleration in equation (2-11) can be expressed by

$$\frac{dv_i}{dt} = \frac{\partial v_i}{\partial t} + \frac{\partial v_i}{\partial x_k} v_k, \quad i, k = 1, 2, 3. \quad (2-12)$$

The first term illustrates the change of particle velocity depending on time in a given volume because of forces. The second term represents the change of particle velocity as a result of the displacement of particles in the neighbourhood. For infinitesimally

small displacements and for small velocities, the second term can be ignored. The current density (functions of position and time)

$$\rho = \rho_0 + \Delta\rho \quad (2-13)$$

of the accelerated medium is the sum of the equilibrium density ρ_0 and the change of density caused by deformation $\Delta\rho(x_1, x_2, x_3, t)$. For infinitesimally small deformations, ρ can be estimated by ρ_0 . Taking all of these simplifications into account, the equation of motion (2-11) becomes

$$\frac{\partial \sigma_{ik}}{\partial x_k} = \rho_0 \frac{\partial v_i}{\partial t}, \quad i, k = 1, 2, 3. \quad (2-14)$$

This formula is strictly correct only for infinitesimally small deformations (amplitudes). For finite amplitudes, the non-linear terms must be considered (section 3.1.1).

Both deformation and tension have a linear dependence on each other for small values (Hooke's law)

$$\sigma_n = C_{nm} \varepsilon_m \quad n, m = 1, 2, 3, 4, 5, 6 \quad (2-15)$$

in which C_{nm} is originally a fourth-rank tensor transformed into 2-indices notation. Due to the symmetry of the ε and σ tensors, this tensor is symmetrical as well. For isotropic media, the coefficients depend only on the two Lamé coefficients λ_L and μ_L :

$$\begin{aligned} C_{12} = C_{13} = C_{23} = \lambda_L, \quad C_{44} = C_{55} = C_{66} = \frac{1}{2}(C_{11} - C_{12}) = \mu_L, \\ C_{11} = C_{22} = C_{33} = \lambda_L + 2\mu_L. \end{aligned} \quad (2-16)$$

Therefore, Hooke's law for isotropic media is

$$\sigma_{ik} = \lambda_L(\varepsilon_{11} + \varepsilon_{22} + \varepsilon_{33})\delta_{ik} + 2\mu_L\varepsilon_{ik}, \quad i, k = 1, 2, 3. \quad (2-17)$$

2.2 Wave propagation in liquids and gases

In this section the wave propagation in liquids and gases is explained which is important to understand because ultrasound inspection is often performed with liquid or air as coupling media. Both media show elasticity of volume but not of shape so that no shear waves exist and tensions (pressures) are always normal on the surface. Compression of these media is feasible, however, so that longitudinal (compression) waves can propagate through liquids and air. Therefore, the motion of particles is in a certain direction and is free of rotation, expressed by

$$\text{rot } \mathbf{v} = 0. \quad (2-18)$$

2.2.1 Hydrodynamic equations

The equations of motion (2-11) and (2-14) are solved for liquids and gases by using the stress tensor (equation (2-9) for all-round pressure: $\sigma_{ik} = -p\delta_{ik}$) and can be rewritten as

$$-\frac{\partial p}{\partial x_k} \delta_{ik} = \rho_o \frac{\partial v_i}{\partial t} \text{ or } \nabla p = \rho_o \frac{\partial \vec{v}}{\partial t}. \quad (2-19)$$

The minus sign is needed to represent positive pressure conditions.

The equation (2-18), which shows that no rotation is possible in the absence of shears, indicates

$$\frac{\partial v_1}{\partial x_2} - \frac{\partial v_2}{\partial x_1} = \frac{\partial v_2}{\partial x_3} - \frac{\partial v_3}{\partial x_2} = \frac{\partial v_3}{\partial x_1} - \frac{\partial v_1}{\partial x_3} = 0 \quad (2-20)$$

and allows the definition of a scalar function $\varphi(x_1, x_2, x_3, t)$ ("potential of velocity"; according to the potential energy term) which equals

$$\vec{v} = -\nabla \varphi. \quad (2-21)$$

As a result, the components of the vector of the particle velocity can be expressed as

$$v_{x_i} = -\frac{\partial \varphi}{\partial x_i}. \quad (2-22)$$

By substituting the particle velocity \mathbf{v} by its potential φ , the equation of motion (2-8) becomes

$$\nabla p = \rho_o \frac{\partial}{\partial t} (\nabla \varphi) = \nabla (\rho_o) \frac{\partial \varphi}{\partial t} \Rightarrow p = \rho_o \frac{\partial \varphi}{\partial t}. \quad (2-23)$$

The continuity equation (2-7) for liquids and gases (air) becomes

$$-\frac{1}{\rho_o} \frac{\partial \rho}{\partial t} = \text{div } \vec{v} = -\text{div} (\nabla \varphi) = -\Delta \varphi \quad (2-24)$$

2.2.2 Equation of state for liquids and gases

The equation of state for liquids and gases can be developed from the following considerations: Hooke's law for the compression of ideal liquids and gases is

$$p = P - P_0 = K \cdot s. \quad (2-25)$$

The letter P denotes the actual pressure at a certain point because of compression, P_0 the equilibrium pressure, K is the bulk modulus of elasticity, and s the ratio of $\frac{\Delta\rho}{\rho_0}$. The linear dependence of pressure and density is valid only for infinitesimally small changes. In general, the dependence is not linear and is given by:

$$P = P(\rho). \tag{2-26}$$

The actual density ρ is the sum out of the equilibrium density ρ_0 and the change of density $\Delta\rho$. In most practical cases, the change of density is very small in comparison to the equilibrium density ($\Delta\rho \ll \rho_0$) so that the equation (2-26) can be approximated by Taylor's series

$$P = P_0 + \frac{1}{1!} \left(\frac{dp}{d\rho} \right)_{\rho=\rho_0} \Delta\rho + \frac{1}{2!} \left(\frac{d^2 p}{d\rho^2} \right)_{\rho=\rho_0} \Delta\rho^2 + \dots \tag{2-27}$$

or with $s = \frac{\Delta\rho}{\rho_0}$

$$P - P_0 = \frac{1}{1!} \left(\frac{dp}{d\rho} \right)_{\rho=\rho_0} \rho_0 \cdot s + \frac{1}{2!} \left(\frac{d^2 p}{d\rho^2} \right)_{\rho=\rho_0} (\rho_0 \cdot s)^2 + \dots \tag{2-28}$$

The first (linear) term in (2-28) includes the linear bulk modulus

$$K = \left(\frac{dp}{d\rho} \right)_{\rho=\rho_0} \rho_0 \tag{2-29}$$

and the second term includes the non-linear bulk modulus B .

Again for small compressions, the terms of higher order can be neglected and the equation of state is written as

$$P \approx P_0 + \left(\frac{dp}{d\rho} \right)_{\rho=\rho_0} \Delta\rho \tag{2-30}$$

and

$$p = P - P_0 \approx \rho_0 \left(\frac{dp}{d\rho} \right)_{\rho=\rho_0} \cdot s = K \cdot s \tag{2-31}$$

This linear equation is also another form of Hooke's law.

Wave propagation is considered to be an adiabatic process because changes take place quickly so that no heat flows out of or into the system. In describing an adiabatic

process, the first law of thermodynamics, which expresses the internal energy change (dU) as the sum of the change of heat (dQ) and the change of work ($dW = -p \cdot dV$), may be considered [53]

$$dU = dQ + dW = dQ - p \cdot dV \quad (2-32)$$

For an adiabatic process in which dQ equals zero and the change of internal energy is

$$dU = n \cdot c_v dT, \quad (2-33)$$

that the first law of thermodynamics becomes

$$n \cdot c_v dT = -p \cdot dV \quad (2-34)$$

in which c_v is the molar specific heat capacity of an ideal gas at constant volume and n is the number of moles. For an ideal gas, the pressure p can be substituted by the ideal gas equation of state

$$p = \frac{nRT}{V}, \quad (2-35)$$

with the universal gas constant

$$R = c_p - c_v, \text{ and } \gamma = \frac{c_p}{c_v} \quad (2-36)$$

As the ratio of specific heats γ (c_p = specific heat capacity of an ideal gas at constant pressure), one obtains, after several rearrangements and integration,

$$PV^\gamma = P_0V_0^\gamma = \text{constant} \quad (2-37)$$

This law of Poisson can be also written as

$$\frac{P}{P_0} = \left(\frac{V}{V_0} \right)^\gamma = \left(\frac{\rho}{\rho_0} \right)^\gamma \quad (2-38)$$

Thus, equation (2-29) becomes

$$K_{ad} = \left(\frac{dp}{d\rho} \right)_{\rho=\rho_0} \rho_0 = \gamma \cdot P_0 \quad (2-39)$$

As a result, the “stiffness” of gas during an adiabatic compression is γ -times higher than during an isotherm compression. This factor must be considered for wave propagation through gas. For liquids, it is not possible to derive an equation of state. In analogy to (2-38), though, empirical tests found the TAIT-equation for liquids [53]

$$\frac{P}{P_0} = \left(\frac{V}{V_0} \right)^n = \left(\frac{\rho}{\rho_0} \right)^n. \quad (2-40)$$

The value of n is an empirical parameter that describes the non-linear elastic behaviour of liquids.

2.3 Wave equation for plane wave propagation

The equation of motion (2-23), the equation of continuity (2-24), and the equation of state (2-31) together provide a system to calculate the three acoustical parameters p , ρ , and φ . The density is a function of pressure and therefore the derivative equals

$$\frac{\partial \rho}{\partial t} = \left(\frac{\partial \rho}{\partial p} \right) \left(\frac{\partial p}{\partial t} \right). \quad (2-41)$$

The derivative

$$\frac{\partial p}{\partial t} = \rho_0 \frac{\partial^2 \varphi}{\partial t^2} \quad (2-42)$$

can be evaluated by differentiating the equation of motion. Inserting (2-41) and (2-42) into (2-24) we obtain

$$\Delta \varphi = \frac{1}{c_0^2} \frac{\partial^2 \varphi}{\partial t^2} \quad (2-43)$$

in which

$$c_0 = \sqrt{\left(\frac{dp}{d\rho} \right)_{\rho=\rho_0}} = \sqrt{\frac{K_{ad}}{\rho_0}} \quad (2-44)$$

is the sound velocity of the propagating wave.

For a one-dimensional plane wave, the potential of the velocity is dependent on position x and time t , which leads to the wave equation for plane waves

$$\frac{\partial^2 \varphi}{\partial x^2} = \frac{1}{c_0^2} \frac{\partial^2 \varphi}{\partial t^2}. \quad (2-45)$$

The solution of (2-45) is given by

$$\varphi(x, t) = \varphi_{\max} e^{i2\pi \left(ft - \frac{fx}{c_0} \right)} = \varphi_{\max} e^{i(\omega t - kx)} \quad (2-46)$$

$$\text{or } \varphi(x, t) = \varphi_{\max} \sin 2\pi \left(ft - \frac{fx}{c_0} \right) = \varphi_{\max} \sin(\omega t - kx) \quad (2-47)$$

under consideration that the initial phase angle equals 0 and only the wave in positive direction is expressed, with the angular frequency

$$\omega = 2\pi f \quad (2-48)$$

and with the wave number

$$k = \frac{2\pi f}{c_0} = \frac{2\pi}{\lambda} \quad (2-49)$$

At $x = \text{const.}$, the phase angle varies between 0 and 2π within the time $T = f^{-1}$ and for $t = \text{const.}$ the phase shift of 2π takes place within the distance $x = c_0/f = \lambda$ (wave length). Similar solutions can be given for the other variable acoustic parameter like particle displacement, density, pressure, or particle velocity to express the wave propagation.

On its way, the wave undergoes sound attenuation so that the acoustical parameters are decreased along the propagating path. The reasons for attenuation are:

- reflection at boundaries (major effect for ultrasound inspection technique; sections 2.4 and 2.5),
- absorption (irreversible and reversible transformation of sound energy into other energy forms, described briefly in section 2.7),
- scattering at small heterogeneities (described very briefly in section 2.7), and
- diffraction (not described, because the lateral size of the plate is regarded as larger than the wave length).

2.4 Reflection and transmission of waves at a plane boundary

What happens if a wave hits the boundary between two media with different physical properties? Depending on the angle of incidence and the characteristics of the media, the wave is either

- totally reflected or partly reflected and refracted/transmitted, and/or
- probably split into a longitudinal and a transversal wave if at least the second medium is solid.

In this work, the focus is on wave beams with normal incidence to the boundaries because, as will be shown in the following chapters, measurements are performed in through-transmission technique with normal sound incidence. Therefore, only longitudinal waves are considered because shear waves are generated only by abnormal angles of incidence interaction at boundaries.

The basic consideration for the interaction between wave and boundary can be expressed as follows:

The particle velocity

$$v(x,t) = -\frac{\partial \varphi}{\partial x} = k\varphi_{\max} \cos(\omega t - kx) = v_{\max} \cos(\omega t - kx) \quad (2-50)$$

for the incident wave is calculated from equations (2-22) and (2-47). Furthermore, the potential of the particle velocity φ is derived with respect to time and multiplied with the density ρ_0 and becomes

$$p(x,t) = \frac{\partial \varphi}{\partial t} \rho_0 = \rho_0 \omega \varphi_{\max} \cos(\omega t - kx) = p_{\max} \cos(\omega t - kx). \quad (2-51)$$

Both equations are indicating that the particle velocity $v(x,t)$ and the changes of pressure $p(x,t)$ for the incident wave are in phase with each other and are coupled by

$$p(x,t) = \rho_0 c_0 v(x,t) = \rho_0 c_0 v_{\max} \cos(\omega t - kx) = p_{\max} \cos(\omega t - kx). \quad (2-52)$$

For a wave propagating in opposite direction ($\varphi(x,t) = \varphi_{\max} \sin(\omega t + kx)$; negative x-direction) one obtains

$$p(x,t) = -\rho_0 c_0 v(x,t) = -\rho_0 c_0 v_{\max} \cos(\omega t - kx) = \rho_0 c_0 v_{\max} \cos(\omega t - kx + \pi) \quad (2-53)$$

and in this case $p(x,t)$ and $v(x,t)$ have opposite phase relation to each other. The term

$$\rho_0 c_0 = Z_0 \quad (2-54)$$

represents the acoustic impedance Z_0 of a medium (similar to the electrical impedance) and expresses in (2-52) as well as in (2-53) the degree of the particle velocity for given pressure. The force caused by pressure that acts on a surface S equals

$$F_p = v \rho_0 c_0 S. \quad (2-55)$$

In general, the relation between $p(x,t)$ and $v(x,t)$ in a region where waves are propagating in positive and negative x- direction and are superimposing is characterized by the complex number

$$Z^* = \frac{p(x,t)}{v(x,t)} = \rho_0 c_0 \frac{e^{i(\omega t - kx)} + e^{i(\omega t + kx)}}{e^{i(\omega t - kx)} - e^{i(\omega t + kx)}} \quad (2-56)$$

where the imaginary term illustrates the phase shift between $p(x,t)$ and $v(x,t)$.

It is now possible to return to monochromatic plane wave propagating along the x -coordinate shown in Figure 9 and discuss its reflection and transmission at acoustic boundaries.

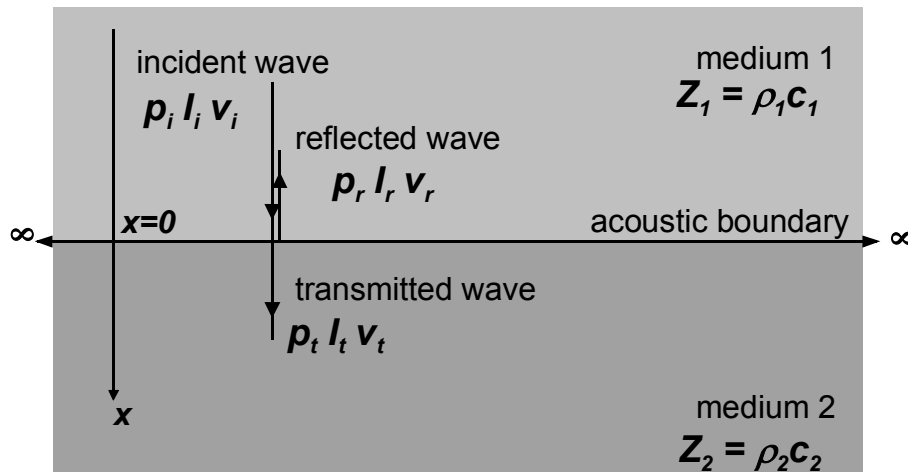


Figure 9: Reflection and transmission of a plane wave at normal incidence at an acoustic boundary of two media with different physical properties.

Medium 1 is characterised by the sound velocity c_1 , and by the density ρ_1 , the incident wave by the pressure p_i , and the particle velocity v_i . The wave reflected at the acoustic boundary is described by the pressure p_r , and the particle velocity v_r . Medium 2 and the transmitted wave are described correspondingly by c_2 , ρ_2 , p_t , v_t . The incident wave hits the boundary and causes harmonic oscillation of the particles on the boundary. The oscillating particles generate two waves that are propagating in opposite directions, the reflected wave and the transmitted wave. At the boundary, the sum of the particle velocities v of the incident wave and the reflected wave must equal the particle velocity of the transmitted ultrasound wave. In addition, because of the balance of the forces, the sum of the pressures of the incident wave and the reflected wave must equal the pressure of the transmitted ultrasound wave. Furthermore, the conservation of energy (I_i , I_r , I_t) must be considered. These considerations lead to the following boundary conditions at $x = 0$ [54]:

$$\left. \begin{aligned} v_i + v_r &= v_t \\ p_i + p_r &= p_t \\ I_i - I_r &= I_t \end{aligned} \right|_{x=0} \quad (2-57)$$

The correlation between the pressure and the particle velocity of the incident wave, the reflected wave, and the transmitted wave is given by

$$\begin{aligned} p_i &= \rho_1 c_1 v_i \\ p_r &= \rho_1 c_1 v_r \\ p_t &= \rho_2 c_2 v_t \end{aligned} \quad (2-58)$$

By combining equations (2-58) and (2-54), the equation (2-57) becomes

$$\left. \begin{aligned} v_i + v_r &= v_t \\ v_i Z_1 - v_r Z_1 &= v_t Z_2 \end{aligned} \right|_{x=0} \quad (2-59)$$

Substituting the particle velocities v in (2-57) by (2-58) and (2-54) leads to an analogue expression for the pressure

$$\left. \begin{aligned} \frac{p_i}{Z_1} - \frac{p_r}{Z_1} &= \frac{p_t}{Z_2} \\ p_i + p_r &= p_t \end{aligned} \right|_{x=0} \quad (2-60)$$

The ratio of the reflected wave to the values of the incident wave (reflection coefficient R) is related to the ratio of pressures (R_p), to the ratio of particle velocities (R_v), and to the ratio of energies (R_I). Correspondingly, the transmission coefficient (T_p , T_v , T_I) is the ratio of the values of the transmitted wave to the values of the incident wave. The coefficients are calculated using (2-57), (2-59), and (2-60)

$$\begin{aligned} R_p &= \frac{p_r}{p_i} = \frac{Z_2 - Z_1}{Z_2 + Z_1} \\ R_v &= \frac{v_r}{v_t} = -\frac{Z_2 - Z_1}{Z_2 + Z_1} \\ T_p &= \frac{p_t}{p_i} = \frac{2Z_2}{Z_2 + Z_1} \\ T_v &= \frac{v_t}{v_i} = \frac{2Z_1}{Z_2 + Z_1} \end{aligned} \quad (2-61)$$

These ratios are valid at all times for all values of pressure and particle velocities of the wave. By definition, the amplitude reflection coefficient is

$$R_\varphi \equiv \left| \frac{\varphi_r \max}{\varphi_i \max} \right| = \left| \frac{p_r \max}{p_i \max} \right| = \left| \frac{v_r \max}{v_i \max} \right| = \left| \frac{Z_1 - Z_2}{Z_1 + Z_2} \right|. \quad (2-62)$$

The energy reflection coefficient is

$$R_I = \frac{I_r}{I_i} = R_p^2 = \left(\frac{Z_1 - Z_2}{Z_1 + Z_2} \right)^2 \quad (2-63)$$

because the energy of a wave is proportional to the square of the pressure

$$I \sim p^2. \quad (2-64)$$

The transmission coefficient

$$T_I = \frac{I_t}{I_i} = 1 - R_I = \frac{4Z_1Z_2}{(Z_2 + Z_1)^2} \quad (2-65)$$

results from the conservation of energy (2-57) [55].

The significance of the different ratios can be illustrated with an example in which an ultrasound wave is transmitted from a piezo-electric ceramic ($Z_1 = 33 \cdot 10^6 \text{ kg/m}^2\text{s}$)

- into water ($Z_2 = 1.5 \cdot 10^6 \text{ kg/m}^2\text{s}$) and
- into air ($Z_2 = 0.00043 \cdot 10^6 \text{ kg/m}^2\text{s}$).

The calculated coefficients are given in Table 2. The reflection coefficient for the pressure amplitude R_p and for the particle velocity R_v always have a phase shift of 180° to each other, independent of the Z_1/Z_2 -ratio. If $Z_1/Z_2 > 1$ (shown in Table 2), the pressure amplitude of the reflected wave is 180° -phase shifted with respect to the incident wave. By comparison, there is no phase shift between ratios of the particle velocities for the incident and the reflected wave. With increasing Z_1/Z_2 the absolute values of R_p , R_v , and R_I approach 1. As a result, in the case of the solid-to-air boundary, approximately 99.99 % of the incident wave is reflected. Both the transmission coefficients T_p and T_v indicate that the pressure amplitude and the particle velocity of the transmitted wave are in phase with each other and in phase with the incident wave. Their values are dependent on whether the wave is transmitted from an “acoustical hard” medium into an “acoustical soft” medium ($Z_1/Z_2 \gg 1$) or vice versa ($Z_1/Z_2 \ll 1$).

coefficients	piezo-electric ceramic and water $Z_1/Z_2 = 22$	piezo-electric ceramic and air $Z_1/Z_2 = 76744$
R_p	-0.91	-0.99997
R_v	0.91	0.99997
R_ρ	0.91	0.99997
T_p	0.09	0.00003
T_v	1.91	1.99997
T_ρ	0.09	0.00003
R_I	0.83	0.99995
T_I	0.17	0.00005

Table 2: Calculated reflection and transmission coefficients for an elastic wave propagation from piezo-electric ceramic into water (second column) or air (third column).

If the wave is transmitted from the piezo ceramic into air, the value of the pressure amplitude is negligible (0.003 %), while the amplitude of the particle velocity is doubled. Also, only 0.005 % of the sound energy of the incident wave is transmitted from piezo ceramic into air. When piezo ceramics receive ultrasound from air (transmission from air into piezo ceramic; $Z_1/Z_2 \ll 1$), it is interesting to note that the pressure amplitude is nearly doubled.

For ultrasound measurements using reflection and through-transmission techniques it is useful to calculate and to compare the transmission coefficients for pressure amplitude T_p and for energy T_I at water-to-sample and air-to-sample boundaries. The calculated coefficients for a CFRP-sample are given in Table 3.

coefficients	boundary			
	water-to-CFRP	air-to-CFRP	CFRP-to-water	CFRP-to-air
T_p	1.5	2.0	0.5	$2 \cdot 10^{-4}$
T_I	0.75	$4 \cdot 10^{-4}$	0.75	$4 \cdot 10^{-4}$

Table 3: Transmission coefficients for pressure amplitude T_p and for energy T_I at water-to-CFRP, air-to-CFRP, CFRP-to-water, and CFRP-to-air boundaries. The acoustical impedances used are $Z_{water}: 1.5 \cdot 10^6 \text{ kg/m}^2\text{s}$, $Z_{air}: 0.00043 \cdot 10^6 \text{ kg/m}^2\text{s}$, and $Z_{CFRP}: 4.5 \cdot 10^6 \text{ kg/m}^2\text{s}$.

In the case of the water-to-CFRP boundary, the pressure amplitude T_p is increased by 150% while at the air-to-CFRP interface, it is doubled. By contrast, at the CFRP-to-

water boundary the pressure amplitude is halved and the resulting pressure amplitude of a wave travelling from CFRP into air is almost negligible. The transmission coefficients of energy T_I are independent of the direction the wave is propagating, whether from CFRP into water, or into air, or vice versa. With water as the surrounding medium, the loss is 25% while with air it is 99.96%.

The values of the different coefficients (Table 2, Table 3) show that it is much more efficient to perform measurements in a water bath than in air. For measurements through air, the huge impedance mismatch between solid and air must be reduced. This can be achieved either by using a matching layer between solid and the surrounding medium (section 2.6) or by reducing the impedance (density and sound velocity) of the piezo ceramic (section 5.2).

2.5 Transmission of a normal incident wave through a plate

In the section above, the transmission coefficients of a wave passing a single boundary was briefly explained. In this section the transmission of an ultrasound wave passing through a plate is described in more detail. A wave passing through a plate is reflected several times at the two inner surfaces (multi reflection). These reflected waves interact with each other and with the transmitted wave. Thus, at certain ratios of thickness d and wave length λ the sound pressure p is either increased or decreased at the boundaries and therefore the transmission and reflection coefficients have either a maximum or a minimum value.

The acoustic impedance of the surrounding medium is given by $Z_1 = \rho_1 \cdot c_1$ and the acoustic impedance of the plate by $Z = \rho \cdot c$ (Figure 10).

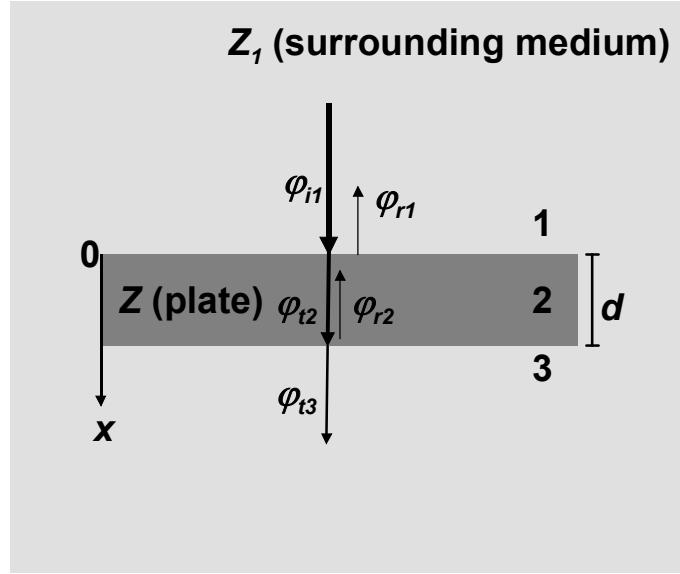


Figure 10: Wave propagation through a plate.

The wave propagates at normal incidence along the x -coordinate. The first boundary is at $x = 0$ and the second at $x = d$ (d : thickness of the plate). Each boundary is a source of a reflected and of a transmitted wave. The wave equation for the normal incident longitudinal wave that hits the first boundary is [54]

$$\varphi_{i1}(x, t) = \varphi_{i1\max} e^{i(\omega t - k_1 x)}, \quad (2-66)$$

for the wave reflected at the first boundary at $x = 0$

$$\varphi_{r1}(x, t) = \varphi_{r1\max} e^{i(\omega t + k_1 x)}, \quad (2-67)$$

and for the wave transmitted through the first boundary

$$\varphi_{t2}(x, t) = \varphi_{t2\max} e^{i(\omega t - kx)} = \varphi_{t2}. \quad (2-68)$$

At the second acoustic boundary the transmitted wave is again reflected

$$\varphi_{r2}(x, t) = \varphi_{r2\max} e^{i(\omega t + k_1 x)} \quad (2-69)$$

and transmitted

$$\varphi_{t3}(x, t) = \varphi_{t3\max} e^{i(\omega t - k_1 x)}. \quad (2-70)$$

As shown in section 2.4, the boundary condition must be steady for pressure, for the particle velocity, and for the potential of the velocity. As a result, the velocity potentials at $x = 0$ are

$$\left. \begin{aligned} \rho_1 \cdot (\varphi_{i1} + \varphi_{r1}) &= \rho \cdot (\varphi_{t2} + \varphi_{r2}) \\ k_1 \cdot (\varphi_{i1} - \varphi_{r1}) &= k \cdot (\varphi_{t2} - \varphi_{r2}) \end{aligned} \right|_{x=0}. \quad (2-71)$$

The potentials at $x = 0$ become

$$\varphi(0, t) = \varphi_{\max} e^{i(\omega t)} \text{ etc.} \quad (2-72)$$

At the second boundary at $x = d$, the potentials differ from the previous ones by the factors $e^{i(\pm kd)}$ and $e^{i(-k_1 d)}$:

$$\begin{aligned} \rho \left[\varphi_{t2}(0) \cdot e^{-ikd} + \varphi_{r2}(0) \cdot e^{ikd} \right] &= \rho_1 \cdot \varphi_{t3}(0) \cdot e^{-ik_1 d} \\ k_1 \left[\varphi_{t2}(0) \cdot e^{-ikd} - \varphi_{r2}(0) \cdot e^{ikd} \right] &= k_1 \cdot \varphi_{t3}(0) \cdot e^{-ik_1 d} \end{aligned} \Bigg|_{x=d} \quad (2-73)$$

After eliminating the potentials φ_{t2} and φ_{r2} in equations (2-71) and (2-73), the total reflection coefficient for pressure equals

$$R_{p_{total}} = \frac{\varphi_{r1}}{\varphi_{i1}} = \frac{\frac{k\rho_1}{k_1\rho} - \frac{k_1\rho}{k\rho_1}}{\sqrt{\left[\frac{k\rho_1}{k_1\rho} + \frac{k_1\rho}{k\rho_1} \right]^2 + 4 \cot^2(d \cdot k)}} \quad (2-74)$$

This equation can be rewritten considering the acoustical impedances

$$\frac{k\rho_1}{k_1\rho} = \frac{2\pi f \rho_1 c_1}{2\pi f \rho c} = \frac{Z_1}{Z} \text{ and } \frac{k_1\rho}{k\rho_1} = \frac{Z}{Z_1} = m \quad (2-75)$$

and equals

$$R_{p_{total}} = \frac{\varphi_{r1}}{\varphi_{i1}} = \frac{\frac{1}{m} - m}{\sqrt{\left(\frac{1}{m} + m \right)^2 + 4 \cot^2(d \cdot k)}} \quad (2-76)$$

The energy reflection coefficient according to Rayleigh [55]

$$R_{I_{total}} = \left(R_{p_{total}} \right)^2 = \frac{\left(\frac{1}{m} - m \right)^2}{\left(\frac{1}{m} + m \right)^2 + 4 \cot^2(d \cdot k)} = \frac{\frac{1}{4} \left(m - \frac{1}{m} \right)^2 \sin^2(d \cdot k)}{1 + \frac{1}{4} \left(m - \frac{1}{m} \right)^2 \sin^2(d \cdot k)} \quad (2-77)$$

is the second power of the pressure reflection coefficient R_p , and the energy transmission coefficient is

$$\begin{aligned}
T_{I_{total}} &= 1 - (R_{p_{total}})^2 = \frac{4m^2}{4m^2 \cos^2(d \cdot k) + (m^2 + 1)^2 \sin^2(d \cdot k)} = \\
&= \frac{1}{1 + \frac{1}{4} \left(m - \frac{1}{m}\right)^2 \sin^2(d \cdot k)} .
\end{aligned} \tag{2-78}$$

Therefore, the ratio $R_{I_{total}}/T_{I_{total}}$ becomes

$$\frac{R_{I_{total}}}{T_{I_{total}}} = \left[\frac{1}{2} \left(m - \frac{1}{m}\right) \sin(kd) \right]^2 . \tag{2-79}$$

It can be seen that equations (2-77), (2-78), and (2-79) do not change if m is replaced by $1/m$. As a result, it makes no difference whether the wave propagates from a medium with high impedance into a medium with low impedance or visa versa. The validity of these equations evaluated by Rayleigh was proved by Boyle measuring plates made out of different types of metals [56].

The dependence of the total energy transmission coefficient $T_{I_{total}}$ on the sample thickness d is calculated for a CFRP-plate (1) in water and (2) in air, at a given frequency of 450 kHz to examine the dependence of the transmission coefficient T for measurements in through-transmission technique. The results are shown in Figure 11 and in Figure 12. For $d \cdot k = n\pi$, the term $\cot^2(d \cdot k) = \infty$ (equation (2-76)) and as a result $R_p = R_I = 0$. Thus, for

$$\frac{d}{\lambda} = \frac{n}{2}; n \in \mathbb{N} \tag{2-80}$$

the transmission coefficient $T_I = 1$ and the entire wave is transmitted through the plate without reflection. Alternatively, for

$$\frac{d}{\lambda} = \frac{(2n+1)}{4}; n \in \mathbb{N}_0 \tag{2-81}$$

the term $\cot^2(d \cdot k) = 0$ and as a result the reflection coefficients reach their maximum absolute value for a given Z_1/Z -ratio.

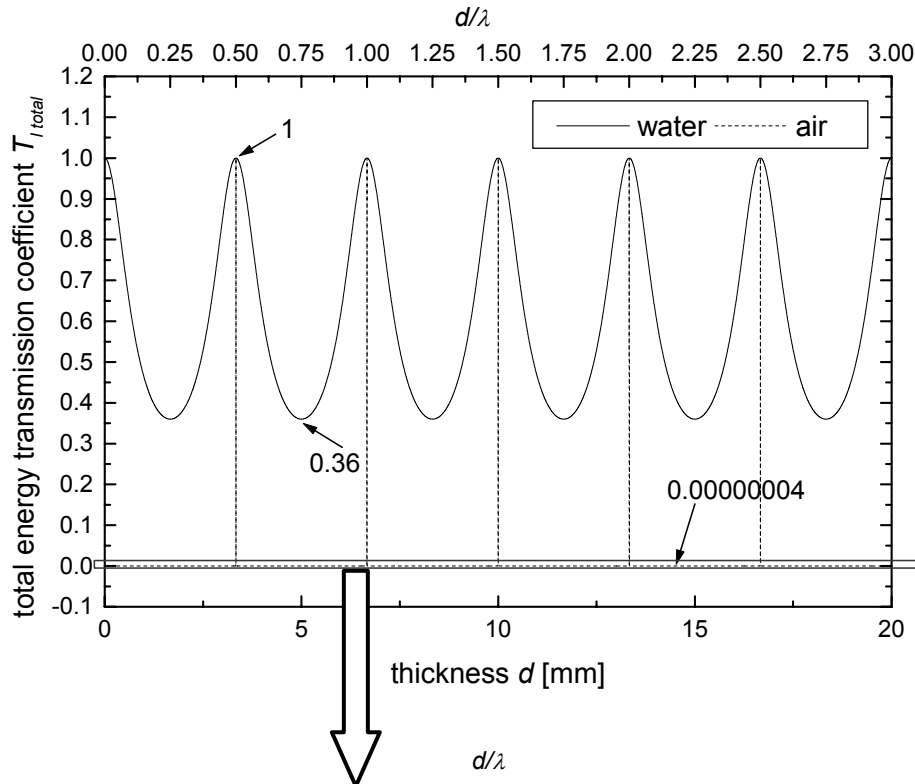


Figure 11: Total transmission coefficient as a function of thickness and d/λ with $\lambda = 6.67$ mm; $f = 450$ kHz for water and air as surrounding media and a CFRP-plate ($c = 3$ km/s).

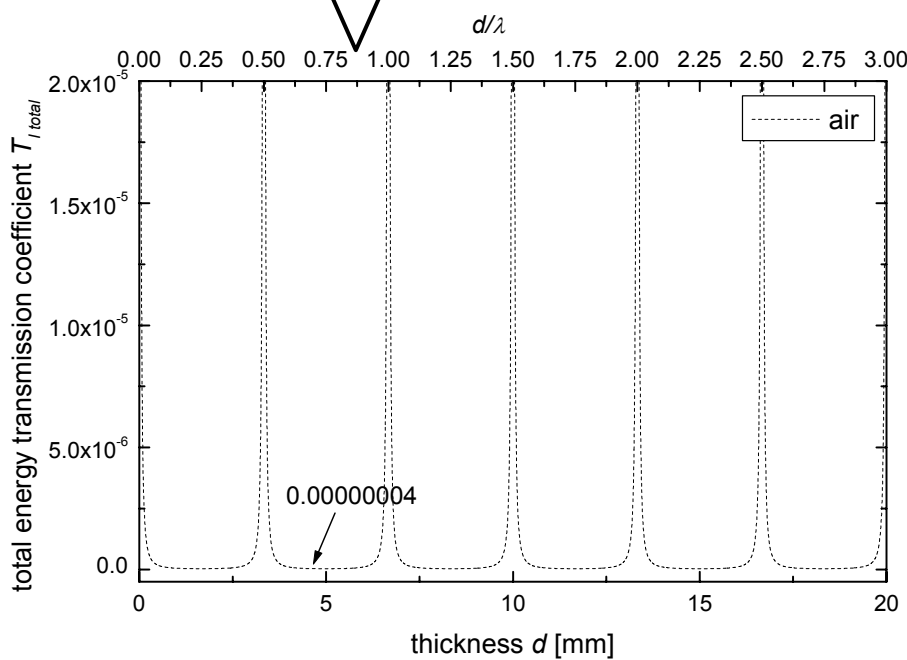


Figure 12: Total transmission coefficient as a function of thickness and d/λ with $\lambda = 6.67$ mm; $f = 450$ kHz for air as surrounding medium and a CFRP-plate ($c = 3$ km/s).

After some rearrangements, the energy reflection coefficient becomes

$$R_{I \max \text{ total}} = \left(\frac{m - \frac{1}{m}}{m + \frac{1}{m}} \right)^2 \quad (2-82)$$

for its maximum value. Under the same boundary conditions, the energy transmission coefficient reaches its minimum value

$$T_{I \min total} = \left(\frac{\frac{2}{m}}{\left(\frac{1}{m}\right)^2 + 1} \right)^2 \quad (2-83)$$

The values of the coefficients are listed in Table 4.

plate CFRP ($Z = 4.5 \cdot 10^6 \text{ kg/m}^2\text{s}$)	surrounding medium water ($Z_1 = 1.5 \cdot 10^6 \text{ kg/m}^2\text{s}$)	surrounding medium air ($Z_1 = 0.00043 \cdot 10^6 \text{ kg/m}^2\text{s}$)
total energy reflection coefficient $R_{I \max total}$	0.64	0.99999996
total energy transmission coefficient $T_{I \min total}$	0.36	0.00000004

Table 4: Calculated coefficients from equations (2-82) and (2-83).

The minimum of the total energy transmission coefficient is 0.36 for water while the value for air is seven orders of magnitude smaller. Thus, almost no energy is transmitted from the air into a CFRP-plate and transmitted back into the air. With water as a surrounding medium, the curve is much smoother than for air. The area in which the transmission coefficient is close to the minimum is also much smaller than for air. With air as a surrounding medium, there is only an extremely small and sharp peak for high transmission values. This huge contrast between the behaviour in water and air is shown in Figure 11 in which the scaling was chosen in order to reveal both curves entirely. The curve for air appears like a delta-function because of this scaling. This appearance is caused by the small absolute changes of the values for air. A graph with an enlarged ordinate is displayed in Figure 13 which shows the values for air coupling close to zero.

2.6 Matching layer

The transmission coefficient of two media (e.g. piezo-electric ceramic Z_{pc} and air Z_a) with highly different acoustic impedances can be reduced by using a matching layer (thickness d). This is done by an interface placed between the two media. Thus, the

wave passes two acoustic boundaries of three media with three different acoustic impedances (Figure 13).

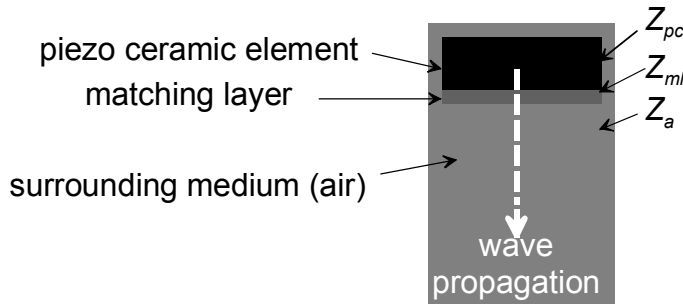


Figure 13: Impedance matching layer between piezo-electric ceramic and air to increase the transmission coefficient between solid and air.

The total energy transmission coefficient is given by [54,57]

$$T_{I_{total}} = \frac{4 \cdot Z_{pc} \cdot Z_a}{\left(\frac{Z_a}{Z_{pc}} + 1\right)^2 - \left(\left(\frac{Z_a}{Z_{ml}}\right)^2 - 1\right) \cdot \left(\left(\frac{Z_{ml}}{Z_{pc}}\right)^2 - 1\right) \cdot \sin^2 kd} \quad (2-84)$$

If $\lambda \ll d$ and as a result $kd \ll 1$ (k : wave number of the matching layer; λ : wave length inside the matching layer) or $\sin kd = 0$ ($kd = n\pi$, $n \in \mathbb{N}_0$), this equation equals the equation for the energy transmission coefficient for two media (2-65). In this case, the transmission coefficient for the three media is not dependent on the acoustic impedance of the matching layer. Another and more interesting case is if $\sin kd = 1$. This is true for $d = (2n + 1) \lambda/4$ so that the initial and the reflected waves are out of phase by $\lambda/2$ which corresponds to opposite sign of the wave. Such layers with a thickness of $\lambda/4$ are commonly used in optics for antireflection coating of lenses. Because the ideal thickness depends on λ , the matching layer is only suitable for one specific frequency. For $\sin kd = 1$ the equation (2-84) can be written as

$$T_{I_{total}} = \frac{4 \cdot Z_{pc} \cdot Z_a}{Z_{ml}^2 \left(1 + \frac{Z_{pc} \cdot Z_a}{(Z_{ml})^2}\right)^2} \quad (2-85)$$

The transmission coefficient $T_{I_{total}}$ becomes 1 and the elastic wave is transmitted without any losses from the piezo electric ceramic into air for

$$Z_{ml} = \sqrt{Z_{pc} \cdot Z_a} \quad (2-86)$$

Therefore, the reflection coefficients must be equal for the two boundaries:

$$R_{pc/ml} = R_{ml/a} \quad (2-87)$$

The value of Z_{ml} would ideally be $0.12 \cdot 10^6$ kg/m²s. Unfortunately, a material that has such an acoustic impedance does not exist. As a consequence, efforts are being made to develop porous soft rubber materials (e.g. silicone rubber with air bubbles $Z \approx 0.0084 \cdot 10^6$ kg/m²s – $0.0835 \cdot 10^6$ kg/m²s) to use as a matching layer for piezo-electric ceramic ultrasound transducers [58,59,60,61].

2.7 Acoustical attenuation

During the propagation of a wave inside a medium, the amplitude of the variable acoustic parameters decreases exponentially (reflection is not considered) due to internal effects along its path by

$$v_{\max}(x) = v_{\max 0} e^{-\alpha x} \quad (2-88)$$

with the attenuation coefficient α . Also the intensity of a wave is reduced by

$$I_{\max}(x) = I_{\max 0} e^{-2\alpha x} \quad (2-89)$$

Thus, the relation (2-54) can be rewritten with the particle velocity v and equation (2-88)

$$v(x, t) = v_{\max 0} e^{-\alpha x} e^{i(\omega t - kx)} \quad (2-90)$$

2.7.1 Sound attenuation in gases and liquids

The sound attenuation in gases and liquids $\alpha(f) = \alpha_r(f) + \alpha_t(f) + \alpha_{st}$ is caused primarily by inner friction effects. According to Stokes [62], the first portion of the attenuation coefficient equals

$$\alpha_r = \frac{8}{3} \frac{\pi^2 \eta}{c_0^3 \rho_0} f^2 = \frac{8}{3} \frac{\pi^2 \eta}{\lambda^2 Z} \quad (2-91)$$

is proportional to the second power of the frequency, and in which η is the coefficient for inner friction (viscosity). The second term α_t that affects the sound attenuation is caused by the thermal conductivity of the medium in which the wave is propagating. In section 2.2.2, the propagation is considered to be an adiabatic process (no heat flow). Whenever a compression of volume elements occurs, though, these elements are heated. Thus, because of the thermal conductivity with the surrounding elements, heat

flow takes place. This irreversible process leads to a decrease of the amplitude. This portion is expressed by [63]

$$\alpha_l = \frac{2\pi^2}{c_0^3 \rho_0} \frac{\gamma-1}{c_p} \lambda_h f^2 = \frac{2\pi^2}{\lambda^2 Z} \frac{\gamma-1}{c_p} \lambda_h \quad (2-92)$$

with the coefficient of the thermal conductivity λ_h . By using the expressions given in section 2.2.2 equation (2-92) can be rewritten and becomes [64]

$$\alpha_l = \frac{2\pi^2 c_0 \lambda_h T a_{ex}^2}{\lambda^2 \rho_0 W c_p^2} \quad (2-93)$$

with the thermal extension coefficient a_{ex} . The third term α_{st} considers the heat radiation as a portion of the attenuation coefficient [65]

$$\alpha_{st} = \frac{1}{2c_0} \frac{\gamma-1}{\gamma} q \quad (2-94)$$

with the cooling coefficient q . This effect is so minor that it does not need to be considered (amplitude is decreased by -6 dB at a distance of 140 km).

Both the attenuations caused by inner friction and by thermal conductivity are proportional to the square of the frequency and the values are listed in tables divided by the second power of the frequency. The theoretical and the measured values for air and water are shown in Table 5.

media	$(\alpha_r/f^2)*10^{17}$ [s ² /cm]	$(\alpha_l/f^2)*10^{17}$ [s ² /cm]	theoretical value $(\alpha/f^2)*10^{17} =$ $[(\alpha_r/f^2) +$ $+ (\alpha_l/f^2)]*10^{17}$ [s ² /cm]	measured value $(\alpha/f^2)*10^{17}$ [s ² /cm]
water	8.5	0.0064	8.5064 \approx 8.5	25
air	0.000087	0.000037	0.000124	0.000199

Table 5: Theoretical and measured values of the wave attenuation coefficients for water and air.

From this table, several conclusions can be drawn:

- In water (and in liquids in general) the absorption caused by thermal conductivity is much lower than the term for inner friction. Thus, this term is often ignored.

- In air (and in gases in general) the absorption coefficient is lower than in water and the absorption caused by thermal conductivity can not be ignored because it is about 1/3 of the value for absorption caused by friction.
- The values measured for absorption in air and especially in water are much higher than the theoretical values. The reason is that many types of molecular processes occur, such as vibration of molecules, rotation of molecules, translation of molecules, and various types of relaxation processes. These processes are taken into account by Kneser [66,67,68] and the measured values can be proved by his considerations.

The distance a wave (frequency: 450 kHz) travels in water and air before its amplitudes are decreased to 1/e is given in Table 6.

	calculated with the theoretical value	calculated with the measured value
$x_{1/e}$ in water [cm]	581000 (= $5.81 \cdot 10^8$ mm)	197500 (= $1.98 \cdot 10^8$ mm)
$x_{1/e}$ in air [cm]	40 (= 400 mm)	25 (= 250 mm)

Table 6: Distance $x_{1/e}$ after which the sound amplitude is reduced to 1/e because of attenuation in water and in air (frequency: 450 kHz).

For air-coupled ultrasound inspection, it is interesting to notice that if the focal length of a transducer is only a few centimetres, the sound attenuation in air does not play an important role.

2.7.2 Sound attenuation and scattering in solids

Sound attenuation and scattering in solids are the energy-loss mechanisms of interest to characterize engineering materials. Absorption losses from material damping, relaxation, thermoplastic effects, and anelastic hysteresis are intrinsic (absorption) mechanisms related to the material properties (elastic properties, density). Diffusion scattering losses, stochastic (phase) scattering losses, and Rayleigh scattering losses, however, are extrinsic mechanisms related to small “heterogeneities” like fibres and pores.

In solids, wave propagation is linked to an elastic deformation of a body (vibration of particles; section 2.1) and because of inner damping (stress-strain damping) the acous-

tic energy is converted to heat (hysteresis losses). For hysteresis, the loss factor is [62]:

$$\varepsilon_h(f) = \frac{8\pi}{3} \frac{(1+\mu)}{E} \eta \cdot f \Rightarrow \varepsilon_h \sim f. \quad (2-95)$$

Thus, the loss due to hysteresis is dependent on the Poisson's number μ , the Young's modulus E , and friction η , and has a first power frequency dependence. The absorption coefficient presented in equation (2-88) and the loss factor ε_h are related to each other according to [69]

$$\alpha = \frac{\pi}{\lambda} \varepsilon_h = \frac{8\pi^2}{3c_0} \frac{(1+\mu)}{E} \eta \cdot f^2 \Rightarrow \alpha \sim f^2. \quad (2-96)$$

Like in gases and liquids, thermodynamic losses arise because travelling waves are accompanied by heat flow from compression to dilatation regions ($\alpha \sim f^2$ equation (2-92)). In solids, viscous losses ($\alpha \sim f^2$ equation (2-91)) are small and are in general negligible.

In most cases, scattering occurs because of additional boundaries like grain boundaries in metals, pores in ceramics, and fibres in reinforced polymers. Each boundary serves as a reflector that emits its own reflected and scattered signal. Also multi scattering is possible. As a result, the amplitude of the ultrasound wave is reduced. Compared to metals, composites have higher sound attenuation in general because of their heterogeneous nature and properties. The attenuation caused by scattering is also a function of the frequency f and of mean scatterer size \tilde{a} . In general there are three scatter processes known that are defined by value of $k\tilde{a}$ [50,70,71]:

- for $k\tilde{a} \ll 1$ the scattering process is proportional to f^4 (Rayleigh scattering),
- for $k\tilde{a} \approx 1$ the scattering process is proportional to f^2 (stochastic (phase) scattering) and,
- for $k\tilde{a} \gg 1$ the scattering process is proportional to $1/\tilde{a}$ (diffusion scattering).

The theories used to describe the scattering processes usually consider ensembles of scattering centres embedded in featureless continua and non-compressible spheres.

Thus, along its propagation path a wave undergoes all sorts of attenuation processes like reflection (independent from distance), sound absorption in different media, and wave scattering. The total attenuation coefficient is therefore a combined expression

which includes a sum of different coefficients. As a result, in ultrasound inspection the wave amplitude is changing. These variations of amplitude are displayed in images to display potential defects (section 4.4).

2.8 Focusing of ultrasound beams

For non-destructive testing, it is of great importance to localize defects. Therefore, focusing of the ultrasound beams to obtain a defined focal spot and to increase the intensity within this point is of interest. One of the options is forming the piezo ceramic plate into a spherical convex shape (Figure 14).

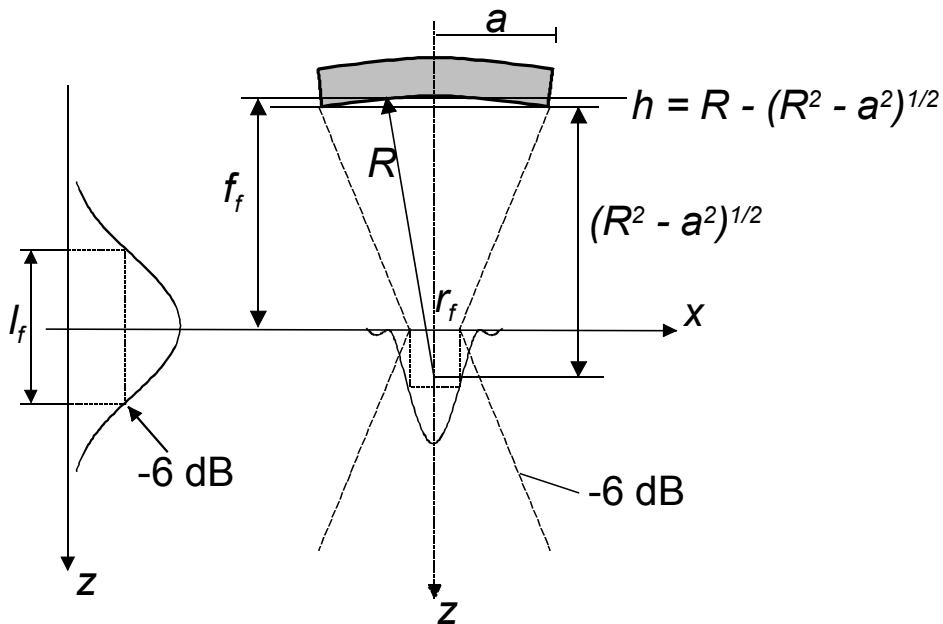


Figure 14: Focusing of ultrasound beam.

The focal length f_f can be calculated by [72]

$$f_f = R - \frac{12}{(kh)^2 + 12} \tag{2-97}$$

with the radius of curvature R , the aperture radius a , the wave number k and $h = R - \sqrt{R^2 - a^2}$. The relative distribution of the intensity along the focal plane shows a circular diffraction pattern with maxima and minima in amplitude (side-loops) with a maximum in the centre. The radius r_f from the centre in which the maximum intensity is reduced to half (-6 dB) around the focal point is given by [73]

$$r_f = 0.257 \frac{\lambda f_f}{a}. \quad (2-98)$$

The ratio of the value for air / water for a given frequency and for the same f_f/a is the ratio of the sound velocities in air and water and becomes

$$\frac{r_{f_{air}}}{r_{f_{water}}} = \frac{330 \text{ m/s}}{1490 \text{ m/s}} = 0.22. \quad (2-99)$$

Thus, the focal spot in air is 4.5 times smaller than in water and therefore the resolution is 4.5 times better. Also along the z-direction, the focus has a finite extension ("focal tube"; length: l_f). The distribution along the z-direction around the geometrical focal point can be approximated by [74]

$$I(z) \approx I_{\max} \left(\frac{\sin \chi}{\chi} \right)^2 \text{ with } \chi = \frac{\pi z}{2 \lambda} \left(\frac{a}{f_f} \right)^2. \quad (2-100)$$

The intensity is decreased by 6 dB for $\chi = \pm 1.39$ at $z = 0.89 \cdot \lambda \cdot (f_f/a)^2$. The length of the focal tube is twice of this characteristic distance and becomes

$$l_f = 1.8 \lambda \left(\frac{f_f}{a} \right)^2. \quad (2-101)$$

Also the focal tube length is 4.5 shorter in air than in water. Furthermore, the maximum sound intensity I_{\max} at the geometrical focal point is

$$I_{\max} = \left(\frac{1}{\lambda} \right)^2 \left(\frac{\pi a^2}{f_f} \right)^2 \cdot I_0 \quad (2-102)$$

where I_0 is the initial sound intensity at the transducer [73]. The maximum intensity at the focal point in air is 20 times higher than in water.

3 Non-Linear Acoustics

In the sections above, the acoustic wave amplitude was regarded as being infinitesimally small; the response of the materials is assumed to be linear to the excitation signal and to follow Hooke's Law. This expectation is based on the linear elastic properties of materials. As a result, the wave propagation with infinitesimally small displacements u is described by:

$$\frac{\partial^2 u}{\partial t^2} = c_0^2 \frac{\partial^2 u}{\partial x^2} \quad (3-1)$$

with the velocity of sound c_0 for an infinitesimal amplitude. This formula (3-1) is equivalent to the equations shown in (2-14) and (2-45). The variable acoustic parameter φ (potential of the particle velocity) is replaced by the particle displacement u as a variable acoustic parameter.

3.1 "Classical" non-linear acoustics

"Classical" non-linear behaviour (distortion of propagating waves) of media gases, liquids, and solids is well discussed in the literature [75,76,77,78,79] and the major topics are summarized in the following subsections.

3.1.1 "Classical" non-linear behaviour of gases and liquids

For finite displacement of particles u out of their equilibrium, the parabolic curve assumption for small displacements (Figure 4) is not valid. Therefore, in order to express the wave propagation the non-linear terms of the equation of motion, the equation of continuity, and the equation of state (sections 2.2 and 2.3) must be considered. Therefore, one obtains the non-linear equation of motion [80]

$$\frac{\partial^2 u}{\partial t^2} = \left(\frac{\rho}{\rho_0} \right)^2 \left(\frac{\partial p}{\partial \rho} \right) \frac{\partial^2 u}{\partial x^2} \quad (3-2)$$

with static and dynamic densities ρ_0 and ρ respectively for a one-dimensional acoustic wave propagating along the x -coordinate. In this case, the phase velocity c is not constant and depends on the two sources of non-linearity: density and pressure (the two factors in the right hand side of (3-2)). The non-linear equation

$$\frac{\partial^2 u}{\partial t^2} = c_0^2 \left[1 - (\gamma - 1) \frac{\partial u}{\partial x} + \dots \right] \frac{\partial^2 u}{\partial x^2}, \quad (3-3)$$

with the amplitude-dependent phase velocity c can be obtained from (3-2) by considering the continuity relation

$$\rho_0 = \rho \left(1 + \frac{\partial u}{\partial x} \right), \quad (3-4)$$

Poisson's law (2-38), and by retaining the quadratic terms in $\partial u / \partial x$. Finally, the local phase velocity c with which each point of wave is propagating becomes

$$c = c_0 + \frac{\gamma + 1}{2} v \quad (3-5)$$

after substituting $-\partial u / \partial x$ by v / c_0 , keeping only the first two terms in the square brackets of equation (3-3) because $\partial u / \partial x \ll 1$, and expansion in series. Thus, the local phase velocity c depends on the local particle velocity v and furthermore the degree of dependence is given by the adiabatic constant γ (equation (2-36)). The degree of non-linearity is expressed by the coefficient of the second-order acoustic non-linearity

$$\beta_2 = \frac{1}{2} (\gamma + 1). \quad (3-6)$$

For gases, the non-linearity coefficient β_2 is between 1 and $\cong 1.4$. For air in particular, $\beta_2 = 1.2$ [48,54]. For liquids (adiabatic process), the coefficient β_2 can also be expressed by the ratio of the compression module B/K if an adiabatic process (section 2.2.2) is taken into account [54]:

$$\beta_2 = \left(\frac{B}{K} + 2 \right). \quad (3-7)$$

The non-linear parameters for liquids in general are larger than those for gases and range from $\cong 2.5$ to $\cong 6.5$. For water the value equals 3.5 [48].

3.1.2 "Classical" non-linear behaviour of solids

For solid media, the equation of state is a series expansion of the stress-strain relation. Its quadratic approximation for a longitudinal plane wave in an isotropic solid turns the equation of motion (3-3) into [80]

$$\frac{\partial^2 u}{\partial t^2} = c_0^2 \left[1 + \frac{C^{III}}{C^{II}} \frac{\partial u}{\partial x} + \dots \right] \frac{\partial^2 u}{\partial x^2}. \quad (3-8)$$

Thus, the non-linear coefficient becomes

$$\beta_2 = -\frac{C^{III}}{2C^{II}} = -\frac{C^{III}}{2\rho_0 c_0^2}, \tag{3-9}$$

in which C^{III} includes the second- and third-order elastic constants. For solids, the non-linear parameter ranges between 2.0 (silver) and ~ 800 (marble) [48].

3.1.3 Wave form distortion

Because of the non-linear behaviour of media, a monochromatic wave distorts during its propagation. This distortion is described by the expression for the particle velocity v by combining equations (2-47) and (3-5)

$$\begin{aligned} v(x,t) &= v_0 \sin \omega \left(t - \frac{x}{c_0 + \beta_2 v} \right) = v_0 \sin \omega \left(t - \frac{x}{c_0(1 + \beta_2 M)} \right) \cong \\ &\cong v_0 \sin[\omega t - kx(1 - \beta_2 M)] \end{aligned} \tag{3-10}$$

in which $M = v/c_0$ is the acoustic Mach number. The wave forms given by this equation are shown in Figure 15 a-d.

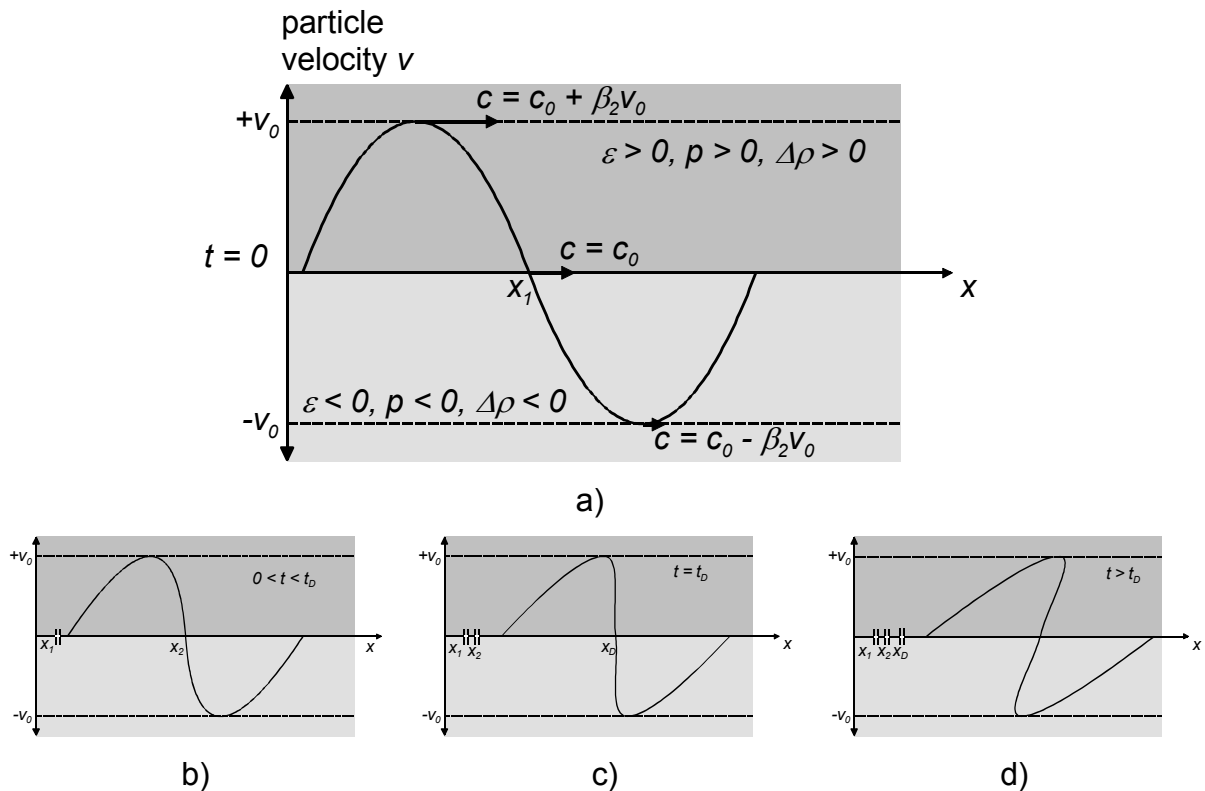


Figure 15: Distortion of a propagating monochromatic wave due to non-linear behaviour of the medium; a) initial wave after launching ($t=0$); b) propagating wave for $t>0$; c) wave at distance x_D (discontinuity distance) and $t=t_D$; d) hypothetic wave form for $x>x_D$ and $t>t_D$.

The drawings display the wave propagation at several distances and times after the wave has been launched. Directly after launching (Figure 15 a), the wave has the typical sinusoidal wave form. Each point travels along the x-direction at different phase velocity c . After a certain time t_D and distance x_D (discontinuity distance), the wave becomes either a N-type wave (if $\beta_2 < 0$) or a saw-tooth-like wave for $\beta_2 > 0$ (shock wave [81]; Figure 15 c). For all gases and all liquids and most solids, the value of $\beta_2 > 0$. For some solids like fused silica or glass, however, the non-linear coefficient β_2 is negative [82]. The maximum slope of the particle velocity profile v has a maximum slope at $v = 0$ and turns out after calculating the first derivative of (3-10) as

$$\left(\frac{\partial v}{\partial x}\right)_{v=0} = \frac{v_0 k (1 - \beta_2 M)}{1 - v_0 \left(\frac{k \beta_2 x}{c_0}\right)} \quad (3-11)$$

and becomes steeper with increasing x . At x_D , the slope $\left(\frac{\partial v}{\partial x}\right)_{x=x_D} = \pm\infty$ and, it can

be seen that the derivative becomes negatively infinite for a saw-tooth like wave for

$$x_D = \frac{c_0^2}{\varepsilon_0 \omega v_0} = \frac{1}{k \beta_2 M_0} \quad (3-12)$$

in which $M_0 = v_0/c_0$ is the amplitude Mach number. For example, two waves propagating with the same frequency and the same maximum particle velocity v_0 , one in water and one in air, the ratio of $x_{D\text{water}}/x_{D\text{air}} \approx 6$ ($\beta_{2\text{water}} = 3.5$; $\beta_{2\text{air}} = 1.2$). Thus, a wave in water travels approximately six times further before it reaches x_D . According to equation (3-12), values $x > x_D$ are also possible. This possibility gives a hypothetical wave form (Figure 15 d), though, because the dissipative properties of media are not taken into account in equation (3-10). If these properties are considered (viscosity, thermal conductivity in liquids and gases, internal friction in solids), the non-linear wave form distortion results in a weak shock wave form shown in Figure 15 c.

3.1.4 Generation of higher harmonics

Non-linear wave form distortion results in the occurrence of additional frequencies. In addition to the fundamental frequency ω , higher harmonics $n \cdot \omega$ ($n \in \mathbb{N} \setminus \{1\}$) can be found in the frequency spectrum. The frequency spectrum and the amplitudes of the

higher harmonics of a distorted wave can be obtained by transforming equation (3-10) into Fourier-series [54]:

$$u(x, t) = u_0 \sum_{n=1}^{\infty} B_n \sin n(\omega t - kx), \quad x < x_D, \quad (3-13)$$

with

$$B_n = \frac{1}{\pi} \int_0^{2\pi} \sin(\omega t - kx + \beta_2) \sin n(\omega t - kx) d(\omega t - kx). \quad (3-14)$$

The integration of (3-14) yields

$$B_n = 2 \frac{x_D}{nx} J_n \left(\frac{nx}{x_D} \right) \quad (3-15)$$

for $n \in \mathbb{N}$ and with the n -th-order (first kind) Bessel function J_n [83]. Putting (3-15) in (3-13) one eventually obtains the equation [48,54,84]

$$u(x, t) = 2u_0 \sum_{n=1}^{\infty} \frac{J_n \left(\frac{nx}{x_D} \right)}{\left(\frac{nx}{x_D} \right)} \sin n(\omega t - kx) \quad (3-16)$$

which describes the spectral content and the higher-harmonic amplitudes of a wave with finite amplitude as a function of the sound path length x to the discontinuity distance x_D . Along its path, the acoustic wave loses increasingly greater amounts of its monochromatic wave characteristic; increasing number of higher harmonics are generated and their amplitudes increase with distance while the amplitude of the fundamental frequency decreases because of energy transfer to the higher harmonics.

3.2 “Non-classical” non-linear acoustics

“Classical” non-linearity describes the wave-form distortion in homogenous media. For heterogeneous media such as gases with particles, liquids with bubbles, and solid materials with interfaces, there is a completely different behaviour. In solids, the non-linear effects of heterogeneities and all types of defects, like delaminations of layers, impact damages, or cracks in particular, are explained in this section. Inclusions have an internal non-bonded, partially bonded (“clapping”), or ideally bonded interface between the inclusion and the intact material. Such contact interfaces are strong local sources for non-linear phenomena because of non-linear motion of boundaries (contact acoustic

non-linearity (CAN) [85]). The motion occurs in normal as well as in tangential directions or in mixed modes.

3.2.1 Normal traction driven interfaces

The non-linear properties of non-bonded contacts driven by normal traction can be described by the general form of NDT-techniques (Figure 4) and in particular as shown in Figure 16: A longitudinal plane wave is launched into a sample (Figure 16 a). If it hits a non-bonded contact, it drives the interface with

$$\varepsilon(t) = \varepsilon_{\max} \cos(\omega_0 t) \quad (3-17)$$

in which ε is the strain.

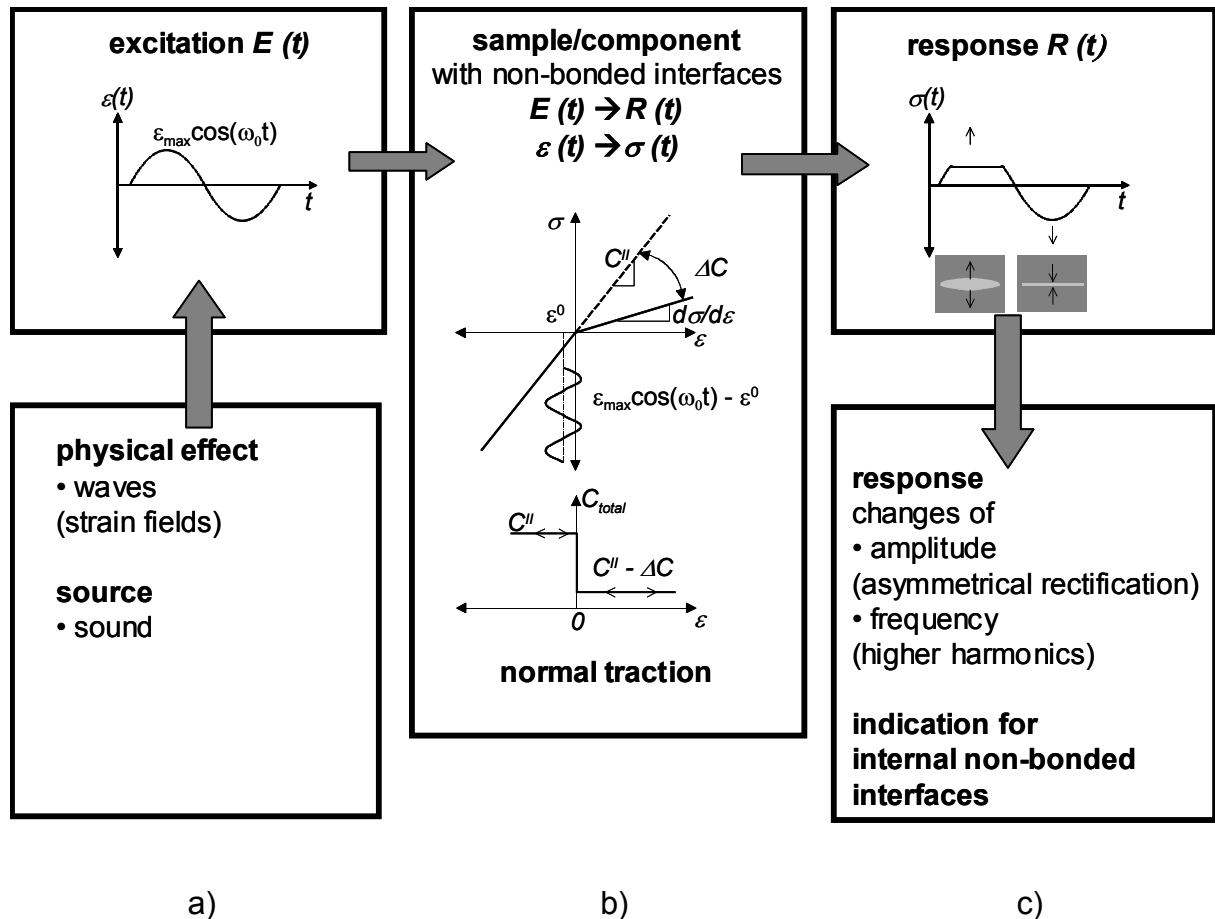


Figure 16: Local non-linear behaviour of non-bonded interface driven by normal traction; a) driving signal $E(t) = \varepsilon(t)$; b) stress–strain relation of a non-bonded interface and contact stiffness as a function of strain (bottom); c) asymmetrical rectification of the response $R(t) = \sigma(t)$ and generation of higher harmonics because of “clapping”.

Because of the local disbonding, compressive stress can be transferred more easily than tensile stress (Figure 16 c middle). This effect leads to an asymmetrical rectifica-

tion of the stress field that depends on the motion of the boundary (Figure 16 c top). The asymmetrical contact stiffness C_{total} depending on strain (and on time) (Figure 16 b bottom) consists of the stiffness C^H and the dynamic stiffness ΔC . According to Figure 16 b, the dynamic stiffness equals [86]

$$\Delta C = C^H - \left(\frac{d\sigma}{d\varepsilon} \right)_{\varepsilon > 0}. \quad (3-18)$$

For the time varying excitation (3-17) and the contact static strain ε^0 of a non-bonded interface, the change of stiffness with time is:

$$\Delta C(t) = \frac{\Delta C}{C^H} H(\varepsilon_{\max} \cos \omega_0 t - \varepsilon^0) \quad (3-19)$$

and represents with the Heaviside unit step function $H(\varepsilon)$, a pulse modulation type function with a period of $T = 2\pi/\omega_0$. Because the stress σ is a linear function for both $\varepsilon < 0$ and $\varepsilon > 0$, one obtains for the output stress

$$\sigma = \{C^H + \Delta C(t)\} \{\varepsilon(t) - \varepsilon^0\} \quad (3-20)$$

This stress-strain relation of a non-bonded interface driven by normal traction is shown in Figure 16 c. Because of the asymmetrical stiffness, only one part of the strain response is rectified. The frequency spectrum of equation (3-20) can be calculated by using the modulation theorem. The amplitude of the n -th harmonic ($n \in \mathbb{N}_0$) is:

$$a_n = \varepsilon_{\max} \Delta C \Delta \tau \{ \text{sinc}[(n+1)\Delta \tau] - 2 \cos[\pi \Delta \tau] \text{sinc}[n\Delta \tau] + \text{sinc}[(n-1)\Delta \tau] \}. \quad (3-21)$$

In this formula, $\Delta \tau = \tau/T$ represents the modulation pulse length with $\tau = (T/\pi) \arccos(\varepsilon^0/\varepsilon_{\max})$. The arccos-function does not exist for $\varepsilon_{\max} < \varepsilon^0$. Thus, the excitation must be greater than the static contact stiffness and therefore pass the threshold for which $\varepsilon_{\max} > \varepsilon^0$ (CAN threshold). As a result, ‘‘clapping’’ defects (like clapping of old cars) is accompanied by occurrence of higher harmonics in the frequency spectrum.

3.2.2 Tangential traction driven interfaces

In addition to normal traction, non-bonded interfaces can also be driven by tangential forces if the defect interface is perpendicular or has a certain angle to the propagating longitudinal wave (Figure 17). Because of periodic tangential movement of two boundaries with respect to each other and the hysteretic stress-strain relation (Figure 17 c), energy losses due to friction occur. According to Figure 17 b the contact stiffness C changes twice between C_s (sticking) and becomes zero for sliding.

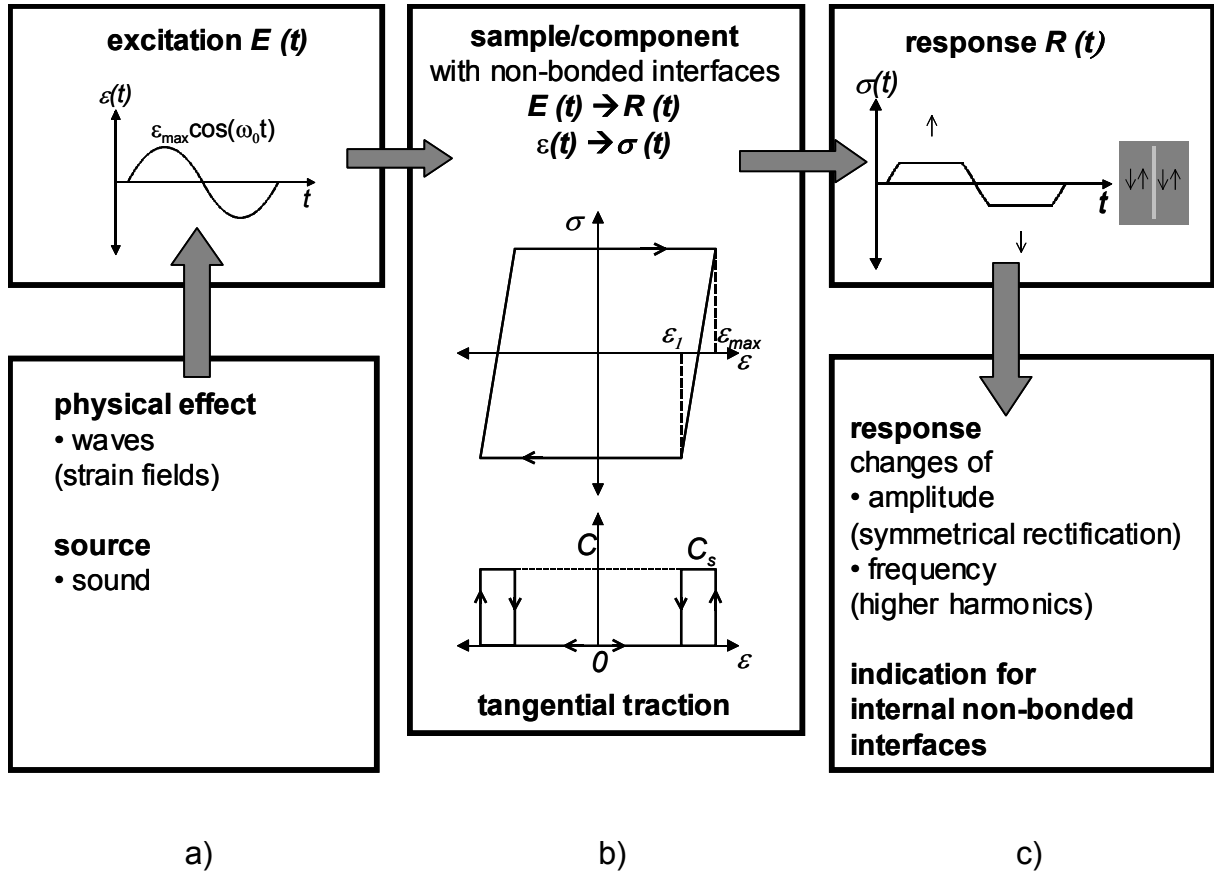


Figure 17: Local non-linear behaviour of non-bonded interface driven by tangential traction; a) driving signal $E(t) = \varepsilon(t)$; b) idealized stress-strain relation of a non-bonded interface to describe the distortion of the signal; stiffness constant C changes between C_s (sticking) and zero (sliding); c) symmetrical rectification of the response $R(t) = \sigma(t)$ and generation of higher harmonics.

The local stiffness of friction-coupled interfaces of non-bonded contacts depends on time and is expressed by [87]

$$C(t) = \frac{C_s}{2} \left\{ 1 - \text{sign} \left(\dot{\varepsilon} \right) \text{sign} \left[\varepsilon + \text{sign} \left(\dot{\varepsilon} \right) \varepsilon_1 \right] \right\}. \quad (3-22)$$

After integrating this relation on strain we obtain

$$\sigma(t) = C(t)\varepsilon(t) + \text{sign} \left(\dot{\varepsilon} \right) \cdot \left[C(t)\varepsilon_1 + \frac{1}{2} C_s (\varepsilon_{\max} - \varepsilon_1) \right] \quad (3-23)$$

which is a double-valued linear function of strain ε with the integration constant σ in accordance with Figure 17 c. The non-linear response of tangential driven interfaces because of friction is a symmetrical rectification of the output stresses. The amplitudes of the higher harmonics in the frequency spectrum found by a Fourier transformation of (3-23) are [87]:

$$\begin{aligned}
b_N = C_s \varepsilon_{\max} \left\langle \Delta \tau_f \left\{ \text{sinc}[(N-1)\Delta \tau_f] + \text{sinc}[(N+1)\Delta \tau_f] - 2\Delta \varepsilon \cdot \text{sinc}[N\Delta \tau_f] \right\} \right\rangle - \\
- C_s \varepsilon_{\max} \left(\frac{1}{2}(1-\Delta \varepsilon) \cdot \left| \text{sinc} \left[\frac{N}{2} \right] \right| \right)
\end{aligned} \tag{3-24}$$

for $N = 2n+1$; $n \in \mathbb{N}_0$, where $\Delta \varepsilon = \varepsilon_1 / \varepsilon_{\max}$, and $\Delta \tau_f = (1/2\pi) \arccos(\varepsilon_1 / \varepsilon_{\max})$. Again the *arccos*-function does not exist for $\varepsilon_{\max} < \varepsilon_1$. As a result, the maximum amplitude of a driving signal must pass the threshold of ε_1 above which higher harmonics are generated. According to (3-24), this mechanism is a source for odd higher harmonics only.

The two mechanisms above show that higher harmonics are generated at localized imperfections with non-bonded interfaces if a certain threshold is passed and if the gap between two boundaries is not so large that the two boundaries can interact with each other. These conditions are fulfilled at least at the edges of e.g. cracks. The efficiency of generation of higher harmonics is many orders of magnitude higher than in classical non-linearity. This effect can be successfully used not only for defect-selective detection but also for localizing and defect-selective imaging of potential defects.

4 Basic Ultrasound Testing Techniques

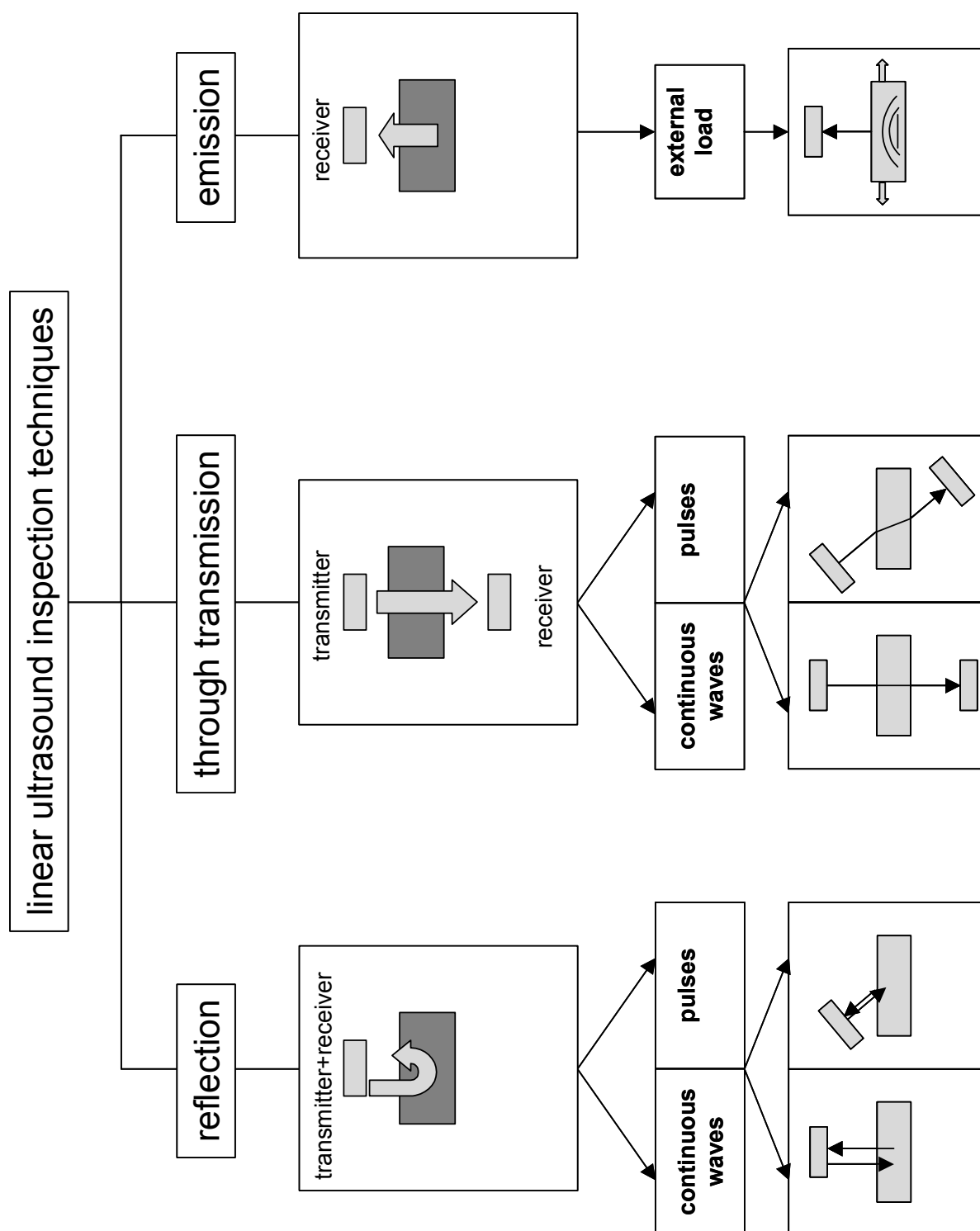


Figure 18: Linear ultrasound inspection techniques.

Common non-destructive inspections using ultrasound need an acoustic couplant in (section 4.1) and are performed primarily in two ways.

An ultrasound wave is directed into a sample and

- either the reflected wave (section 4.2; reflection technique; reflections from all kinds of surfaces or grain boundaries) is recorded, or
- the through-transmitted wave (section 4.3; through-transmission technique) is recorded.

Both techniques (Figure 18) work either with continuous wave or with pulses. Another method is based on the acoustic emission of samples (Figure 18). Acoustic emission occurs mostly when load is put on samples [88,89,90,91]. Depending on the information one wants to obtain from the ultrasound signals received, the signals can be displayed in several ways (section 4.4).

4.1 Coupling media and coupling techniques

Ultrasound inspection cannot function without a couplant, which is needed to transfer the acoustic energy between the transducer and the sample. The coupling medium should meet the following conditions:

- Constant coupling during entire inspection for reliable testing.
- Suitable acoustic matching for acoustic energy transfer (acoustic impedance of the couplant is between that of the sample and of the probe face).
- No influence on the properties of the testing object.
- Not toxic or corrosive.
- Wets both the surface of the transducer and of the sample (suitable viscosity).
- Without air-bubbles or solid inclusions.
- Can easily be removed after inspection.

Coupling is performed in two ways, direct contact coupling and gap testing technique [92] (also called delay path/delay line coupling [70]). The two techniques differ primarily in the length of the coupling medium path between sample and probe.

Contact coupling is done by pressing the transducer onto the sample surface using constant force. It can also be done by merely gluing the transducer to the sample with hot-melt glue, with resin, or with wax. After inspection, though, it is often difficult to re-

move the transducer from the sample. Dry-coupling, an additional technique, uses transducer shoes like pads or hemispheres made out of soft rubber. This method is used for inspection of materials such as wood because soft rubber materials fit rough surfaces [93]. Another technique uses roller probes with plastic tyres (dry-contact wheel transducer) [94,95]. The advantage of dry-coupling is that remote testing is possible. The limitation is the difficulty of keeping coupling conditions constant.

Liquid or semi-liquid media and paste are also candidates for contact coupling. Examples are gelatine, gel, grease, heavy oil, glycerine, or resins. Each has its own advantages and disadvantages, but all have in common that scanning across the sample is difficult to perform.

Gap testing techniques use a delay line between the transducer and the receiver. The line consists either of a solid medium (e.g. thermoplastic material) or a fluid medium (immersion coupling). Immersion coupling is widely used in industry. The sample is immersed into liquid and the transducer is mounted a certain distance away from the sample depending on focal length. Because the liquid medium fills the gap, uniform coupling conditions are possible. Therefore, scanning across the test object is feasible. Water is the most common liquid for inspection using this technique. It is inexpensive, available almost everywhere, and is not toxic. As mentioned in section 2.4, the sound amplitude is reduced to only about 13 % between transmitting and receiving (losses inside the sample are not taken into account). Measurements are performed primarily in a water bath which restricts this method because it is difficult to move the tank and large components are difficult to inspect. The lack of portability is overcome by using a water jet device (the squirter technique) with which ultrasound waves are coupled into the sample. The limitation of this technique is that air-bubbles inside the water jet or on the surface of the test object can cause disturbing reflections. The disadvantages of all immersion techniques are that immersion is not a real remote technique and that the liquid couplant can penetrate into samples and cause corrosion or change the properties of materials. Also, liquid-sensitive materials cannot be inspected.

Therefore, there is a need for real non-contact, remote ultrasound inspection. Developments are being made for non-contact coupling, for example with the use of electric or/and magnetic fields or with laser beams. The most promising technique is laser-based ultrasound that generates an ultrasound pulse caused by heat shock [96,97,98].

Ultrasound inspection through air, though, would be the most appropriate method. Because of the huge impedance mismatch between solid and air, however, it is difficult to perform (section 2.4 and chapter 5).

4.2 Reflection technique

The reflection technique, especially with pulses (pulse-echo method), is the most commonly used in industry. A single ultrasound probe both transmits and receives signals so that only single-sided access is needed. A pulse generator provides a signal to the transmitter which itself generates an acoustic wave. The wave propagates from the transducer to the sample and into it. On its path, it crosses several boundaries with different acoustic impedances which are reflecting the wave partly according to equation (2-61). The wave is first reflected at the front surface of the sample (entry echo [92] or front surface reflection [70]). At internal surfaces (acoustical boundaries) of inclusions, the wave is reflected again (discontinuity echo [92] or inclusion reflection [70]). The last reflection (back-wall echo [92] or back surface reflection [70]) takes place at the boundary of the test object (solid) and the surrounding medium (e.g. water or air). An example (amplitude versus time) is given in Figure 19.

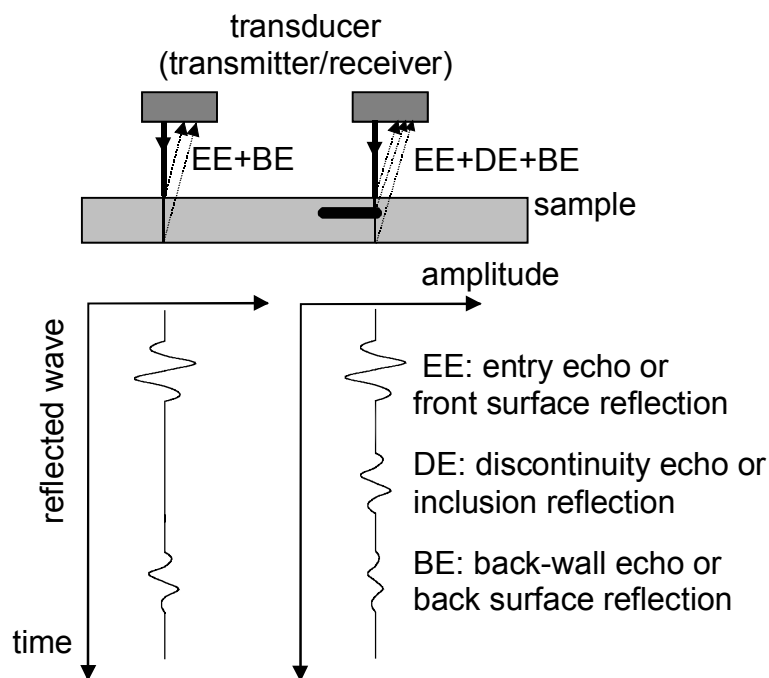


Figure 19: Reflected wave without inclusion (left) and with “sound soft” inclusion (right).

The sample is surrounded by water (lower impedance than the sample) and has an inside inclusion with lower impedance than the material. The amplitude recorded over time at an inclusion-free part of the test object shows only entry and back-wall echo, while at an inclusion, a discontinuity echo can be seen also. By measuring the ultrasound signal's time of arrival, it is possible to calculate the depth of an inclusion. This ability to measure depth is another advantage of this technique. Frequent applications of the reflection technique are detection of defects or damage in metal plates [99], railroad tracks [100], and fibre reinforced polymer materials [101]. The angle of incidence does not necessarily need to be perpendicular to the sample surface (Figure 18). With angle probes, for instance, it is possible to inspect welding more readily because it is easier to place a transducer next to the welding instead of on the uneven surface [93]. Misfits of fibre orientation inside of long fibre-reinforced materials can also be detected by scanning across a sample with a transducer that is not mounted perpendicularly to the surface of a sample [102]. By orbital scanning, fibre orientations can also be distinguished [103]. These techniques detect the ultrasound waves backscattered by fibres.

4.3 Through-transmission technique

A single-sided measurement has its limitations if highly sound-absorbent materials such as porous materials or components with many boundaries (e.g. honeycomb structures) need to be inspected. Because the ultrasound beam must pass through the sample twice (round trip), the signal-to-noise ratio may be too poor. In this case, the through-transmission technique offers better possibilities because the wave needs only to pass through the material once. With this method, the transmitted wave, but not the reflected signals are recorded. As a result, the received ultrasound signal in the through-transmission technique looks different from that in reflection-technique measurements. Only pulses or continuous waves, but not reflections, are mapped in the through-transmission technique. As a consequence, information about the depth of discontinuities is lost. By measuring in through-transmission, however, the x - and y -positions and the dimensions of a discontinuity can be distinguished. For detection of potential defects, changes of amplitude are evaluated (Figure 20). These changes of amplitude occur because the ultrasound wave is reflected, scattered or obscured by imperfections. As shown in Figure 20, a sample is placed between two separate transducers in which one acts as transmitter and the other one as receiver. For maximum

transferred acoustic wave energy, both transducers must be precisely aligned and must have the same characteristics (acoustic and electric impedance, centre frequency, bandwidth).

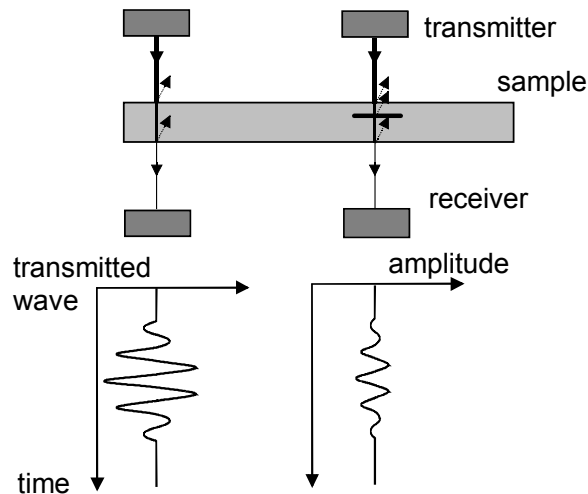


Figure 20: Transmitted wave (through-transmission technique) without inclusion (left) and with inclusion (right).

The immersed through-transmission technique can be used for such measurements as monitoring of disbonding that occurs between metal and rubber layers of engine mountings [93]. Again the angle of incidence does not need to be 90° ; for example, the inspection of fillet welds is performed with two angle probes [93]. Also with incident waves, it is possible to measure elastic constants [104].

Both reflection and through-transmission technique can also be used to perform non-linear measurements. The difference is that transmitter and receiver differ in the centre frequency. The centre frequency of the receiver is n -times of the transmitter to receive the n^{th} order higher harmonic.

4.4 Scanning techniques and imaging of ultrasound signals

For defect detection and characterisation, several types of ultrasound signal presentations (images) are common. The choice depends on both the features of the equipment and on the information one wants to obtain from the data.

The A-scan presentation (or A-scan image) $A(x_0, y_0, t)$ displays amplitude A at a single point (x_0, y_0) at time t and therefore provides information about the depth of discontinui-

ties (if measured in reflection technique). This kind of presentation (Figure 19 and Figure 20) is easy to perform and is the most commonly used one in ultrasound testing. It is difficult to evaluate the run of signals measured in reflection technique if there are several boundaries or potential defects inside the test object and if there is no reference run of the signals recorded at a known defect-free area. The A-scan presentation is primarily used for contact coupling measurements and has its limitations in inspection of large components because numerous single-point A-scans would have to be performed. For larger samples, and to obtain two-dimensional information about a defect, a B-scan presentation is more suitable.

The B-scan presentation $A(x, y_0, t)$ is performed by scanning across the sample and mapping several A-scans along one coordinate x while the y -axis is fixed. On the B-scan image, the abscissa represents the position along the scanning direction and the values of time of flight or distance are shown on the ordinate. With the help of a colour bar scheme, the signal amplitude height is displayed. A measurement in reflection technique leads to a B-scan image shown in Figure 21 a.

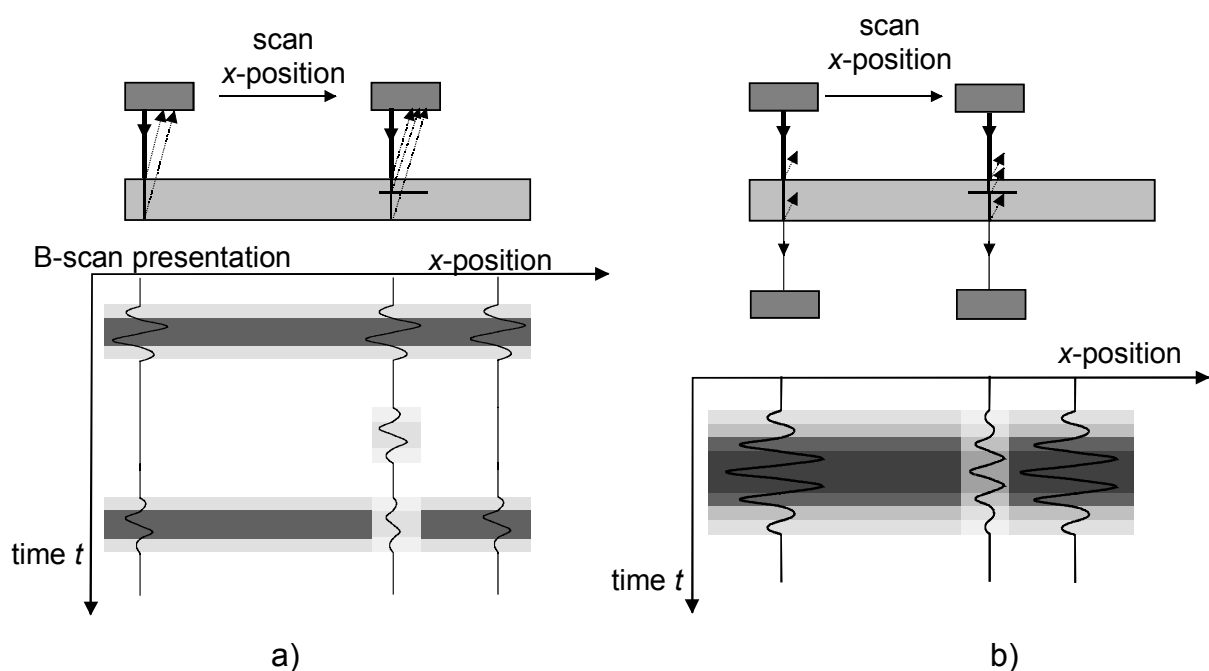


Figure 21: a) B-scan presentation of a measurement performed in reflection technique; b) B-scan presentation of a measurement performed in through-transmission technique.

The entry echo and the back-wall echo are indicated through parallel lines of different colours. The discontinuity echo can be seen between both echoes. Because of the imperfection, the back-wall echo at the x -position of the potential defect is weaker. This

type of image shows a cross-section of the sample perpendicular to the surface and parallel to scanning direction. As a result, the B-scan image displays the x-position, the length in x-direction, and the depth of a potential defect. By contrast, on the B-scan presentation of a through-transmission examination, only parallel lines of different amplitude heights and weaker signals across a discontinuity are shown. Thus, on the B-scan image only the x-position and the length in x-direction of an imperfection but not its depth can be detected.

The C-scan presentation $A(x, y, t_n)$ is another standard method that is becoming more and more popular because ultrasound equipment is getting increasingly better due to advances in microprocessor technology. The C-scan image shows a view of the sample as seen from above and therefore shows a cross section of the sample and the imperfection parallel to the scanning surface [92]. Thus it is a projection of internal features regardless of their depth [92]. To achieve such images, the sample is scanned in a raster pattern and either the reflected wave amplitude or the transmitted wave amplitude at a certain time range t_n (or the entire A-scan) and the x-, y- coordinates are mapped. To evaluate a C-scan image, the amplitudes are integrated within a time range and the result is displayed with the help of a colour bar scheme. Information about the size and the position of a potential defect are available because of changes in amplitude. On Figure 22, the performing of a C-scan presentation of a through-transmission measurement is shown.

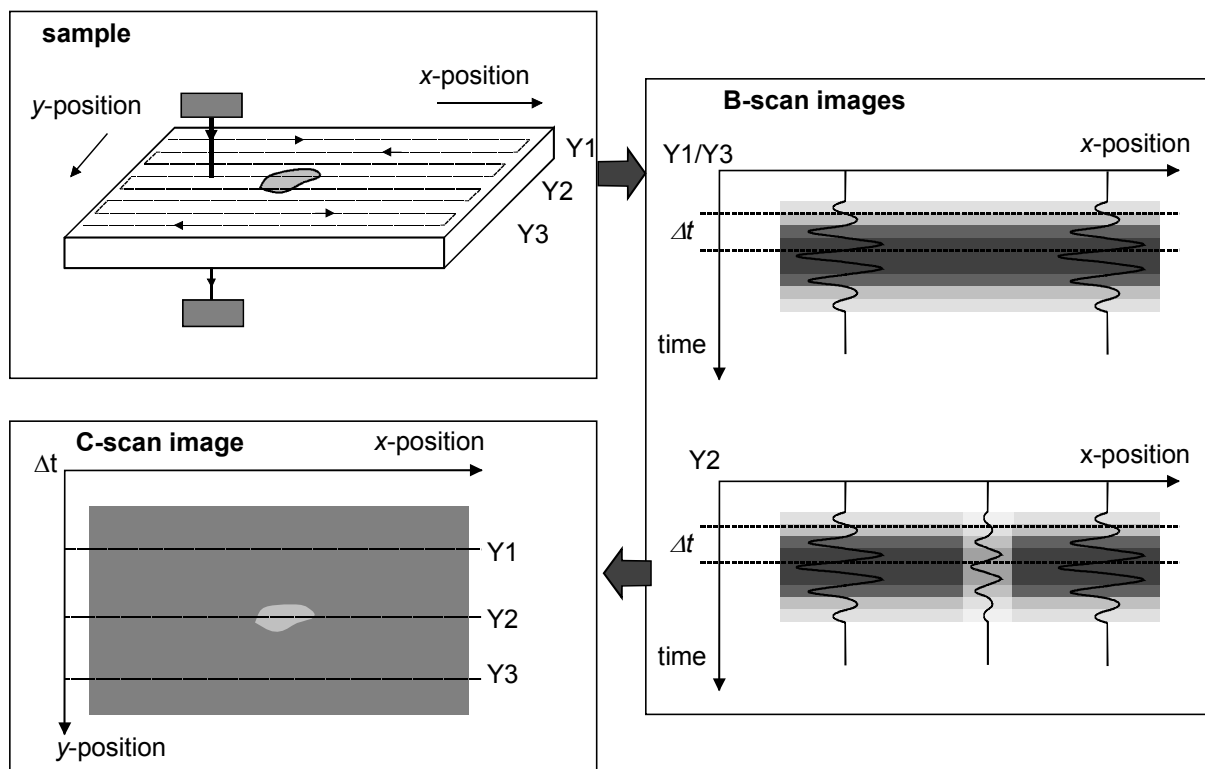


Figure 22: Performing a C-scan image, the entire sample is scanned (upper left, in this case in through-transmission technique) and either entire B-scans (right) or the amplitude are mapped within a time range. The change of amplitude within a time range Δt is displayed in a C-scan image (lower left).

The D-scan presentation $t(x, y)$ is a modified C-scan presentation and shows the time of flight t dependence as a function of position (x, y) . The image displays a cross section of the test object perpendicular to the projection of the beam axis on the scanning surface.

The F-scan presentation $F(x, y)$ is also a modified C-scan presentation. Instead of amplitude, another feature - such as centre-frequency, phase angle, or frequency spectra - is displayed as a function of position (x, y) .

In Table 7 and Table 8, the different types of ultrasound presentation techniques explained above and also other types of images are summarized. The descriptions were taken from the European Standard EN 1330-4 which defines the terms used in ultrasound testing [92] and were edited to describe some techniques more clearly and to add techniques that are not explained in the standard.

type of image	spatial coordinates			signal amplitude	time of flight	other features	type of data acquisition
	x	y	β	A	t	F	
A-scan presentation				•	•		$A(x_0, y_0, t)$
B-scan presentation	•			•	•		$A(x_0, y, t)$
Rotation B-scan presentation			•	•	•		$A(\beta, x_0, y_0, t)$
Polar scan presentation			•	•			$A_{max}(\beta, x_0, y_0)$
C-scan presentation	•	•		•			$A(x, y, t_n)$
Volume scan presentation	•	•		•	•		$A(x, y, t)$
P-scan presentation	•	•		•	•		$A_m(x_m, y_0, t),$ $A_m(x_0, y_m, t),$ $A(x, y, t_n)$
D-scan presentation	•	•			•		$t(x, y)$
F-scan presentation	•	•				•	$F(x, y)$

Table 7: Different types of ultrasound imaging methods.

type of image	description
A-scan presentation	Display of the ultrasound signal in which the abscissa represents the time, and the ordinate represents the amplitude
B-scan presentation	Image showing a cross section of the test object perpendicular to the scanned surface and parallel to a reference direction. The cross section will normally be the plane through which the individual A-scans have been collected.
Rotation B-scan presentation	Modified B-scan: amplitude is recorded versus rotation angle and time (orbital scanning)
Polar scan presentation	Modified B-scan: maximum amplitude is recorded versus rotation angle (orbital scanning)
C-scan presentation	Image of the results of an ultrasound examination showing a cross section of the test object parallel to the scanning surface.
Volume scan presentation	Three-dimensional (spatial) representation of the inspected volume. At each inspection-point of scanning surface, a complete A-scan must be recorded.
P-scan presentation	Projection-view of several B- or C-scans
D-scan presentation	Image of the results of an ultrasound examination showing a cross section of the test object perpendicular to the projection of the beam axis on the scanning surface. The D-scan will normally be perpendicular to the B-scan.
F-scan presentation	Modified C-scan: values of a certain feature (e.g. centre-frequency or phase angle) are recorded and displayed instead of amplitudes.

Table 8: Descriptions of different ultrasound imaging methods.

5 Air-coupled ultrasound inspection method

As mentioned in section 2.4, it is difficult to measure through air using ultrasound. Therefore, some additional factors must be considered to develop or to use an ACU testing device.

5.1 Fundamental considerations

The objective of all improvements to ultrasound test equipment is to enhance the signal-to-noise ratio (S/N) which can be estimated by [105]

$$S/N = 10 \log \left(\frac{Pa}{4kT\Delta f \cdot NF} \cdot \frac{T_I}{CL \cdot AL \cdot AB \cdot DL \cdot EL} \right) \quad (5-1)$$

Pa	available transmitter power	T_I	transmission coefficient
k	Boltzmann's constant	CL	two-way transducer conversion loss
T	absolute temperature in °K	AL, AB	sound absorption in air and of the sample
Δf	effective bandwidth of the receiver electronics	DL	diffraction losses in air
NF	"noise factor" (range 1-10)	EL	"excess" propagation losses

The transmitter power (Pa), is represented by [105]

$$Pa = V^2 / 4R \quad (5-2)$$

and must be enhanced by choosing a high peak-to-peak voltage (V) and a low output loading resistance of the signal generator or amplifier (R). This situation also requires the use of very efficient electrical impedance and noise matching networks at the transmitting and receiving sides of the equipment. At the same time, the effective bandwidth of the receiver (Δf) as well as the "noise factor" (NF) must be reduced. The noise factor NF is primarily a scale for the efficiency of how well the electrical input resistance of the receiving transducer matches the resistance value that corresponds to the noise resistance of the signal generator or preamplifier. With an electrical impedance-matching transformer, the noise factor can be reduced.

The second part of equation (5-1) explains the ratio of different losses. The transmission coefficient is given by equation (2-65) in which Z_1 is the specific acoustic impedance of air and Z_2 is the specific acoustic impedance of the test object. The value of T_I is therefore fixed for a specific task and can not be influenced.

In the denominator of equation (5-1), the two-way conversion loss (CL) of the transducers for the interface solid (transducer material) and air can also be calculated by equation (2-65). It is evident that CL must be decreased by the transducer design, e.g. by better impedance matching. The sound absorption losses in air (AL) are between 10 and 100 dB/m in the frequency range of 100 kHz to 1 MHz. In practice, with a distance between the transmitter and the receiver of 80 – 100 mm, the losses do not exceed 10 dB (at 300° K and atmospheric pressure) [105,106,107,108] (see also section 2.7). The absorption loss of the sample (AB) depends on the material and is therefore fixed. Finally, diffraction losses (DL) and “excess” propagation losses (EL ; amplitude saturation effects, partial loss of phase-front coherence, and air turbulence effects) can be ignored because both factors have an insignificant impact. In summary, ACU inspection is possible if the impedance mismatch between transducer and air as well as the electrical impedances are reduced, and the power output is enhanced.

5.2 Air-coupled ultrasound device

The considerations described in section 5.1 are taken into account in the design and development of commercially available ultrasound testing equipment [109,110,111]. A commercial device “AirTech 4000” [111] was used for the measurements described below. The device consists out of two probes for transmitting and for receiving ultrasound signals. These two transducers are controlled by personal computer boards that are built into an industrial computer case.

5.2.1 Transmitting part of the equipment

The ultrasound signals are transmitted by probes adapted for measurements in air. The first studies in the development of air-coupled transducers were made as early as 1954 [112]. In the past 15 years, major developments have been made in the design. Two types of transducer offer the best possibilities to work in air.

First are electrostatic (capacitance) probes [113,114]. They consist out of a thin polymer membrane (coated on one side with a thin metallic layer) and a backplate made, for example, out of metal-coated silicon with etched pits [115]. Both parts form the two plates of the capacitor.

Second are the probes made out of piezo-composites [116] which are used in the “AirTech 4000” equipment. Piezoelectric rods (“active phase”) aligned in parallel along the thickness direction are embedded in a three-dimensional passive polymer matrix (“1-3-configuration”, Figure 23, left) [117,118]. The middle-to-middle distance a between the two rods must be smaller than the half-wave length of the shear wave ($a \leq \lambda_s/2$) of the polymer matrix in order for the composite as a whole to vibrate. (Figure 23, right).

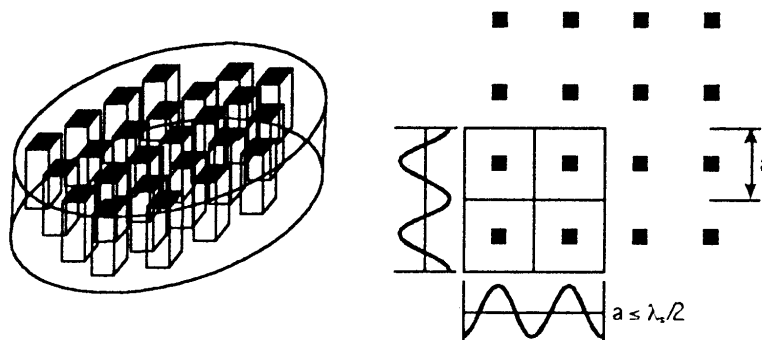


Figure 23: Drawings of a 1-3 piezo composite [117].

The piezo composites are manufactured according to the “dice and fill” technique [119] in which a piezo ceramic plate is diced into an orthogonal array. It is first sawed in cuts parallel to each other, and again sawed after a 90°-rotation of the plate. The depth of the cuts is about 80% of the ceramic thickness. Then the notches are filled with a polymer material, followed by a heat treatment of several hours. Next, both sides are covered with electrodes such as a sputtering Ni-alloy base and galvanization of a gold-layer [117]. Afterwards, the transducers are focused by forming the composite into a spherical shape. The focal length of the transducers used is 40 mm (Figure 24 a) and is much smaller than the distance at which the amplitude is reduced to $1/e$ (Table 6). The calculated radius of focal spot for the transducers is 3 mm (equation (2-98); $c = 330$ m/s, $f = 450$ kHz, $f_f = 0.04$ m, $a = 0.0095$ m). Using this kind of piezo-composite transducers, the acoustic matching to air is four times better than with plain piezo ceramic because the integral impedance Z is reduced by the passive polymer phase with lower velocity and lower density than the piezo ceramic itself (piezo composites: typically $Z = 6\text{-}10 \cdot 10^6$ kg/m²s; piezo ceramic: typically $Z = 29\text{-}35 \cdot 10^6$ kg/m²s). In addition, with a matching layer of silicon rubber containing air bubbles (section 2.6), the efficiency is improved 5 to 30 times. The rear side of the composite is air-backed in order to drive the piezo composite in thickness mode resonance (Figure 24 a). As a conse-

quence, the transducers operate with a much higher sensitivity. The piezo composite is built in a metal casing in order to prevent it from becoming damaged and to shield it from electrical interferences (Figure 24 b).

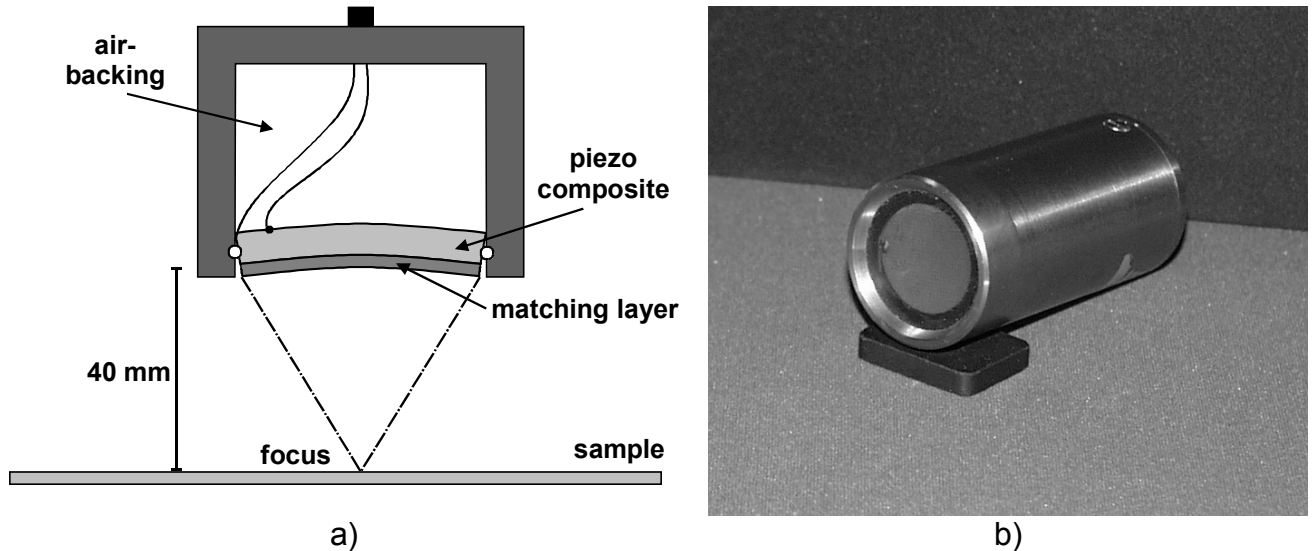


Figure 24: Drawing (a) and image (b) of ACU probe.

The transmitter probe has a built-in electrical impedance matching network (coil and transformer) in order to increase the transmitter voltage by six times and therefore increase the output power. The transmitter probe is operated by a software-controlled burst transmitter board that was especially developed for the air-coupled equipment. A built-in power amplifier generates an output power of up to 1.2 kW into 25 Ω . Because of low output electric impedance ($< 1.8 \Omega$) and matching networks, the voltage at the piezo composite reaches up to 1400 V_{pp}. The board generates quartz-controlled tone burst signals up to 15 cycles and is adjustable for frequencies between 70 kHz and 1 MHz (pulse width and period) with a pulse repetition rate of up to 2 kHz (Figure 25 a). In our case, the transmitter is driven by 15 cycles with a pulse width of 1.125 μs and a period of 2.250 μs (444 kHz) to match the resonance frequency of 450 kHz (wave length in air: 0.76 mm) of the piezo composite. Therefore an adjustment range of $\pm 10\%$ is necessary [120]. By using the rectangular tone burst pulse instead of a spike pulse, additional power is provided during the transient phenomenon of the transducer (Figure 25 a) to achieve high oscillation amplitudes of the piezo-composite plate. The tone burst with 15 cycles is shown in Figure 25 b.

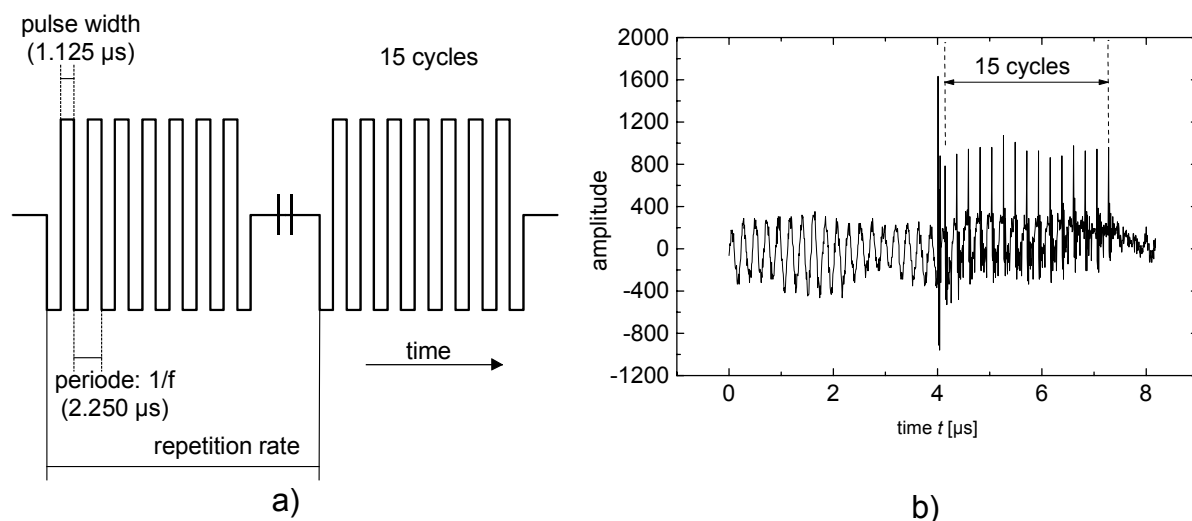


Figure 25: a) Electrical input to the transmitter, b) output of the receiver.

5.2.2 Receiving part of the equipment

The receiver probe also contains an electrical impedance matching network and additionally a very low noise preamplifier (50 dB) as well as a narrow-band filter unit (Figure 26). The combination of preamplifier and narrow band-pass filter unit allows low-noise amplification. As a result, no additional averaging of the signals is needed and fast scanning across a sample is possible.

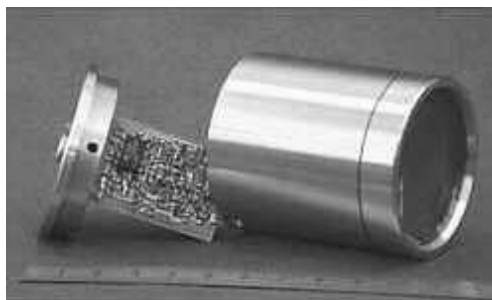


Figure 26: Image of the ACU receiver probe [121].

Because of the long burst signal, the air-backed piezo composite, and the built-in electronics, measurements are possible only with two separate ultrasound probes (transmitter and receiver) either in through-transmission mode or with transmitter and receiver on the same side.

An adapter board receives the ultrasound signals and provides voltage for the preamplifier and band pass filter unit. Afterwards, the signal processing and additional amplification is done by an ultrasound receiver board originally designed and used for

measuring in immersion technique. The analogue signals are then sampled with a maximum of 200 MHz and a resolution of 8 bits by an analogue-to-digital (A/D) converter board ("PAD 82", made by Spectrum Systementwicklung). The tone burst signal, described above, generates a long ultrasound signal of about 100 μs duration (Figure 27 a).

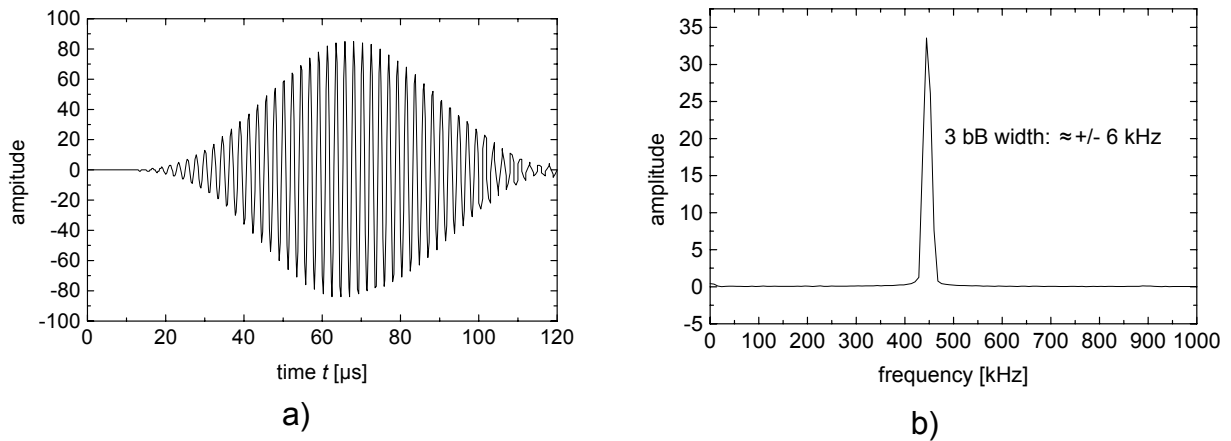


Figure 27: a) Received ultrasound signal, b) frequency spectrum of the received ultrasound signal.

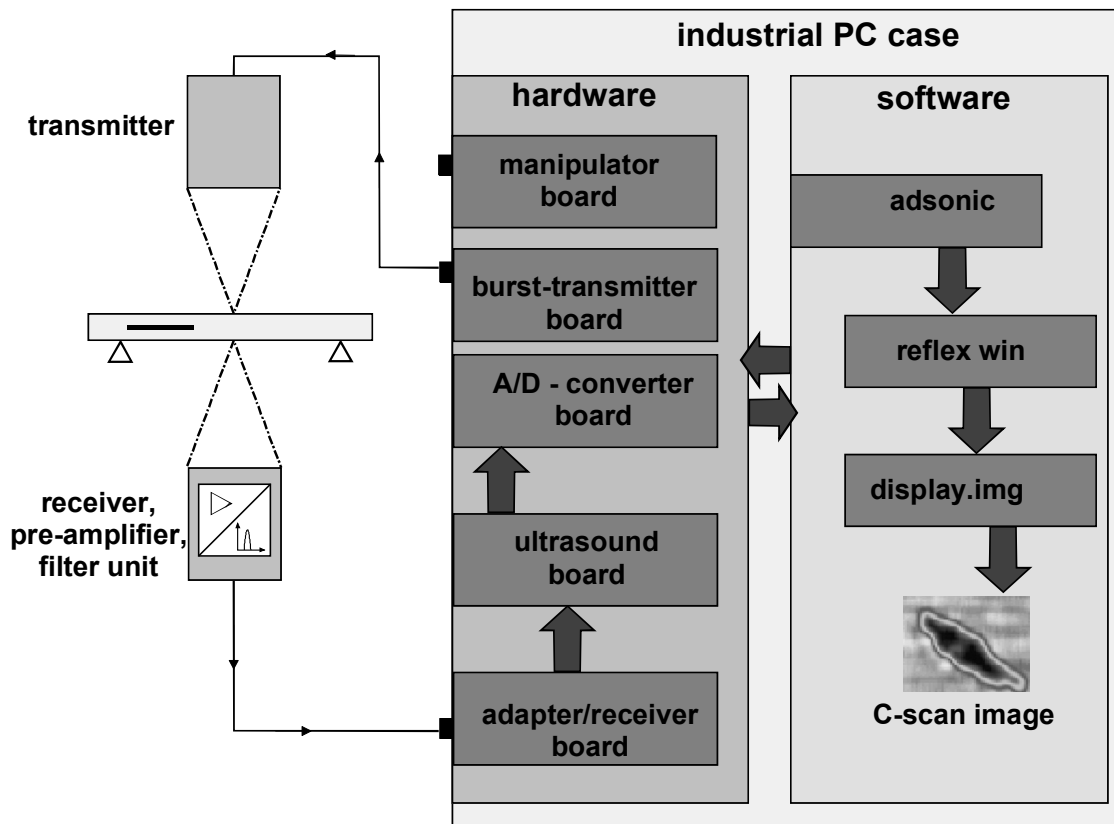


Figure 28: Block diagram of the system architecture of the air-coupled equipment.

The calculated frequency spectrum of this ultrasound signal is displayed in Figure 27 b. The run of the curve shows the narrow band characteristic (3 dB width: $\approx \pm 6$ kHz) of the ultrasound signal. The entire system architecture is presented in Figure 28.

5.3 Performing measurements with linear ACU inspection

This section describes how a measurement in through-transmission mode is performed with the air-coupled equipment and what considerations need to be taken into account. Linear ACU measurements record changes in amplitude because of reflections, absorption, and differences in damping (changes in density or elastic properties). For inspection, a sample is placed on top of the edges of two mountings and between transducer and receiver (distance between probe and sample: 40 mm). The scanning across a sample is done by a three-axis, stepping motor-controlled scanning assembly (made by ISEL, (Figure 29)) with a maximum speed of 25 mm/s and a precision of 0.01 mm. This scanning assembly is operated by a manipulator PC-board. For all measurements, the A-scan spacing was 0.5 mm (x-position) and a 1 mm or 2 mm spacing between two B-scans (y-position) was chosen.

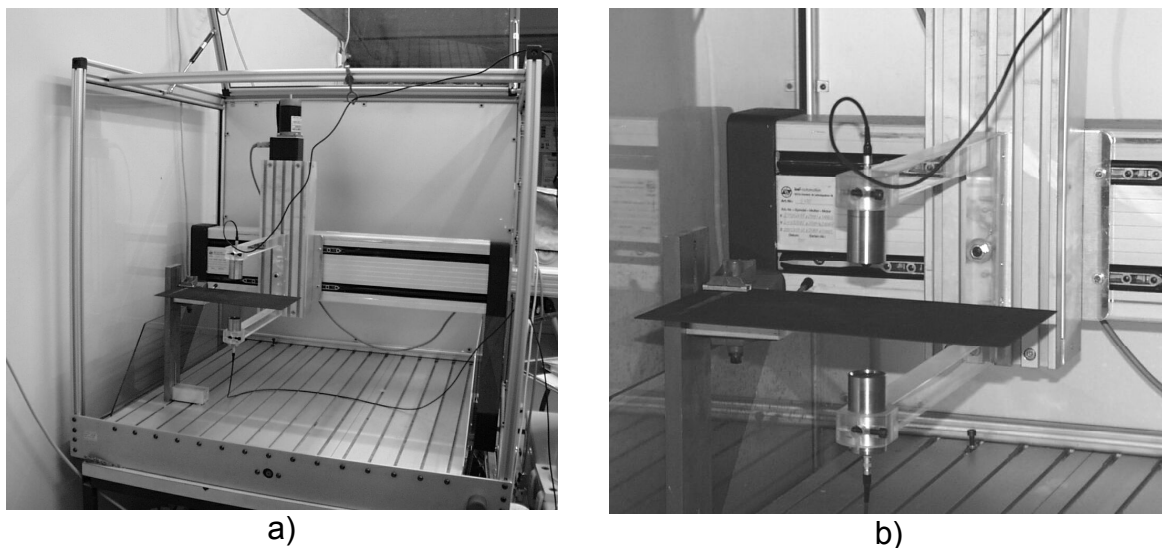


Figure 29: a) ACU inspection set-up; b) transducers and CFRP-sample.

The hardware and the scanning system are controlled by the software module “ADSONIC” which was especially designed for this equipment [122] (Figure 28). This software calculates B-scan images and stores the raw data for further processing. With “ADSONIC”, the dimension of the scanned area (x-, y-dimension and the spacing), the sampling rate (mostly 12.5 MHz), and the gain are set. The change of amplitude (or the gain) is described by (see also section 2.4)

$$\Delta A = 20 \log \frac{A_2}{A_1} \text{ [dB]} \quad (5-3)$$

in which ΔA is the gain [dB], A_2 the amplitude, and A_1 the reference amplitude. To examine the dependence of amplitude from gain, a pseudo ACU C-scan image was performed. Across a sample (PMMA, thickness: 4.3 mm), ACU B-scans were made along the same scanning path without actually moving in y -direction but with increasing y -direction in the software setting. The ACU B-Scans are performed with different gains that vary between 30 dB and 70 dB with a step of 5 dB. Out of these data, a C-scan presentation within a time range of 0.01 ms (typical value for calculating of a C-Scan in this work; see also below) was evaluated. Along a line in “ y -direction”, with different gains, the echo dynamic values were taken and used for the diagram in Figure 30. The values were normalized with the amplitude at 30 dB, A_2 ; see (5-3). The half logarithmic linear behaviour of amplitude between 5 dB and 30 dB (35 dB – 60 dB) can be shown. The deviation at 40 dB (70 dB) is caused by an overrange of the ultrasound signals.

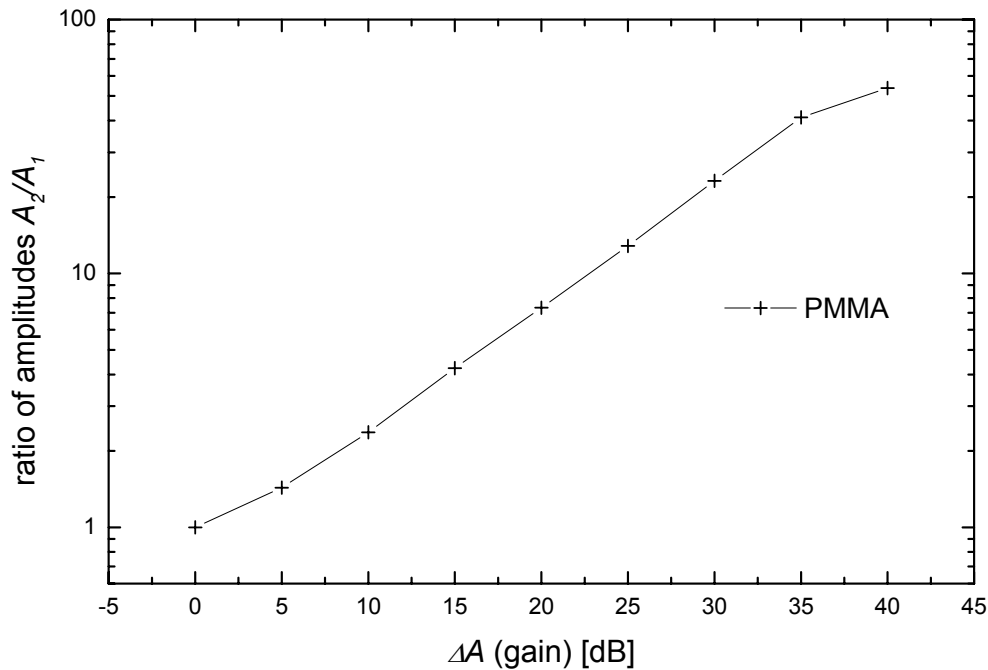


Figure 30: Amplitude versus gain steps (Δ gain) of 5 dB, measured at a PMMA-sample (thickness: 4.3 mm).

For performing C-scan images and signal analysis, the software module “REFLEXWIN” [123] is used. It is based on Windows® platform and was developed for geophysical applications. It was chosen because it offers more features than standard ultrasound calculation software. For evaluating a C-Scan image in through-transmission, it does

not make any difference which start time for the time range is chosen because by measuring in through-transmission mode, mainly variations in amplitude are of interest and changes are the same within the time window (typically recorded time window: 0.08 ms). The values of amplitude are usually integrated within a time range of 0.01 ms. As a result, an x -, y - image is evaluated which shows the position of an imperfection. After calculating a C-scan image, the data are stored in a three-column ASCII file (x -, y -position and amplitude). This file is processed with the help of the software "Display.img" developed by the laboratory of the Institute for Polymer Testing and Polymer Science (IKP), Department of Non-Destructive Testing (ZfP) to create again a C-scan image, but with flexible colour bars (Figure 28).

For quality assurance and for non-destructive testing, it is not only important to detect defects but also to measure their size. Both steps are necessary in order to monitor changes in defects that may result from further damage to a sample. A sample was made to determine the relation between the real size of the defect and the apparent size as given by the signal structure (Figure 31).

Strips with different width (true width x_t ; Figure 31; top) were attached on the top surface of a PMMA-sample. Between each strip and the surface there is a gap to simulate a delamination with an additional boundary which causes a decrease of signal.

Across this sample, a C-scan image was performed (Figure 31, middle). The dark areas (low amplitude) indicate the gaps. The echo dynamic curve (changes of amplitude dependant of x -position) was calculated across a line with the help of the c-scan data. Afterwards, the derivative of this curve was determined. The position of the peaks (indicating minimum and maximum and therefore the inflection points) of the derivative curve were used to estimate the apparent width x_a (Figure 31; bottom). The PMMA-plate was measured five times at different positions at the scan table and the sample was also horizontally rotated. The average value of x_a , the standard deviation, and the difference of average value of x_a and x_t were calculated (Table 9) from these five measurements.

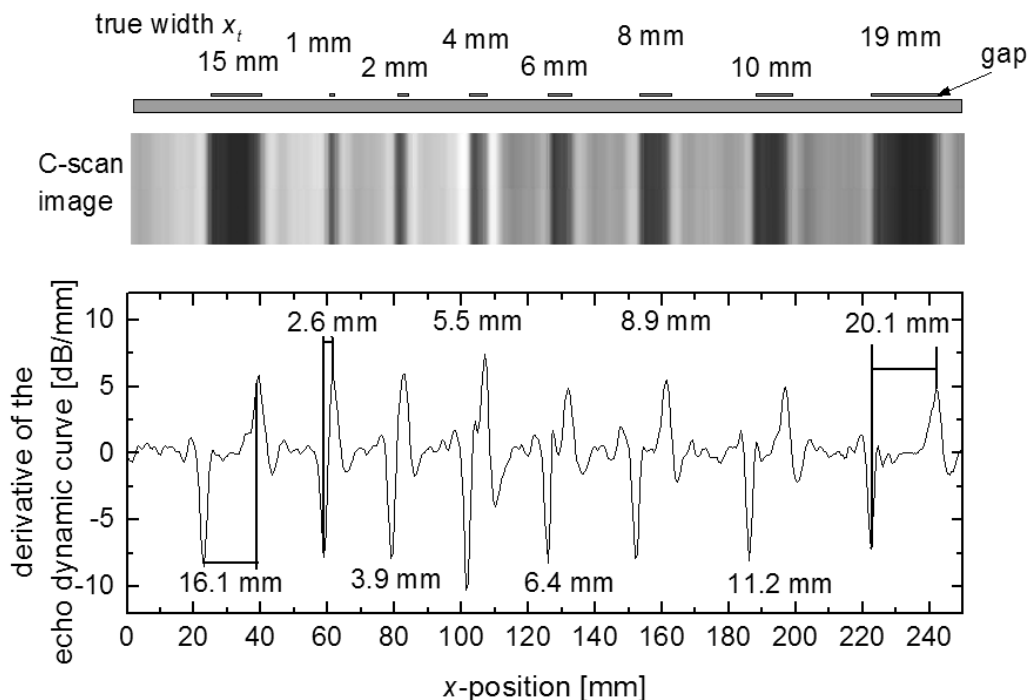


Figure 31: Measurement performed to determine the difference between the true size x_t and the apparent size x_a of a defect. The PMMA-plate has strips with a gap between the strip and the surface and different width x_t on top of the surface; top: drawing of the sample; middle: C-scan image of the sample (dark areas indicate the gaps); bottom: derivative of the echo dynamic curve to determine the apparent width x_a (shown are the average values of x_a).

true width x_t [mm]	average value of the apparent width of x_a [mm]	standard deviation of the apparent width [mm]	$x_a - x_t$ [mm]
1	2.6	0.42	1.6
2	3.9	0.22	1.9
4	5.5	0.30	1.5
6	6.4	0.42	0.4
8	8.9	0.22	0.9
10	11.2	0.27	1.2
15	16.1	0.42	1.1
19	20.1	0.55	1.1
average value:			1.2

Table 9: Comparison of the true width x_t and the average value of the apparent width x_a of strips on the surface of a PMMA-plate.

In Figure 32, the average values of the apparent widths x_a are plotted versus the true value x_t considering the errors for x_a and x_t (the errors of x_t was estimated). Both values have a nearly linear relation and the curve is shifted to higher values by an offset of 1.2 mm (indicated by comparison of the dashed line and the solid line in Figure 32 as well

as by the average value of the values of the right column in Table 9) and shown in Figure 33. As a result, within the range of 1 to 19 mm, there is an offset of 1.2 mm with a spread of 0.8 mm (Figure 33) between the apparent size x_a and the true size x_t of a defect.

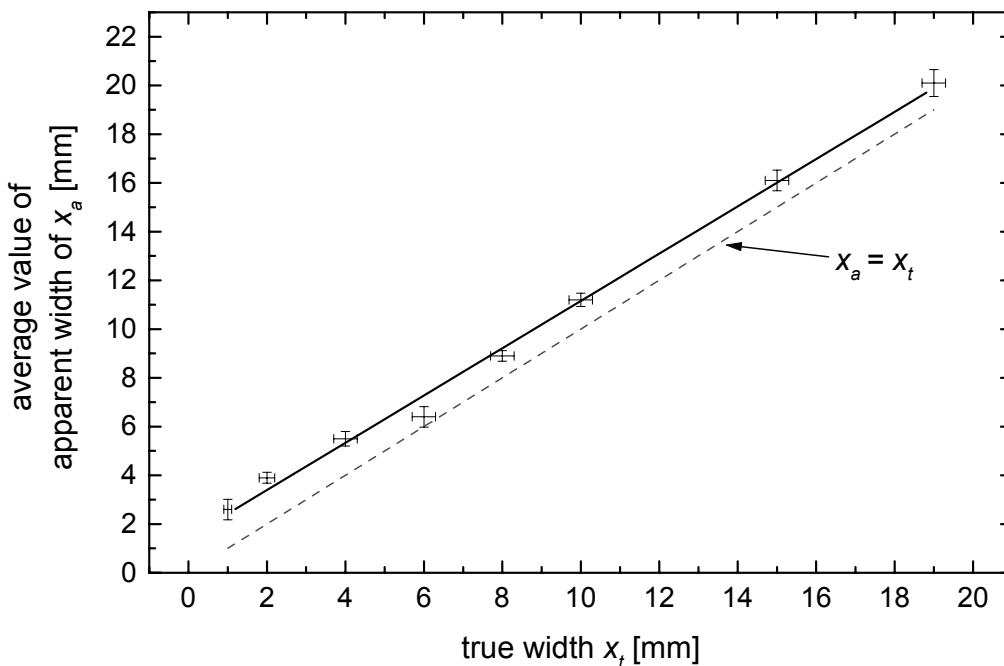


Figure 32: Average apparent widths of x_a plotted versus the true width x_t . The solid line indicates the measured relation and the dash line a hypothetic one (equality of both values). The offset between both lines is 1.2 mm.

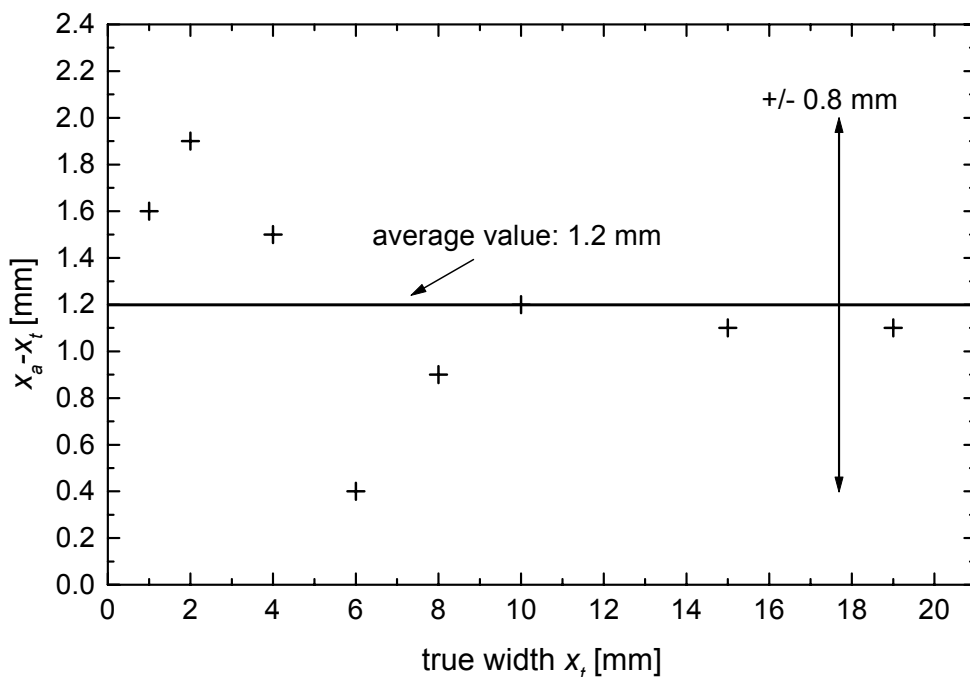


Figure 33: Plot of the difference between x_a and x_t versus the true value x_t . The average value is 1.2 mm with a spread of 0.8 mm.

One of the disadvantages of measuring in through-transmission mode is a signal overrange along the edges of a sample because of waves propagating around the edges and scattering. As long as the wave propagates through air and not through the sample, the ultrasound signals are damped less and cause overrange of signals. To find out the dimensions of this overrange area, a metal sheet (width: 14 mm) was fixed 40 mm apart from the edge of a PMMA- sample with double-face photo strip (width: 15 mm). For this sample, an ACU C-scan image was performed and compared with the dimensions of the sample (Figure 34 a).

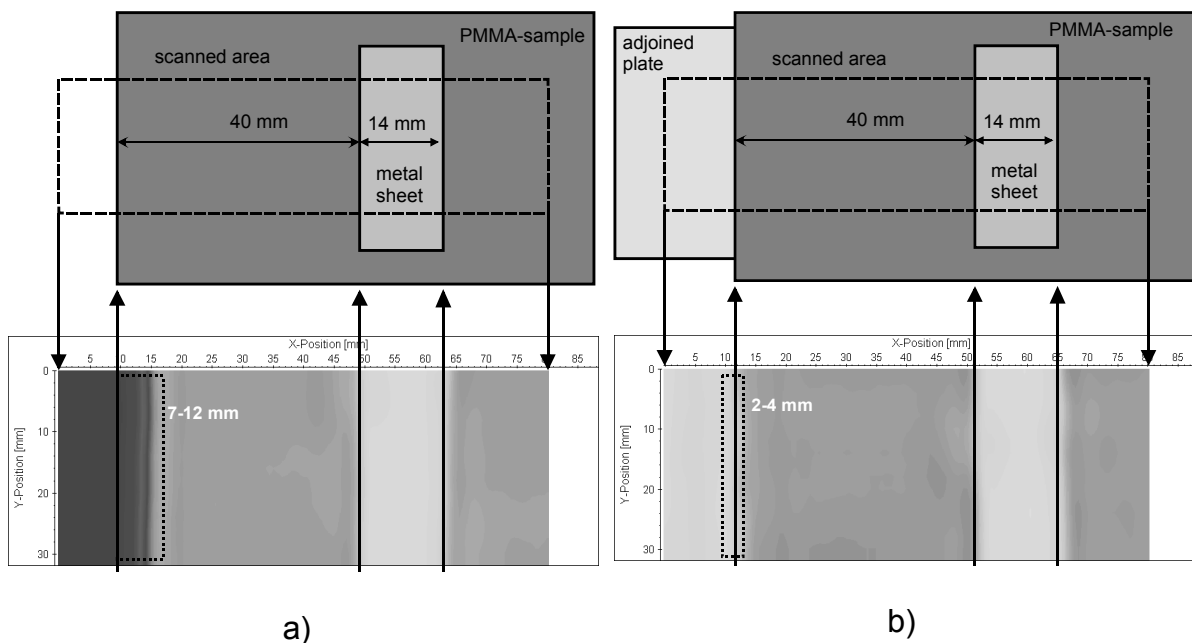


Figure 34: a) Drawing (top) and C-scan image (bottom) of a sample to examine the effect of overranged signals along edges. The overrange is indicated by dark area on the left side of the ACU C-scan presentation b) Drawing (top) and ACU C-scan image (bottom) of a sample to examine the influence of a plate joined to the test object on the signals along edges. The lack of overranged signals is indicated the bright area on the left side of the ACU C-scan image.

The edges of the metal sheet and also the edge of the sample were found. The estimate of the area that cannot be inspected could be evaluated, and ranges between 7 mm and 12 mm depending on the gain chosen. The overrange of the signal is indicated by the dark area on the left side of the ACU C-scan image. To reduce the area along the edges that cannot be inspected, it is possible to join a plate to the sample with an overlap of about 1-3 mm (Figure 34 b). Hot-melt glue was applied along the edge to prevent sound from going through the interface between the sample and the plate. This application must be done very precisely; otherwise there will be an overrange of signal if the joint is not done well. As a result, the width of uncertainty can be reduced to 2 to 4

mm. This width depends mostly on the overlapping of the sample and the joined plate, and on the width of the hot-melt strip. For narrow samples and for samples with imperfections close to the edge, it is important to know this effect and to reduce it by joining an additional plate to the sample.

5.4 Performing measurements with non-linear ACU inspection

In contrast to linear ultrasound inspection (which displays changes of amplitude because of changes of impedances), non-linear ultrasound inspection selectively displays an increase of amplitude because of higher harmonics that are only produced at nonlinearities (section 3.2). If there is no source for generation of higher harmonics, only noise is detected. The basic idea of non-linear ACU inspection is that the frequency spectrum of the excitation source and the receiver are not identical and do not overlap like at linear ultrasound inspection. The centre frequency of the excitation source is chosen that the centre frequency of the narrow band receiver is an overtone of the fundamental frequency. To perform non-linear measurements, the only difference to be made to the equipment is that the air-coupled transmitter is switched off because it can be operated only at 450 kHz and the burst signal itself produces higher harmonics. Instead, an external excitation source (e.g. piezo-transmitter glued to the sample) or an internal excitation source (e.g. piezo-transmitter directly embedded into the sample) injects a sinusoidal wave into the sample. The excitation source is driven by a wave generator and an amplifier for generation of continuous sinusoidal waves. In the case of non-linear ACU, the sample is excited at fundamental frequencies (e.g. 150 kHz, 225 kHz) that have 450 kHz as an overtone. The narrow band receiver tuned to 450 kHz scans across the sample. In defect-free areas, only the fundamental frequency is emitted that cannot be detected with this narrow band receiver. The scan is made across a defect however, the narrow band receiver responds selectively to the higher harmonic frequency of 450 kHz. A schematic drawing of non-linear ACU inspection is shown in Figure 35. From the data recorded, a higher harmonic image is evaluated similar to a C-scan image. This higher harmonic image can either be classified as an F-scan image (Table 8) because it displays the appearance of one frequency, or as a C-scan image because the amplitude is shown. In the following parts of this work, this type of image is called either a C-scan image (for which the expression is well known) or is called a “higher-harmonic image” in order to be clear that a higher harmonic is shown.

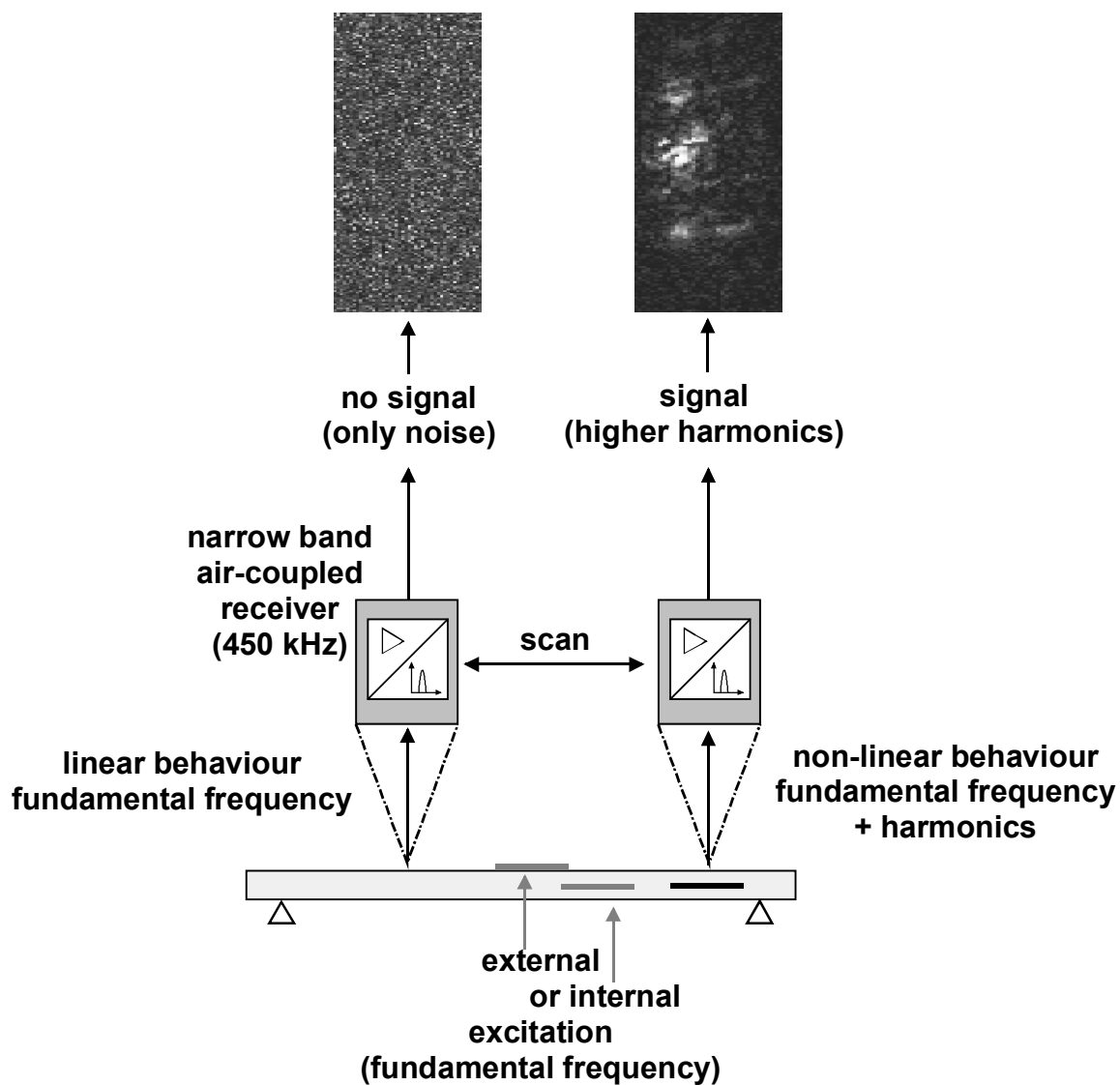


Figure 35: Non-linear ACU inspection method: The receiver responds only to a harmonic of the excitation (fundamental) frequency.

6 Applications

This chapter presents results obtained from a variety of different materials and components and compares the results with those of other NDT techniques in order to demonstrate the capabilities of air-coupled ultrasound inspection techniques.

6.1 Wood

Solid wood as a construction material is used for roof structures of large halls, or as decorating or pylon material. Therefore, it is important to inspect wood components during manufacture and during use. Wood is very complex; each tree-trunk is different and the factors that affect wood properties are not yet fully understood. As a result, much ongoing effort is devoted to studying wood [124]. Non-destructive characterisation of wood is also a topic of major interest in the collaborative research centre SFB 381 (German Science Foundation; DFG) where the failure of wood due to various kinds of defects is investigated. Contact ultrasound is one of the techniques [125,126]. The major problem, though, is how to couple elastic waves into wood. Contact coupling is difficult because on rough surfaces, scanning over the sample is not possible and water as a liquid coupling medium would penetrate into the wood and affects its properties. The influence of water on solid wood and therefore on ultrasound signals was verified with a 10 mm thick wooden sample that was first measured with ACU (dry wood; Figure 36), then kept in a water bath for 30 minutes and measured again (wet wood; Figure 36). The decrease of the ultrasound signals because of absorbed water is about 16 dB. This result proves that water has a strong influence on ultrasound inspection of water sensitive materials and that measurements in a water tank would not be an appropriate method. With air-coupling, however, remote measurements are now possible.

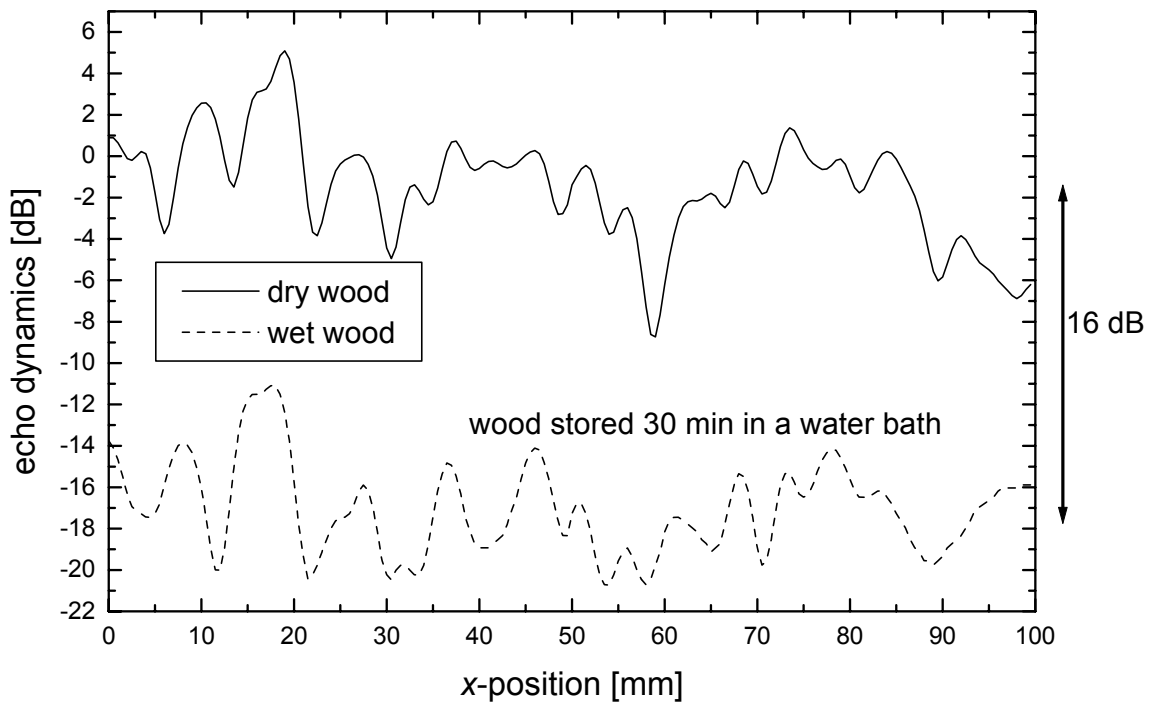


Figure 36: ACU applied for inspection of wood: echo dynamic curve of a solid wood sample before and after storing in water.

6.1.1 Solid wood

After cutting solid wood, it is necessary to examine the direction of the wood grain in order to know what uses can be made of the specific piece of wood because the elastic properties depend on the direction of the fibres [127]. Ultrasound inspections to classify wood have been done before [128], but coupling is a problem. With an ACU B-scan, the structure can be inspected more readily. Local variations in the structure (Figure 37) can be detected in the ACU B-scan image, shown as differences in the amplitude of the transmitted signal. The ACU B-scan presentation of a more homogeneous piece of wood is illustrated in Figure 38. The variations of amplitude on the ACU B-scan presentation are caused by earlywood and latewood. Earlywood is softer, lighter in colour, thin-walled, has a lower density, and has larger cell size. Latewood is harder, darker in colour, thick-walled, and has a higher density, as well as a smaller cell size. Thus, there are variations in the transmission coefficient, ultrasound absorption, and sound velocity. The changes in sound velocity can be seen in phase shifts shown in Figure 37 and Figure 38. Furthermore, the variations of amplitude in Figure 37 are caused by “sound” channels that consist of boundaries of early- or latewood so that the waves are guided and not merely transmitted perpendicularly. These two ACU B-scan results confirm the ability of ACU inspection to sort pieces of wood according to their

structure. This type of inspection could be made by naked eye as well. It is easy to automate this process, however, and automation offers the possibility of reduced labour costs and eliminates monotonous work, which are two major topics in modern quality assurance.

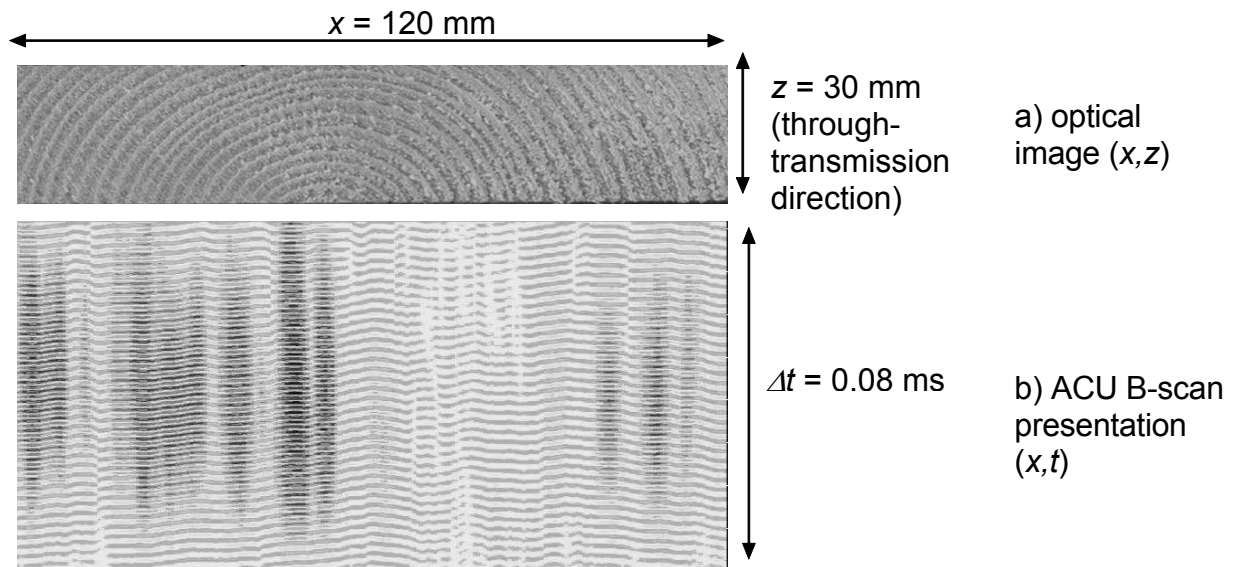


Figure 37: Spruce wood sample of 30 mm thickness; a) optical image of spruce wood; b) ACU B-scan image (through-transmission) (sample kindly provided by G. Dill-Langer; FMPA-BW, Stuttgart).

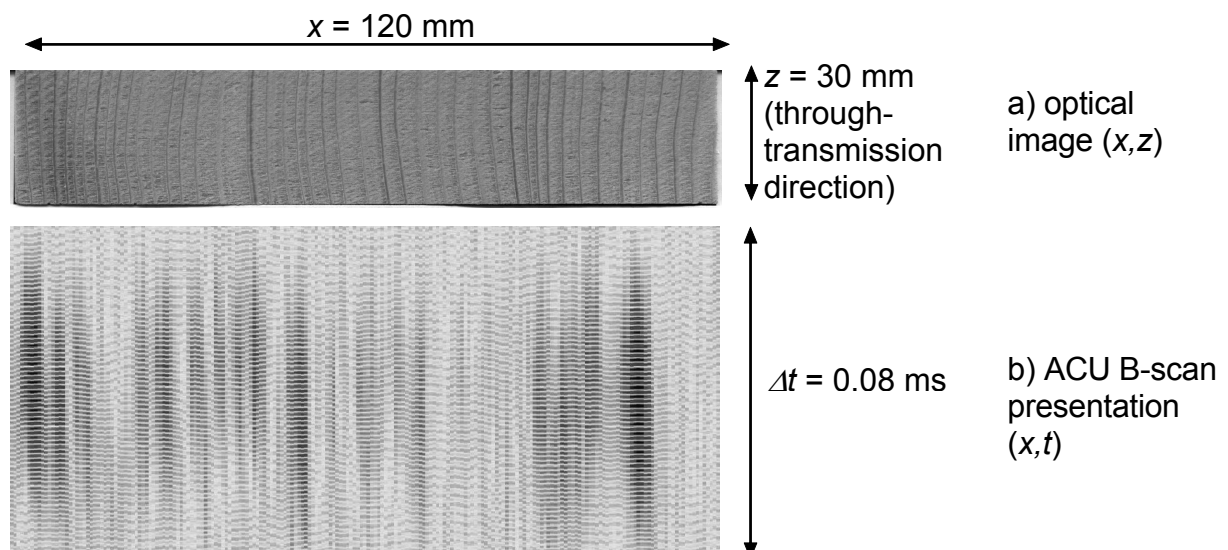


Figure 38: Spruce wood sample of 30 mm thickness; a) optical image of spruce wood; b) ACU B-scan image (through-transmission) (sample kindly provided by G. Dill-Langer; FMPA-BW, Stuttgart).

Because wood is a natural product, it may have hidden defects, such as subsurface knots that can be a potential source for failure of wooden components. Therefore, a sample was chosen in which the knots can be seen by the naked eye in order to have a hint where they are located. On the ACU C-scan presentation (Figure 39), the dark areas indicate the size and the location of the knots (inside the white squares). The structure of the wood sample (annual structure) is displayed by dark and bright horizontal lines.

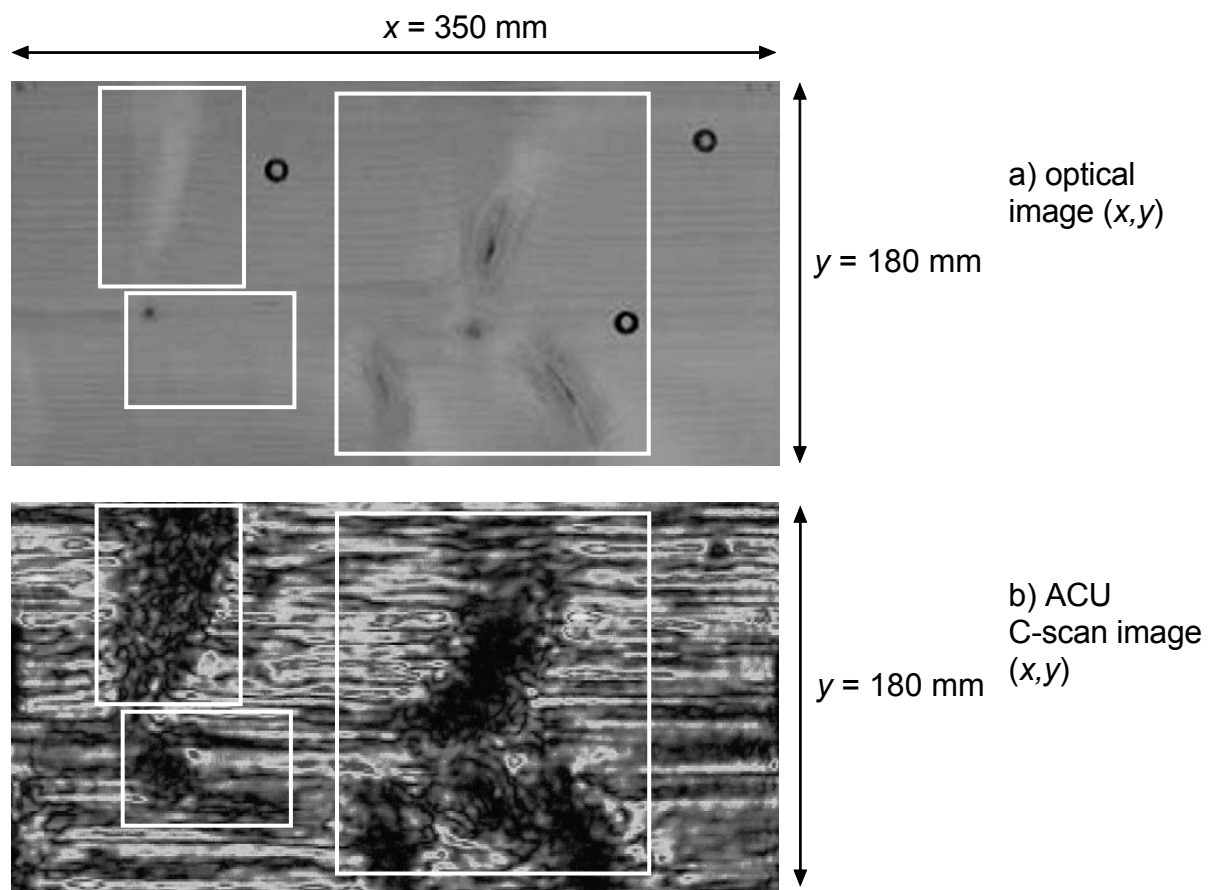


Figure 39: Spruce wood sample of about 20 mm thickness; a) optical image with knots (the three dark circles are used as markers, the white squares indicate the knots); b) ACU C-scan image of the sample (sample kindly provided by G. Dill-Langer, FMPA-BW, Stuttgart).

The question may arise as to whether ACU detects only surface changes. To answer this question, holes (not visible from the top and bottom surfaces) with different diameters and variations in depth were drilled into a sample of spruce wood (Figure 40 a). The resulting ACU C-scan image is shown in Figure 40 b.

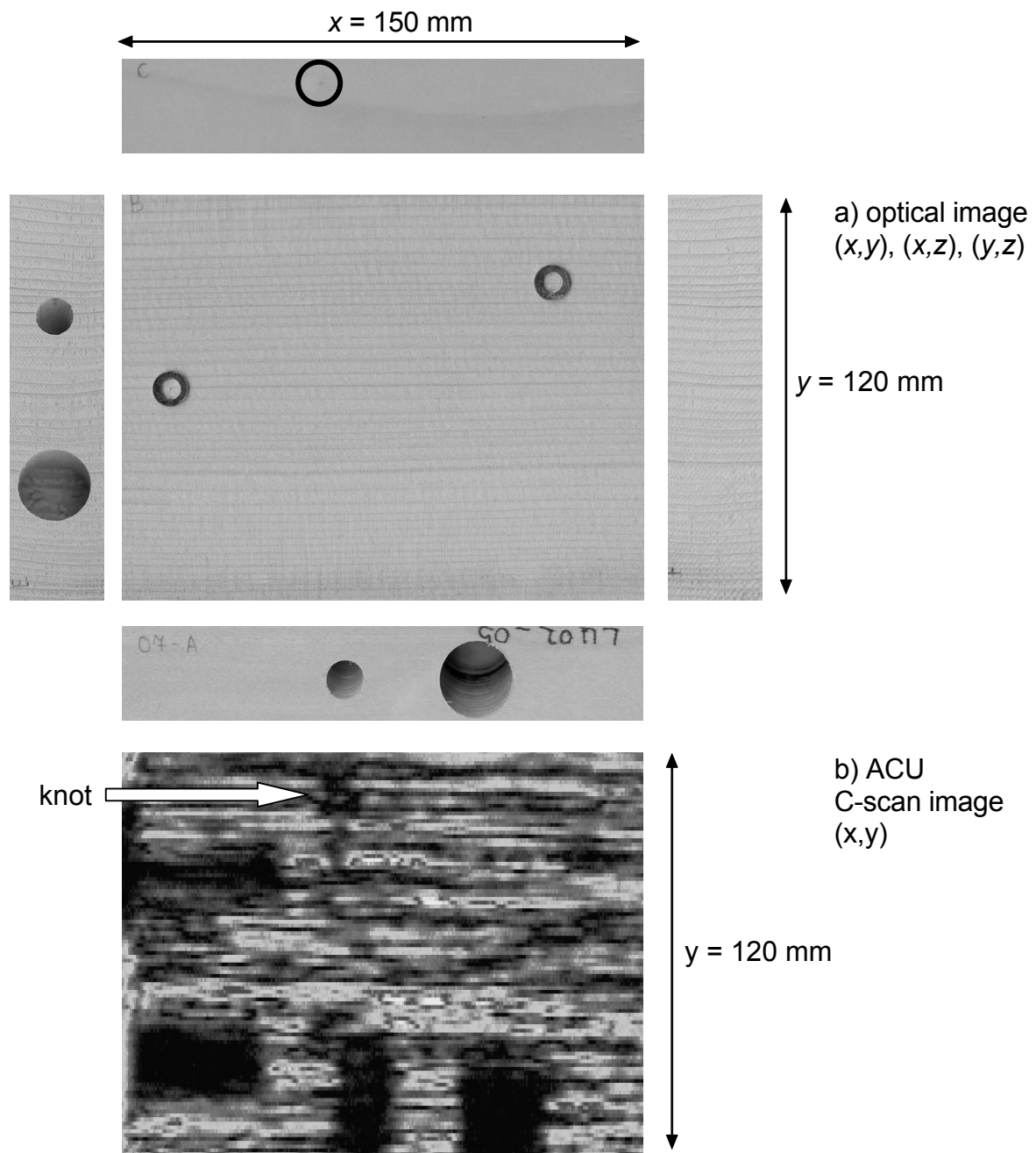


Figure 40: Spruce wood sample of 30 mm thickness; a) optical image with drilled holes and hidden knots (upper black circle); b) ACU C-scan image of the sample. The white arrow points at the hidden knot (sample kindly provided by G. Dill-Langer; FMFA-BW, Stuttgart).

The different holes (black areas in Figure 40 b) are detected and also a hidden knot (white arrow) that is difficult to see with naked eye.

6.1.2 Wood veneer sample

Most furniture parts are made of wood veneer. In the furniture industry, there is an increasing need to inspect the production and joining process of this type of material. With air-coupling, remote measurements are feasible in this case. Figure 41 displays the C-scan image of a wooden veneer sample with areas of missing glue of different width below the veneer layer (dark areas). Additional defects in the upper right of the image can also be seen [129]. This result is consistent with images obtained using optical lockin thermography [130].

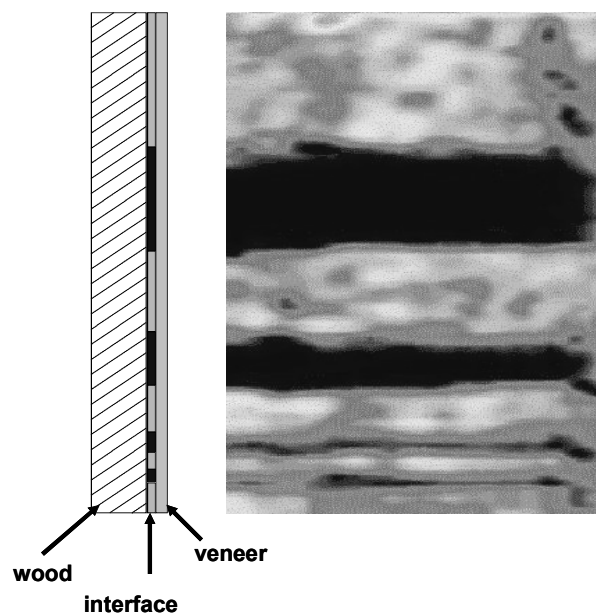


Figure 41: Drawing and ACU C-scan image of a wood veneer sample (thickness: 10 mm; scanned area: 30 mm x 80 mm) (sample kindly provided by H. Berglind Tratek, Swedish Institute for Wood Technology Research).

6.2 Carbon Fibre Reinforced Plastic (CFRP)

In the aerospace and automotive industries, there is a growing demand for materials with specific properties that cannot be met by traditional materials like steel and aluminium. An important alternative material is CFRP which is used increasingly due to its high specific strength. Because of the ability to arrange long carbon fibres in different directions, with a varying number of layers, and embedding them with epoxy resin or thermoplastic materials, different mechanical properties of CFRP can be achieved that suit the requirements. During the manufacturing process, which is still mostly manual, it is important that the layers are bonded with each other and that there are no delaminations between two layers. Also, this kind of defect can occur during usage because of

load or bending. In addition, impact damage that happens in service can be critical for CFRP-components. Because CFRP-materials are used with increasing frequency for safety-relevant components, there is a growing need for reliable non-destructive testing techniques in the field of after sales quality assurance.

6.2.1 Impact Damage

Impact damage to CFRP is difficult to avoid because the damage can be caused by such things as stones or falling tools. Usually, almost no damage can be seen on the impact side because the surface layers are supported by the lower layers. Nonetheless, interior layers may break causing an internal defect, and the greatest damage may occur on the opposite side of the surface where the impact took place (Figure 42).

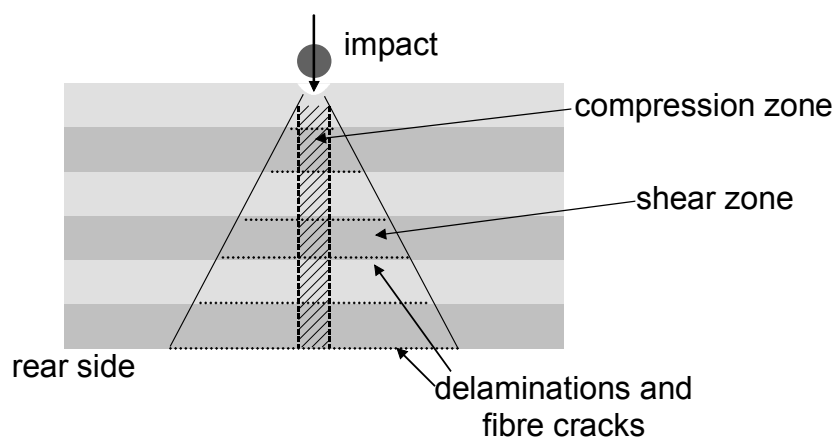


Figure 42: Cone structure of an impact damage.

This hidden damage can be a safety risk because technicians who are inspecting airplanes, for example, are accustomed to finding damages in such materials as aluminium which shows almost the entire extent of the damage on the surface.

Measurements have been made on a CFRP-plate (quasi isotropic laminate; thickness: 1 mm; orientation of the surface layers 45°) with seven impact damages of the same impact energy level. On the side where the impacts occurred, only a small amount of damage with a diameter of about 0.5 mm can barely be seen. On the rear side, though, the fibres are broken so that the damage (40-45 mm in length) is readily visible. All seven impacts and their 45° -orientation are detected with linear ACU in through-transmission mode (Figure 43a). The same sample was also inspected with ULT (Figure 43 b) and with the non-linear vibrometry technique (Figure 43 c) [131]. These

techniques display the seven impacts as well. While ACU is sensitive to changes in acoustical impedance, ULT detects local mechanical hysteresis, and non-linear vibrometry shows areas with high mechanical distortion factor. ULT displays in addition the centre of the impact damage where the impact took place. This was not seen with non-linear vibrometry. To prove whether the centre can also be found with ACU, one impact was inspected more precisely.

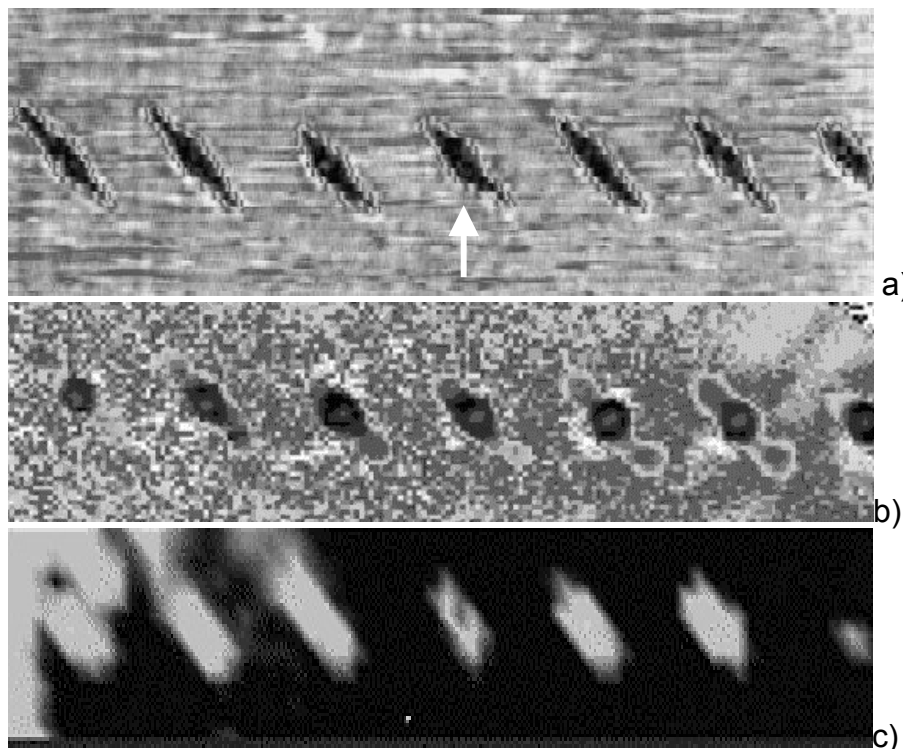


Figure 43: CFRP-sample (295 mm x 142 mm x 1 mm) with seven impact damages; a) ACU (through-transmission mode); b) ULT phase image (0.03 Hz); c) non-linear vibrometry (5th harmonic image; fundamental frequency 20 kHz) [131] (sample kindly provided by R. Aoki; DLR, Stuttgart).

A closer look of the impact in the middle (Figure 43 a; white arrow) is displayed on the ACU C-scan image in Figure 44 (lower right). The place where the impact occurred and also the gradation of damage between the impact and the material around it can be inspected. A criticism of air coupling is the small signal-to-noise ratio of the signals received due to the large impedance mismatch between solid and air. The signal change of approximately 22 dB in the echo dynamic curve across the impact (Figure 44), which is caused by the impact, is clearly over the noise level of about 1-2 dB. The decrease in the signal is caused by additional boundaries resulting from delaminations inside and on the rear side of the sample. It is interesting that in the area around the impact the signal level reaches almost the height of the undamaged neighbourhood. At the centre

where the impact occurred there is a normal stress field (compression zone) which does not cause damage (longitudinal waves), while at the edges there are tangential stresses along an increasing length at the same angle of the cone which are causing damage at the outer part of the cone (shear zone). The extension of the impact of about 8 mm found on the C-scan image is larger than the visible extension (width: 2-4 mm).

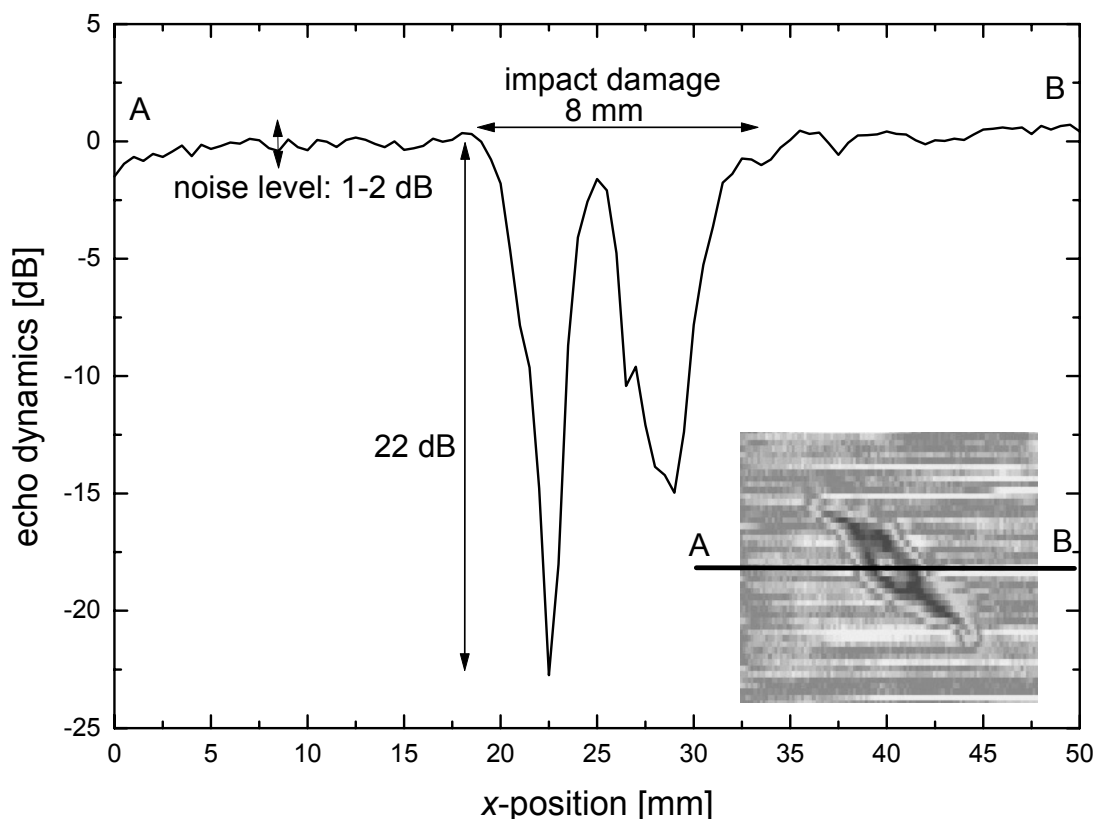


Figure 44: Echo dynamic curve across (A-B) of an ACU C-scan image of an impact displayed on the lower right. The signal peak in the centre indicates the compression zone.

As seen in Figure 43 c, the non-linear behaviour of the impacts can be used for localization of the damages and was detected by non-linear vibrometry. So it should also be possible with non-linear ACU technique. Therefore, the same sample was inspected using this non-linear technique which can be performed with single-sided access. This time only five of the seven impacts were inspected. As an excitation source, two piezo actuators were glued to the sample with hot melt glue (dark half-circles on the ACU C-scan image performed in through-transmission mode; Figure 45 a). Thus, it is not a true non-contact method. Nonetheless, the signals are received through air and not through water. The ACU C-scan in transmission mode displays the locations of five

impacts and of the two actuators (Figure 45 a). By exciting the actuator at 225 kHz and using the 2nd harmonic frequency for imaging, four impacts can be seen. The impact directly above the actuator on the left side, which was used as ultrasound source, is not clearly detectable because of higher harmonics caused by the clapping of the piezo ceramic. Only noise is received when the plate is excited with 320 kHz (Figure 45 c) which is close to the maximum sensitivity at 450 kHz and which has no higher harmonic at 450 kHz. These results confirm that only the overtone frequency at 450 kHz is detected.

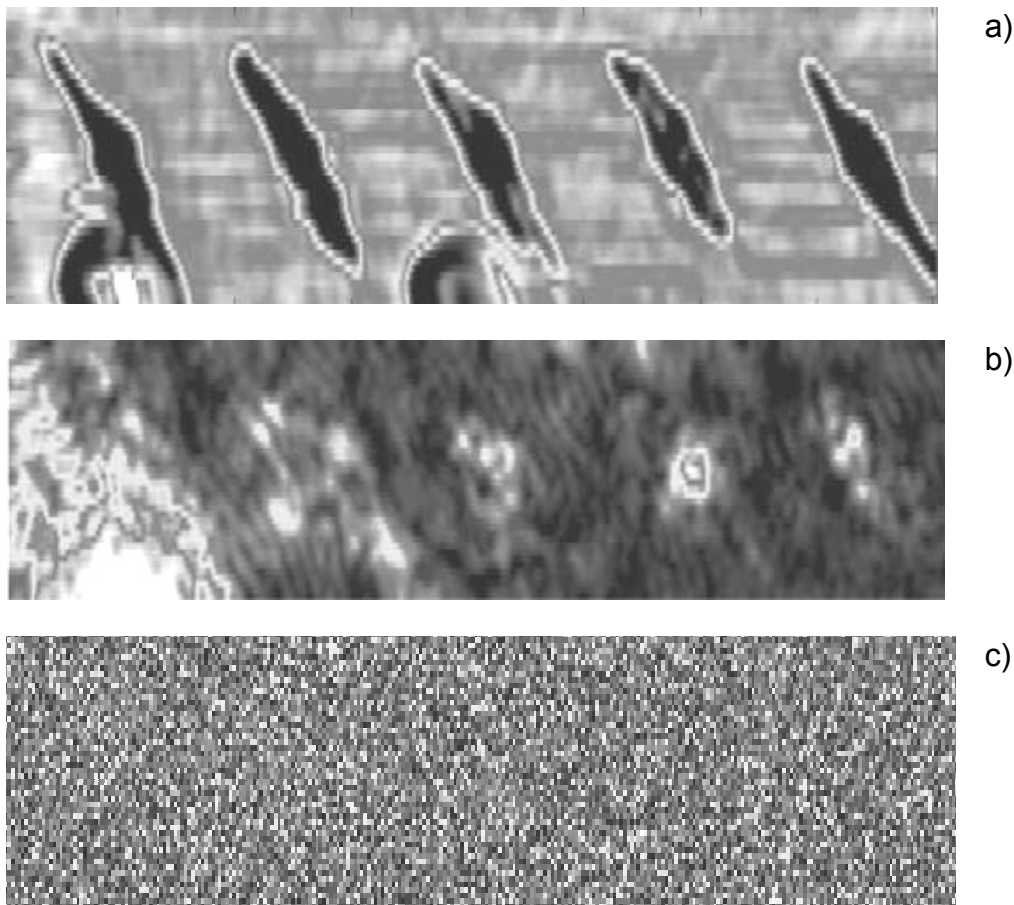


Figure 45: CFRP-plate with seven impact damage (five are only shown here, see also Figure 43); a) linear ACU through-transmission technique; b) 2nd harmonic image (excitation: 225 kHz, detection: 450 kHz); c) image performed with excitation frequency of 320 kHz (scanned area: 190 mm x 65 mm).

In addition to impacts that can be seen on the rear side, impact damages that are not visible with the naked eye need to be inspected. Also CFRP-materials used for aerospace applications are in general thicker than the sample shown in Figure 43. Thus, a 14.5 mm thick CFRP-sample was impacted. On the front side, where the impact occurred, only a small and shallow impact (diameter: 10.2 mm; depth: about 0.15 mm;

Figure 46 (measurement kindly performed by H. Gerhard; IKP, University of Stuttgart) can be seen.

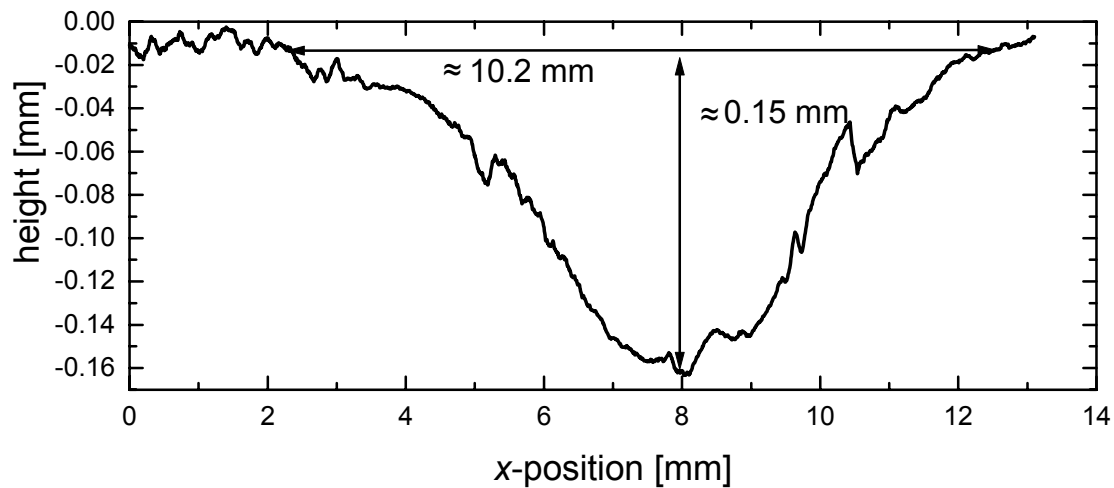


Figure 46: Surface scan performed by Laser-Scanning Microscopy (LSM) across an impact damage of a CFRP-sample (sample kindly provided by D. Almond; Materials Research Centre, University of Bath, UK).

On the rear side, nothing can be observed. The ACU C-scan presentation (Figure 47 a), however, shows an extension of the impact of about 50 mm x 40 mm. This result verifies that the hidden damage caused by an impact is larger than the visible one. Because the through transmission technique is an integral method along the thickness of the sample, the cone structure cannot be found, and only the entire extension of a defect is seen. OLT is sensitive to thermal interfaces, and single-sided measurements from the front and from the rear side of the sample show the increase of damage size on the phase images (phase 0.01 Hz; measurement kindly performed by G. Riegert, IKP, University of Stuttgart). The shape of the defect is not as sharp as inspected with ACU because of distortion of thermal waves. If the extension of a defect is of interest with OLT, double-sided access is needed and two measurements must be performed while with ACU inspection, only one is needed.

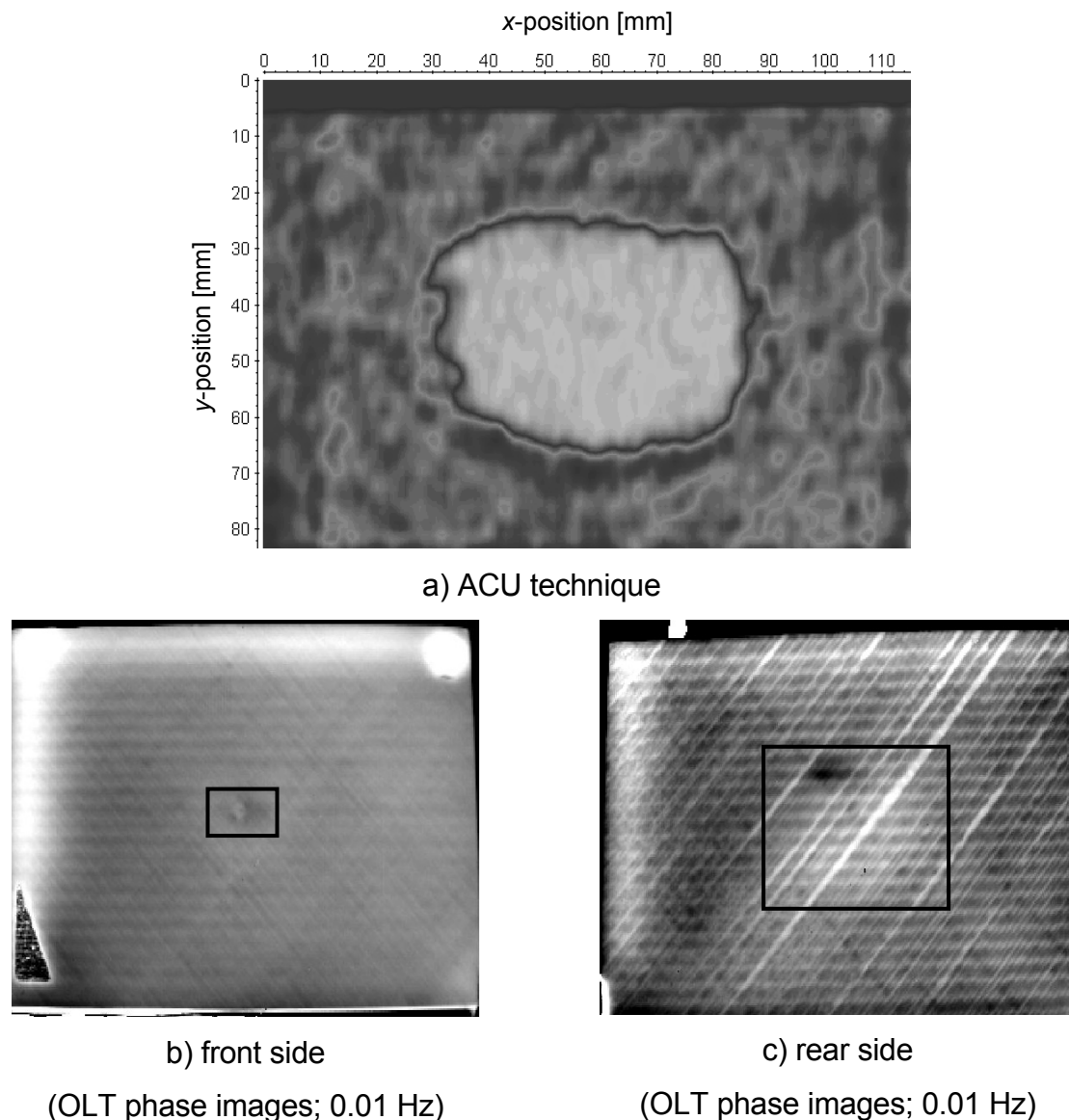


Figure 47: CFRP-sample (thickness: 14.5 mm) with impact damage; a) ACU inspection, b) OLT phase image performed from the front side (phase 0.01 Hz); c) OLT phase image performed from the rear side (phase 0.01 Hz) (sample kindly provided by D. Almond; Materials Research Centre, University of Bath, UK).

In addition to the detection of impacts, it is important to know whether it is possible to distinguish among different impact energy levels and the size of the impacts. Therefore, a defect-free CFRP-plate was first inspected with ACU to make sure that there are no imperfections in the plate (not shown in this study). Out of this plate, three samples were made and impacted with three different energies. The damage caused by the lowest impact energy of 329 mJ could not be detected with either linear nor with non-linear ACU inspection (Figure 48). The damage caused by the two other impacts with energies of 617 mJ and 986 mJ were detected with linear- and non-linear ultrasound inspection. Likewise, other non-destructive testing techniques, such as optical lock-in

thermography or non-linear vibrometry, were not able to identify the impact with the lowest energy level but the other two impacts were also found [132].

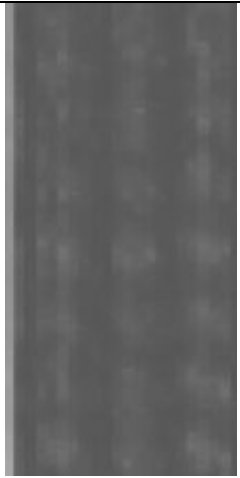
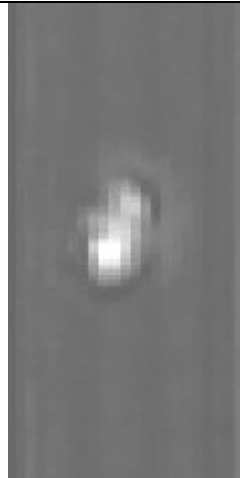
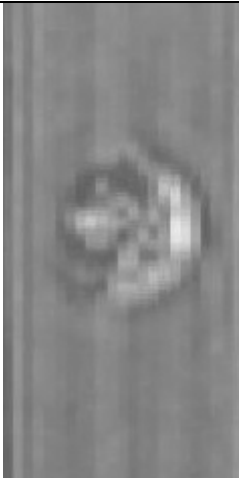
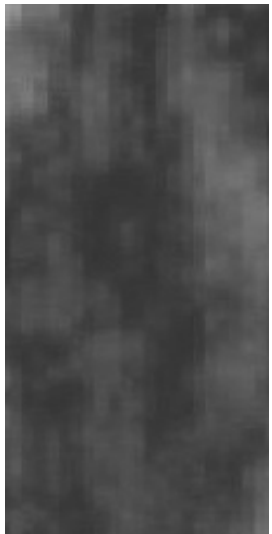
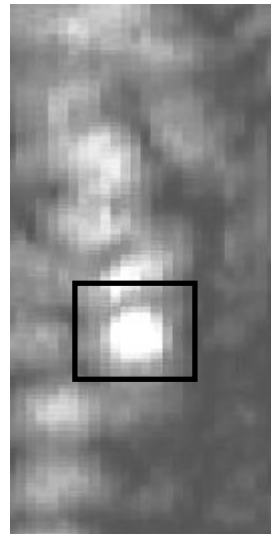
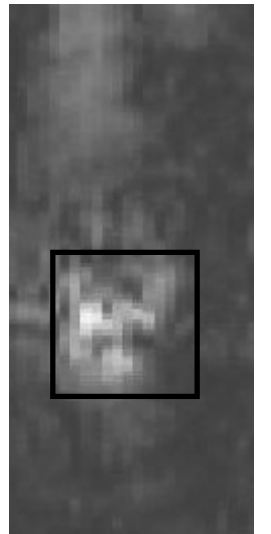
	impact energy level: 329 mJ	impact energy level: 617 mJ	impact energy level: 986 mJ
through- transmission image			
non-linear image			

Figure 48: Comparison of impact damages with 3 different energy levels in CFRP-samples (thickness: 2 mm) inspected with linear (top) and non-linear (bottom) ACU techniques (displayed area: $\approx 30 \text{ mm} \times 65 \text{ mm}^2$).

By measuring the size of the impacts on the through-transmission images, it is found that the size increases with increasing energy (617 mJ-impact: $\approx 7 \times 9 \text{ mm}^2$, 986 mJ-impact: $\approx 12 \times 15 \text{ mm}^2$). Also, on the 2nd higher harmonic images, an increase of size is seen. It is not possible to qualify the size, however, because the images are not as sharp as in through-transmission. This result is caused by the two different physical properties that are used to display the defects: First, linear ultrasound makes use of reflection and transmission of waves at acoustical boundaries. Therefore, the entire shape of this imperfection is seen because the interface behaves the same all over the

additional surface (section 2.4). Second, non-linear ultrasound displays the relative movement of the boundary (section 3.2). This movement may differ within the interface because two surfaces may be close together. As a result the CAN threshold for non-linear behaviour may be overcome. In other areas, though, the surfaces are separated from each other so that the CAN threshold is not passed.

6.2.2 Delamination

In addition to impact damage, delaminations between two layers can occur in CFRP-materials. The delamination of two layers can happen during the manufacturing process because of a mould release agent that is commonly used to prevent the component from sticking to the form. Delamination can also occur during use because of heterogeneous distribution of epoxy resin or by mechanical damage.

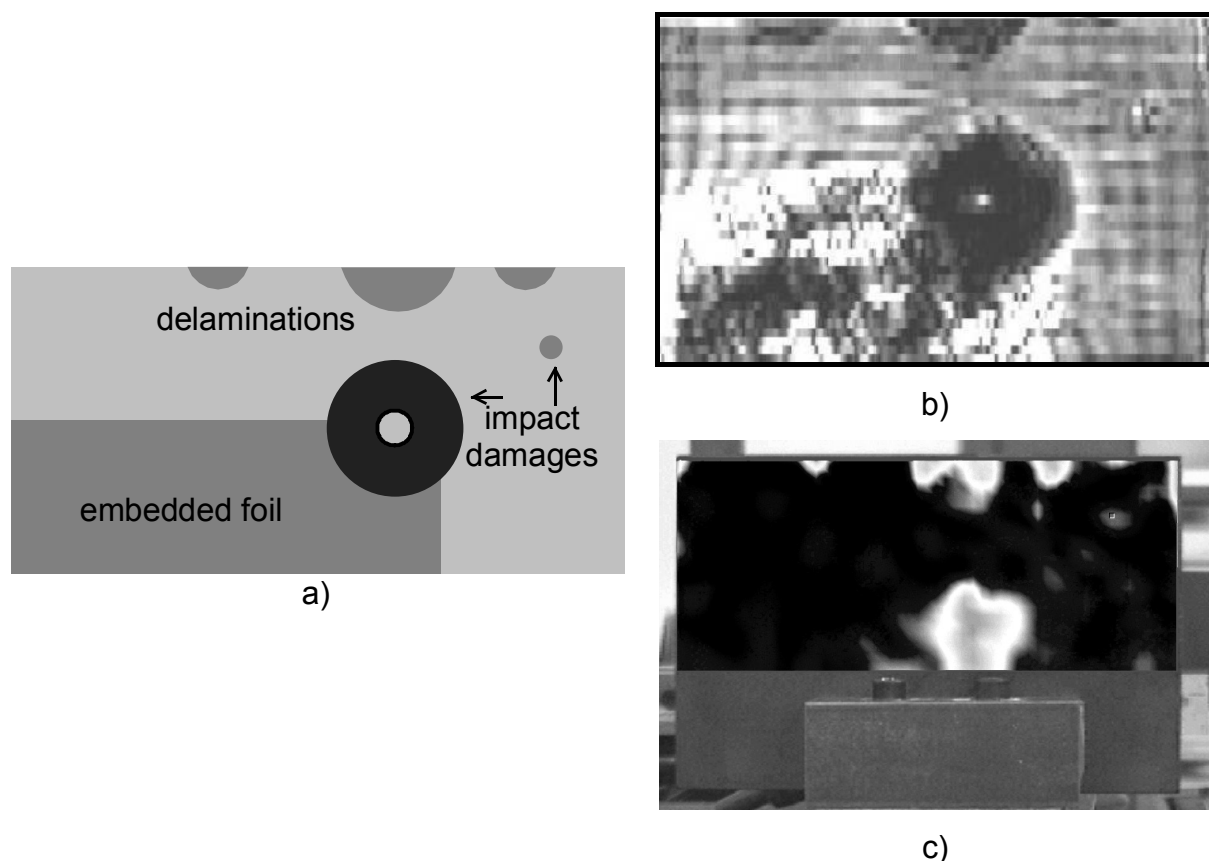


Figure 49: CFRP-sample (size: 150 mm x 100 mm x 4 mm) with artificially made delaminations at the edges, with two impact damages, and with embedded foil; a) drawing of the sample; b) linear ACU C-scan image; c) 3rd higher harmonic image (fundamental frequency of 20 kHz).

The sample shown in Figure 49 a has three artificially made delaminations at the upper edge, two impact damages, and an embedded foil. Artificially made defects are a pos-

sibility to qualify non-destructive testing techniques (section 1.2). On the ACU C-scan presentation, all defects are found (Figure 49 b). While on the 3rd harmonic image performed with non-linear vibrometry (Figure 49 c [39]), only the impacts and the delaminations are found but not the embedded foil. It seems that the foil does not behave non-linearly and is therefore not a source of higher harmonics. Measurements with non-linear ACU failed because with the excitation via a glued-on piezo actuator, the excitation amplitude was not high enough to pass the CAN threshold because the sample was too thick and the surfaces of the interface were separated too much. The inspection with non-linear vibrometry was feasible because the sample was driven with a modified welding sonotrode which was able to provide the amplitude needed. This sonotrode is operated at 20 kHz and this is not suitable for the non-linear ultrasound technique used in this study. For thinner samples, however, the piezo actuator provides enough power to generate higher harmonics at delaminations. A CFRP-sample (cut out of the defect-free CFRP-plate mentioned above) was first inspected with non-linear ACU, with OLT, and with optical microscopy to make sure that no defect occurred during the cutting process. With all three techniques, no delaminations were found. After putting cyclic load (235 000 cycles; 10 MPa - 300 MPa) on the sample, delaminations along the edges arose. They are detected with all three techniques (Figure 50). The black circles on the OLT-phase images indicate the position of the piezo actuators which are not shown on the non-linear images. This time linear air-coupled inspection was not able to detect the delaminations because they were too close to the edges (see also section 5.3) [132].

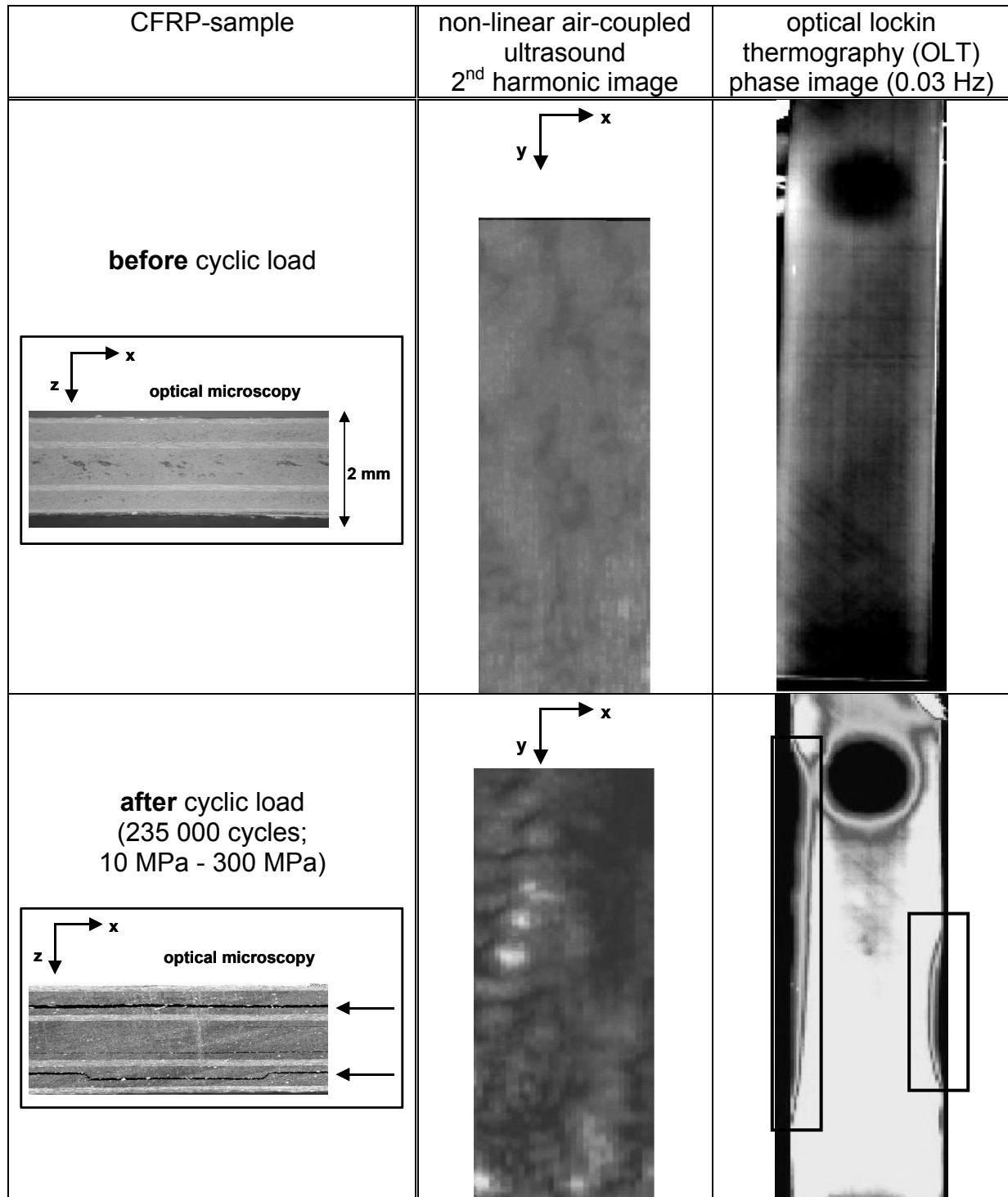
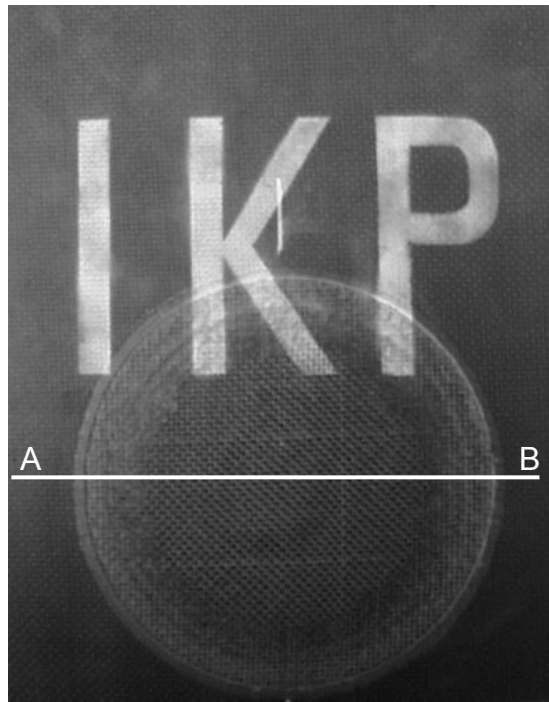
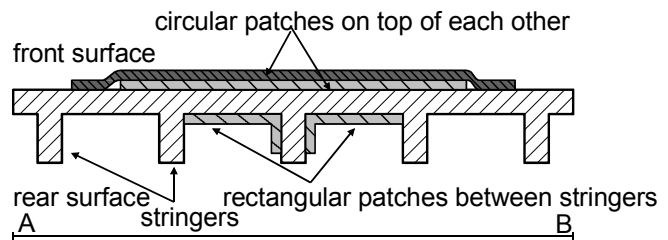


Figure 50: Monitoring of the occurrence of delaminations caused by cyclic load at CFRP-sample (sample size: 220 mm x 45 mm x 2 mm) with non-linear ACU (2nd harmonic image; column in the middle) and OLT phase images (0.03 Hz; column on the right-hand side).

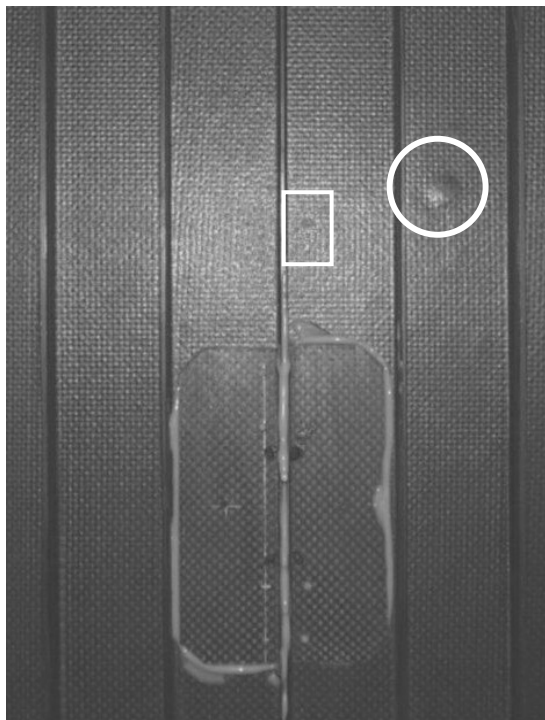
6.2.3 Repaired CFRP-structure



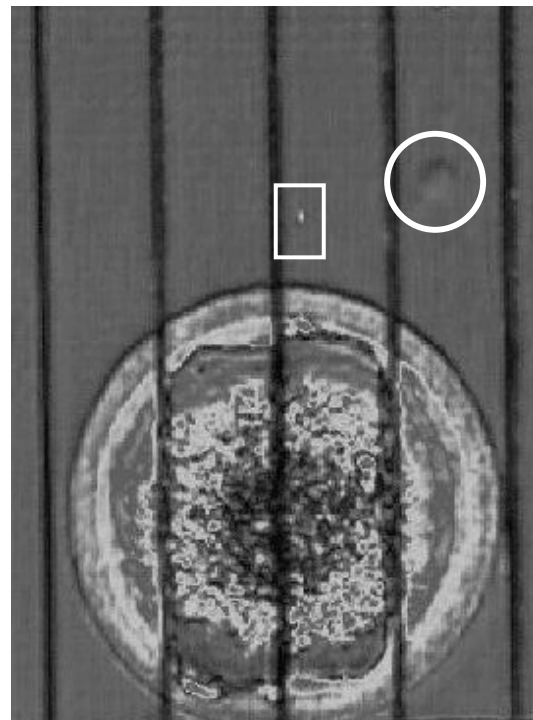
a) front surface (optical image)



b) drawing of the component



c) rear surface (optical image)



d) C-scan image (through transmission)

Figure 51: a) and c) Optical images of a repaired airplane component (sample size: 225 mm x 270 mm x 2 mm); b) drawing of the sample; d) ACU C-scan image in through-transmission mode (sample kindly provided by R. Aoki; DLR, Stuttgart).

For quality assurance, it is not only important to detect defects but also to inspect repaired damage (e.g. impacts or delaminations) of CFRP-components and to monitor

the quality of the result achieved with non-destructive testing methods. This monitoring is also possible with ACU inspection as displayed in Figure 51 using a repaired airplane component (thickness: 2 mm) with stringers. On the front side, two circular patches are on top of each other (Figure 51 a, b) and on the rear side (Figure 51 b, c) there is a rectangular patch that matches the stringers. The C-scan image (Figure 51 d) shows the three patches, and illustrates that the result of the repair is very homogeneous. Furthermore, a small glue spot (diameter: 3 mm; white rectangle) and a delamination (diameter: 14 mm; white circle) can be detected. The dark horizontal lines on the C-scan presentation are caused by the integrated stringers. A similar result was obtained by OLT with multi frequency excitation [133], but the glue spot was not found.

6.3 Cure monitoring of epoxy resin and detecting disbonds in adhesive joints

In the automotive and aerospace industries, the use of adhesive bonding of components is currently increasing in popularity. In modern cars, the joint length is about 100 m. Adhesive joining has many advantages over welding and riveting including higher structural integrity, improved corrosion performance, reduced weight, and more flexibility in the design of components regarding materials and shapes. Also reduced manufacturing costs and the elimination of rivet-induced fatigue problems make adhesive bonds an attractive possibility for joining. The use of adhesive bonding in safety relevant structures has been slow partly because of the lack of reliable and predictable non-destructive testing methods to monitor the cure process and to assure the condition of the bond. For quality assurance of industrial applications, though, it is essential to know the quality of adhesive joints and to monitor the curing process. Many efforts are ongoing in the non-destructive community to develop or to adapt testing techniques. To monitor the cure process, such methods as mechanical spectroscopy of metal bars [134], dielectric methods [135], infrared techniques [136], acoustic emission [137] and the characterisation of the curing process [138] are discussed in the literature. Also ultrasound inspection methods are being used to examine the cure process [139,140,141,142,143], as well as non-linear methods [144,145]. The disbonding within an adhesive layer can be inspected by ultrasound wheel probes [146]. The focus in this work has been to find out if it is possible to monitor the curing process, to distinguish among different mixture ratios of the binder to the hardener, as well as to detect

disbonding with ACU inspection. Therefore, a sample was made that is shown in Figure 52.

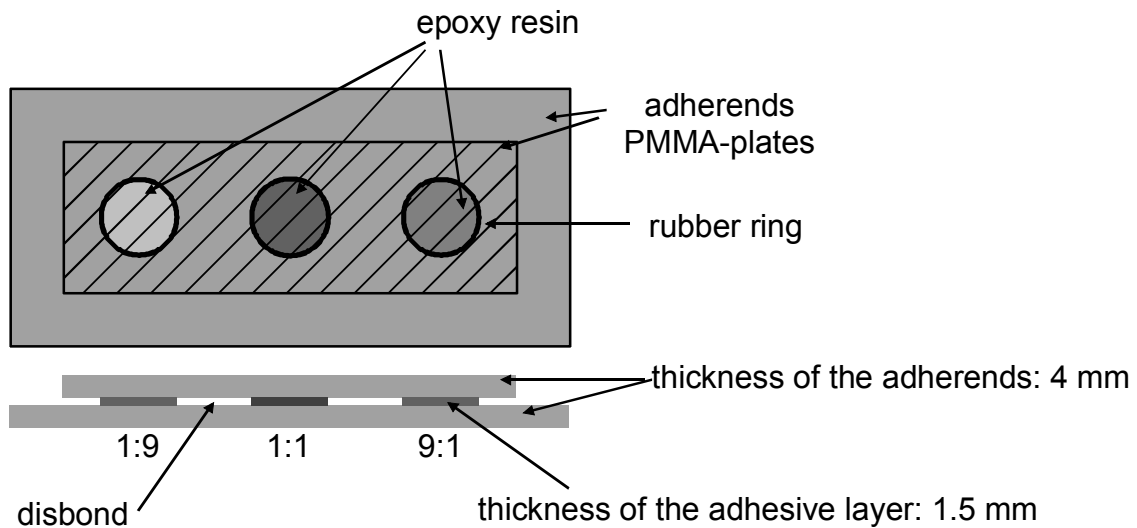


Figure 52: Sample used for inspection of the quality of adhesive joints. The ratio binder/hardener (epoxy resin) was 1:9, 1:1, and 9:1 (from left to right).

Two PMMA-plates were joined together with a two-component epoxy resin (UHU plus schnellfest) that was filled inside the three rubber rings. The rubber rings are used to achieve a constant thickness of the adhesive layer and to simulate artificial disbond between the rings. The optimal mixture ratio of both components of the epoxy resin is 1:1. In order to distinguish among different ratios of the two components, three different ratios 1:9, 1:1, and 9:1 were chosen (Figure 52). During the curing process, a line scan across all three rings was performed after certain times. The change of amplitude is shown in Figure 53. Immediately after mixing the two components together, the amplitudes of the ultrasound signals transmitted through the adhesives with the ratios 1:9 and 9:1 are higher than through the resin with the mixing ratio of 1:1 (up to three minutes). After five minutes, the situation changes and the transmitted amplitudes through the resin with the ratio 1:1 are higher than through the others. Also at the beginning of the curing process, the amplitudes at the boundaries are slightly higher than those in the middle of the resin-filled rings. Between 15 and 40 minutes (total curing time according to the manufacturer: 20 minutes), no significant change across the adhesive in the middle is seen. This behaviour was also found by recording of higher harmonics with a laser-vibrometer during the curing process [147].

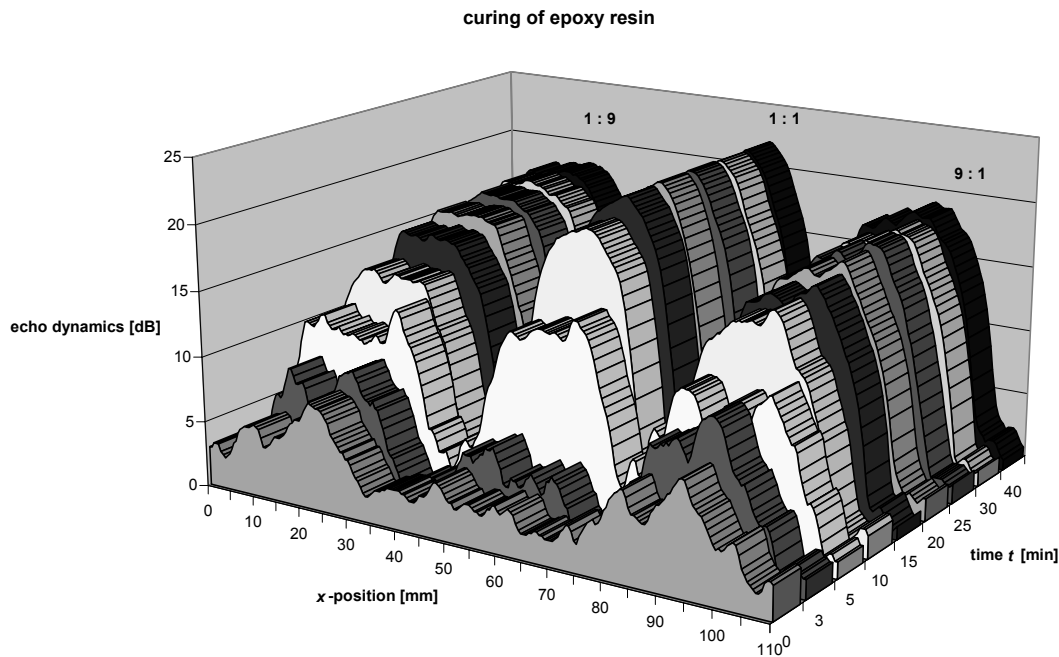


Figure 53: Changes of ultrasound amplitude during cure process of different mixture ratios of a two-component epoxy resin (1:9, 1:1, 9:1).

The amplitudes of the incorrectly mixed resins are still increasing for times greater than 15 minutes. Across the artificial disbonds between the rubber rings, the ultrasound amplitude is always below the bonded areas. The two primary reasons for the increase of amplitude during the curing process are

1. the increase of the sound velocity c and thereby the increase of the acoustical impedance Z and
2. the decrease of the sound attenuation.

Both changes occurred because of the increase of the stiffness caused by the cross-linking of the epoxy resin during the curing process. The measurement of the sample shown in Figure 52 equals the transmission of an incident beam through a plate described in section 2.5. In this case the surrounding medium is PMMA and the adhesive is the medium in-between. An increase of velocity c and therefore of Z reduces the reflection coefficient and as a result increases the transmission coefficient. At the end of the process, the acoustic impedance Z of the fully-cured epoxy resin (ratio 1:1) reaches a value of approximately $2.6 \cdot 10^{-6} \text{ kg/m}^2\text{s} - 3.6 \cdot 10^{-6} \text{ kg/m}^2\text{s}$ [41] and is close to the impedance of PMMA ($Z = 3.1 \cdot 10^{-6} \text{ kg/m}^2\text{s} - 3.3 \cdot 10^{-6} \text{ kg/m}^2\text{s}$ [41]). The resin that is not fully-cured (ratio 9:1) does not reach the stiffness of the fully-cured adhesive because the molecular chains are still able to move (relaxation processes) and are not totally

cross-linked because of an insufficient amount of hardener. As a result, the sound attenuation is greater and therefore the amplitude is lower. The binder (epoxy that becomes cross-linked) of the adhesive with the mixing ratio of 1:9 becomes fully cross-linked because there is only a small amount of the binder and much more hardener that cannot react. The decrease of the sound amplitude is caused by the hardener in this case.

6.4 Honeycomb sandwich structures

Honeycomb structures are suited for lightweight construction if high flexural rigidity, high geometrical moment of inertia, and low weight are needed. Components made out of this type of structures are used for such things as airplanes or helicopters. For ultrasound inspections, through-transmission mode with low frequency is appropriate because of the complicated structure with a lot of boundaries. Air-coupled inspections of impact damages [148], defects in the honeycomb core [149], and solar honeycomb panels [150] have been made previously. The focus in this work has been to detect disbond between skin and cells as well as to detect inclusions like resin agglomerations or water. For example, during the process of joining the surface layers with the honeycomb body, the cells might be filled with resin. If this happens, the stiffness properties of the structure are changed and the weight is increased. In a sample (thickness: 13 mm), there is an artificial disbond between the honeycomb body (honeycomb 3.2-64 T=12 mm) and the surface layer made out of CFRP (Figure 54 a). Also, several cells are filled with adhesive. On the ACU C-scan image, the disbonding (dark rectangle) and the filled honeycombs (bright area) are detectable (Figure 54 b) [151]. The additional boundary of the disbonding causes a decrease of the transmitted signal and therefore the not bonded area appears black on the image. In contrast, the filled cells (bright area) are related to an increase of signal in comparison to the empty ones due to the lack of air inside the cells.

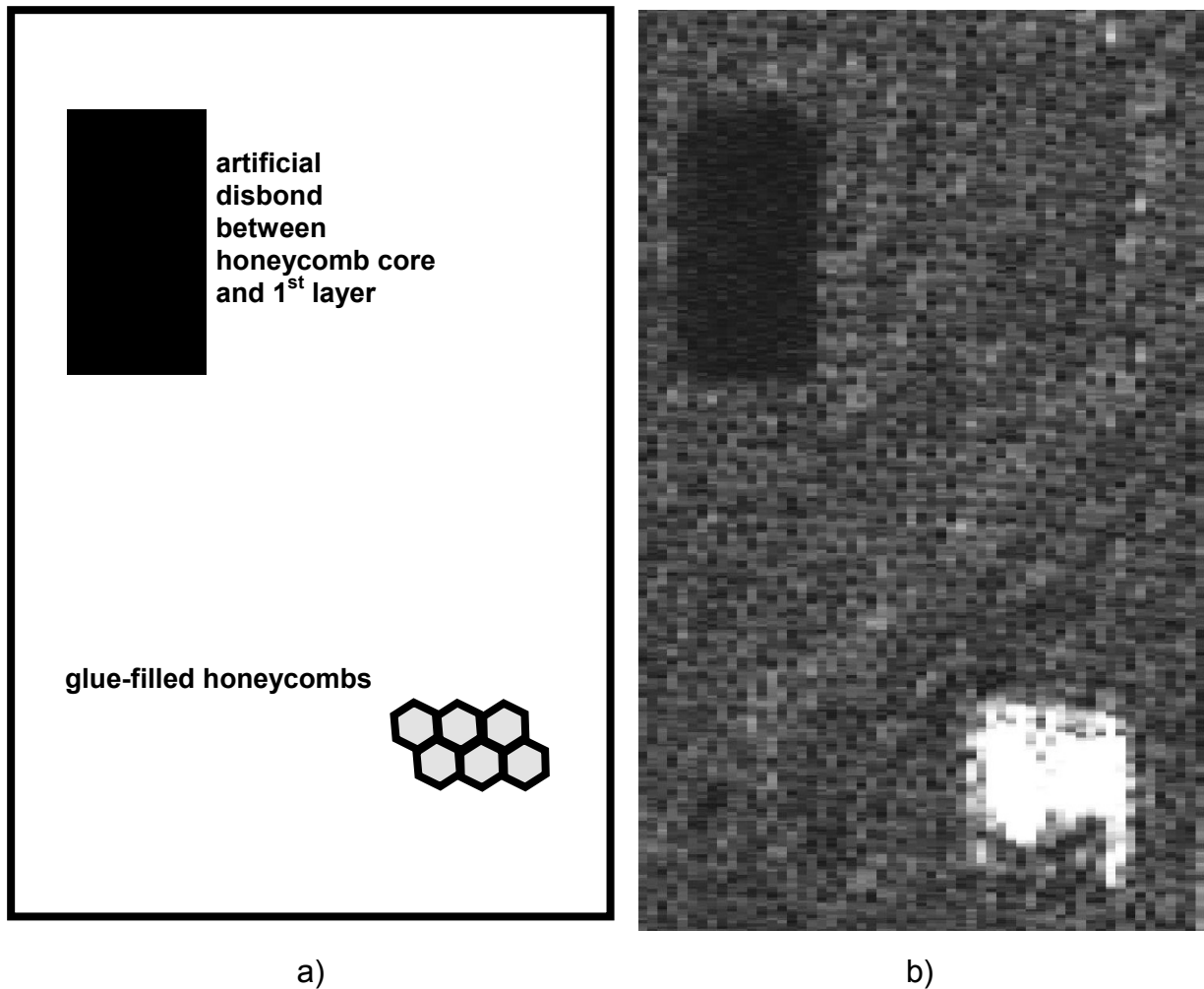


Figure 54: Drawing (a) and ACU C-scan image (b) of a honeycomb structure (sample size: 150 mm x 280 mm x 13 mm) with artificial disbond and with glue filled honeycombs (sample kindly provided by D. Keller; Euro-Composites S.A., Luxemburg).

Temperature differences between the inside and the outside of an airplane can cause condensation of air-humidity and moisture along the inner wall. This water may penetrate into the honeycomb core. Freezing water inside the cells can damage the honeycomb structure. Standard ultrasound inspection with water as a liquid coupling medium is not appropriate because of additional possible water penetration into the honeycomb core. The ACU C-scan presentation (Figure 55) shows the difference between water-filled (bright spots) and empty cells. Similar and comparable results on water-filled honeycomb structures were obtained with OLT [37].

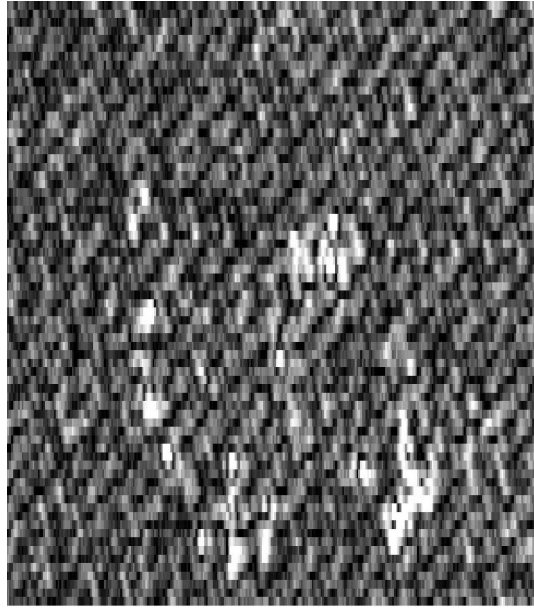


Figure 55: C-scan image (scanned area: 100 mm x 120 mm) of a honeycomb structure (GFRP- and CFRP-layers), some honeycombs are filled with water (bright spots).

6.5 Multi-Layer Ceramics

Ceramics are the best choice whenever material strength is required at high temperatures where metals and all other kinds of materials fail. The history of modern ceramics dates back to the 1960s when synthetic ceramics were developed with silicon as a primary ingredient in the form of Silicon Carbide (SiC) and Silicon Nitride (Si₃N₄). These materials have good physical, mechanical, and friction properties, as well as temperature resistance [152]. Also in the 1950s and in the 1960s, carbon fibre reinforced carbon (Carbon/Carbon, C/C) was developed in the United States and in the Soviet Union [153]. A combination of these two ceramics leads to a new class of materials called Carbon-Carbon Silicon Carbide (C/C-SiC or C/SiC). These are carbon fibre reinforced composites with a ceramic matrix, mostly silicon carbide. In 1988, major research was begun in Germany in the field of C/C-SiC [153]. This high performance and high temperature resistant material (up to 1800°C) offers many new applications due to both the reduced brittleness (caused by the embedded fibres) and the low density (1.8 – 2.0 g/cm³; depending on the porosity). The density is even lower than that of Aluminium (2.7 g/cm³). All these properties make C/C-SiC a candidate material for space technology (e.g. heat protecting components [154] or steering flaps of re-entry space vehicles [155]) or vehicle technology (e.g. break discs [156]). Therefore reliable non contact testing techniques are needed.

6.5.1 Monitoring the production process of C/C-SiC.

An optical image of the C/C-SiC material is displayed in the upper left of Figure 56 [157]. The material is black (carbon) with metallic reflections (silicon). With ACU, it is possible to monitor the production process steps without using water, which can be absorbed by the material.

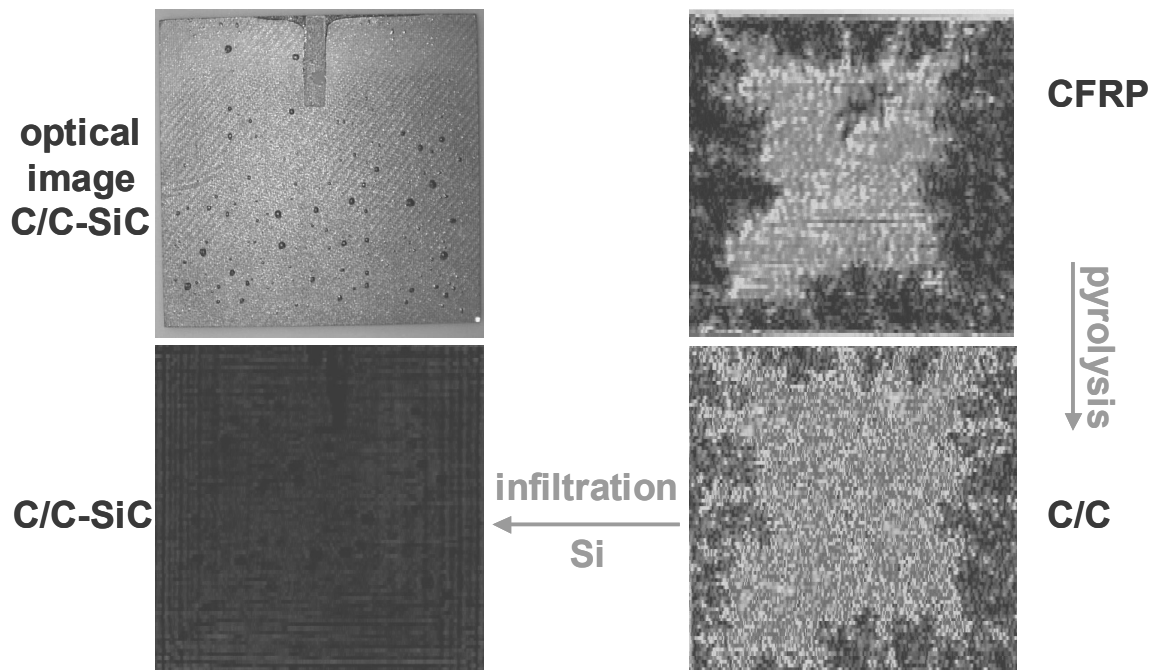


Figure 56: Monitoring the production process of fibre-reinforced ceramic (C/C-SiC) with ACU performed on one plate (from upper right image to lower left image; size of the sample: 300 mm x 300mm x 8 mm) (sample kindly provided by R. Aoki; DLR, Stuttgart).

Figure 56 illustrates various steps of the production process that need to be understood in order to produce defect-free components, which is a major point in modern quality assurance. The process called “Liquid Silicon Infiltration” (LSI) [158] starts with CFRP. In this first step, the carbon fibre structure (e.g. layers) is infiltrated with liquid precursor (resin) under pressure (5 – 20 bar) and at a temperature of 200°C in an autoclave and then cured. Because of combined imbuing and curing in a closed system, three-dimensional structures are easy to make. On the ACU C-scan presentation of CFRP (Figure 56, upper right image), differences in density are detected. During the following pyrolysis step in a Nitrogen atmosphere (to prevent the oxidation of Carbon), with no pressure and at a temperature of 900°C, the material is transferred into the C/C-phase because the resin is turned into carbon, hydrogen and nitrogen become NH₃. On the ACU C-scan image (Figure 56, lower right image), changes in density and in porosity

are seen between the CFRP-phase and the C/C-phase. C/C-ceramics have a very high sound attenuation level because of their high porosity. This result was expected because CFRP is converted into an amorphous carbon matrix with high capillarity and trans-laminar micro cracks. In the last step, liquid silicon is infiltrated into this porous material at 1550°C and under vacuum. Because of capillary attraction, cracks and holes are filled. In addition a chemical reaction takes place; carbon and silicon are transformed into silicon carbide (SiC). Surprisingly, after infiltration, the initially heterogeneous material is very homogeneous (Figure 56, lower left image).

6.5.2 Heterogeneous distribution of Si and SiC

What does a heterogeneous distribution of Si look like and can it be detected with ACU? An inadequate infiltration of Si into C/C is related to a heterogeneous stiffness of the material. Low SiC-content areas have a greater porosity and occur mainly in the centre and in thicker parts because Si is diffusing in from the surfaces. This situation is a potential source of defects. Figure 57 presents the result of a C/C-SiC ceramic sample with heterogeneous distribution of the Si content.

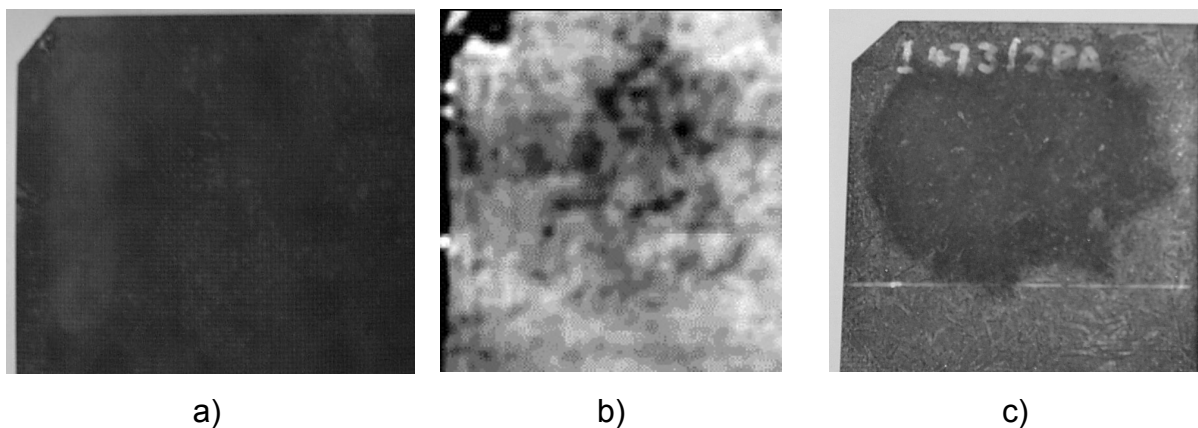


Figure 57: Detection of heterogeneous distribution of Si inside a C/C-SiC-sample (thickness: 6 mm); a) optical image of the front side (changes of Si-content not visible); b) ACU C-scan image (variations of Si-content are detected; scanned area: 120 mm x 120 mm); c) optical image of the rear side (changes of Si-content are visible) (sample kindly provided by B. Benitsch and R. Aoki; DLR, Stuttgart).

On the front surface (Figure 57 a), nothing can be seen by naked eye. But on the ACU C-scan presentation (Figure 57 b), the changes of density that are related to varying transmission and absorptions coefficients are detected. The poorly infiltrated area appears darker because of lower density so that a lower signal is transmitted because of

lower transmission and higher absorption coefficients. On the rear side, the area with lower Si-content is seen (Figure 57 c).

6.5.3 Delaminations

In addition to monitoring the production process, the structural integrity of the final product is a major topic of concern if safety-relevant applications are considered. Thus, it is important to detect defects during each step of the manufacturing process. Because carbon fibre reinforced ceramic consists of layers, delaminations can occur during the manufacturing process or later during use if silicon is not distributed homogeneously during the infiltration step (section 6.5.1). To prove the ability of ACU techniques to detect delaminations in all steps of the production process, three plates made of CFRP, C/C, and C/C-SiC, each with artificial delaminations open to the edge, were inspected. With water-coupling, these measurements would be difficult to perform because water would penetrate into the delaminations.

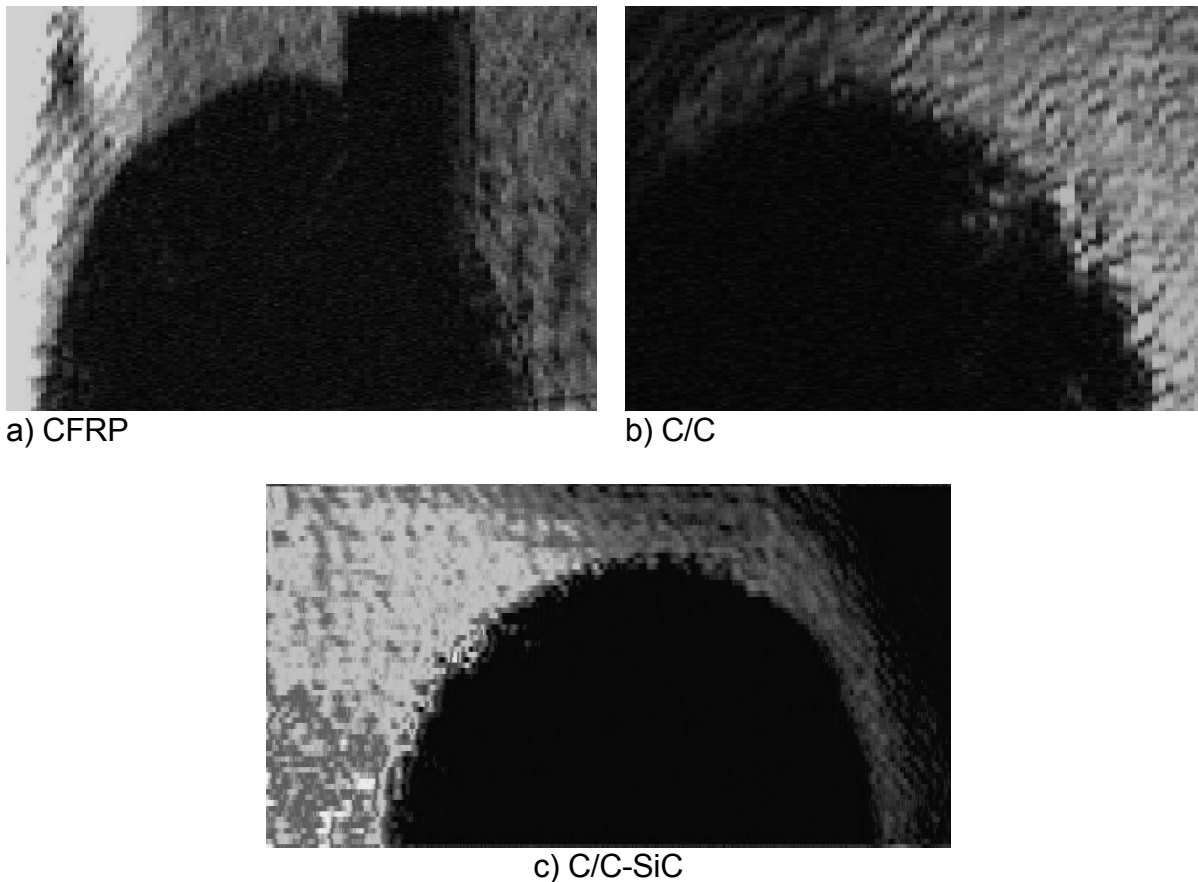


Figure 58: ACU C-scan presentations of artificial delaminations (dark areas) open to the edge; a) in CFRP; b) in C/C-phase; c) of a C/C-SiC ceramic (thickness of each of the three samples: 8 mm; scanned area: 295 mm x 135 mm) (samples kindly provided by B. Benitsch; DLR, Stuttgart).

Figure 58 a shows an ACU C-scan image of an artificial half-circle delamination in CFRP and an embedded rectangular foil. Also the delaminated areas of the samples made of C/C and C/C-SiC [129] (Figure 58 b, c) are seen. The black area in the upper right of the ACU C-scan image of the C/C-SiC sample is caused by the curvature of the sample. Thus, it is possible to inspect samples of all three manufacturing steps.

6.5.4 Disbond

During the infiltration step (section 6.5.1), it is possible to use silicon as “glue” so that the parts are joined together without any interface because the interface will become a homogeneous part of the material. This “in-situ” technique has its limitations if the component is too complicated in structure or too thick so that silicon is not absorbed well and disbond between joint interfaces may occur.

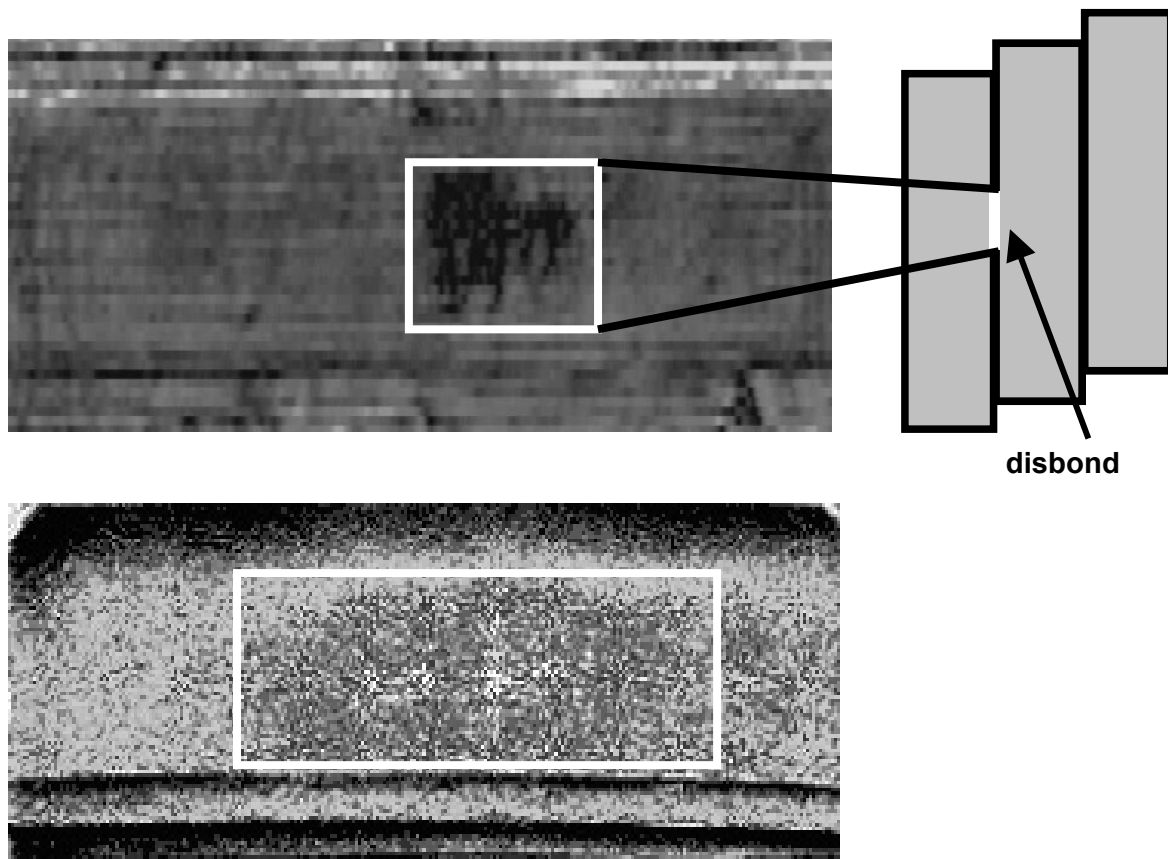


Figure 59: C/C-SiC ceramic sample with disbond (thickness of each plate: 8 mm; scanned area: 240 mm x 90 mm); ACU C-scan image (top); optical lockin thermography, phase image (0.06 Hz, bottom) (sample kindly provided by B. Benitsch; DLR, Stuttgart).

The sample (Figure 59) consists of three plates shifted with respect to each other before they were joined together with an artificially made delamination between two layers in the middle. The defect can be detected and seen in the middle of the ACU C-scan image (Figure 59 top, white rectangle). The thickness variations of the sample along the upper and lower edge are shown by bright and dark horizontal lines [129]. An OLT phase image (Figure 59 bottom; measurement kindly performed by A. Dillenz; IKP, University of Stuttgart) also displays the variation in thickness and the delamination (white rectangle). The size of the disbond appears much larger because the thermal wave image is the convolution of the true structure with the thermal wave while ultrasound is sensitive to local impedance variations.

6.6 Shape adaptive Structures – “Smart Structures”

Piezo ceramics are used not only to generate or to detect ultrasound waves, but also for shape adaptive structures (“smart structures”) which consist of piezo ceramics that are embedded into CFRP- or GFRP-materials. The piezo ceramic can be operated both as a sensor to monitor external stimuluses as well as a structural actuator: when voltage is applied, it changes its form along with that of the material around it, and therefore adjusts the geometry of the components to flexible needs [159]. These opportunities offer interesting new purposes in aerospace applications.

Current developments in the manufacture of shape adaptive helicopter rotor blades use piezo ceramics to torque blades. The piezo ceramics must to be adjusted to the upstream and downstream situations with respect to the air during each rotation while the helicopter flies forward [160]. Thus, aerodynamics are enhanced and the total vibration of a helicopter can be reduced to make it more comfortable for passengers and to save fuel [161]. Other developments for airplane applications, such as horizontal and vertical stabilizer or wing flaps, are used to optimise the lift so that airplanes take off faster and the noise level around airports can be reduced [161,162].

These structures also must be inspected with non-destructive testing techniques because piezo ceramic, which is very brittle, is embedded into fibre reinforced polymer material. Due to voltage, integrated wires, and electronics, it is not appropriate to measure such structures in a water bath. Therefore, ACU offers new possibilities.

6.6.1 Detection of delaminations and structures in shape adaptive components

The embedding of the piezo ceramic into a polymer laminate is a problem because two materials with different elastic properties are combined. Two defects that may occur are

- delaminations in the laminate itself and
- delaminations between the interface laminate/ceramic.

A sample (CFRP-laminate) in which four actuators are integrated is shown in Figure 60 a. To simulate such defects, two Teflon[®] sheets on top of each other were embedded first on top of an actuator (upper right circle; Figure 60 a) and second in the laminate itself (lower left circle; Figure 60 a).

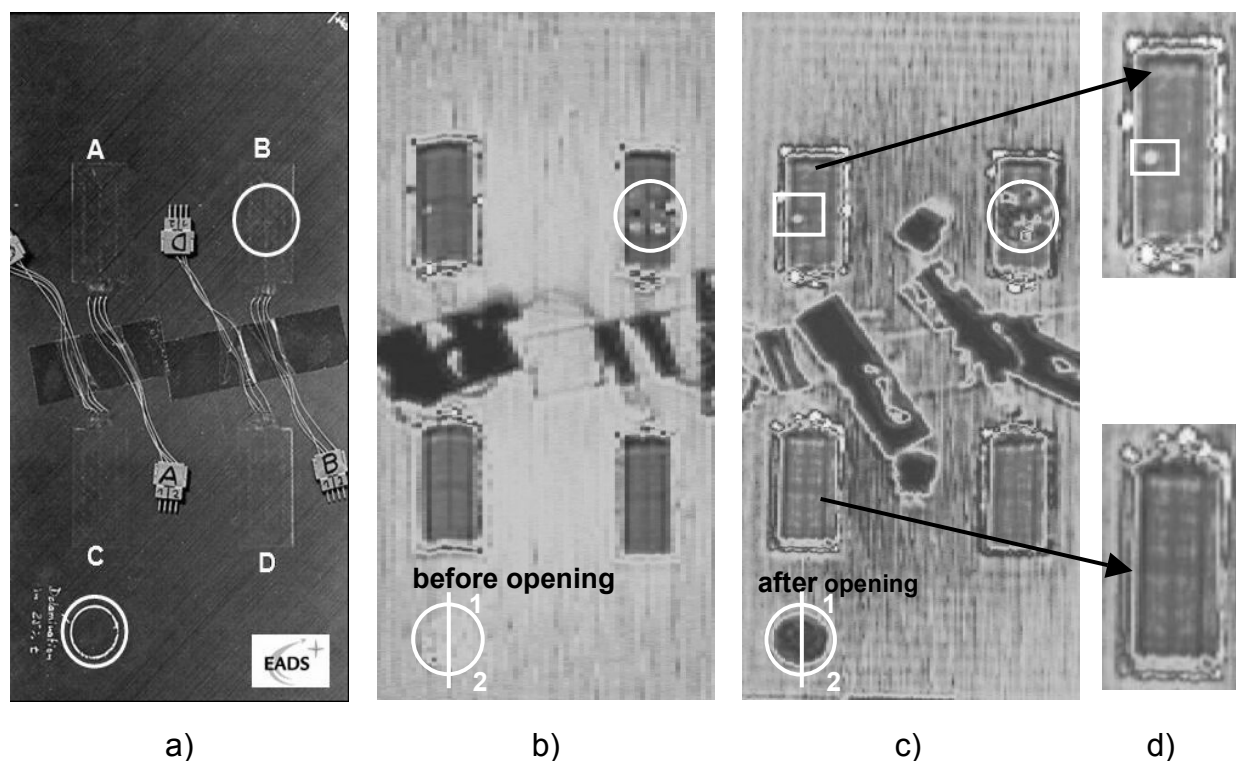


Figure 60: a) Optical image of shape adaptive structure (size: 152 mm x 300 mm x 2 mm) with 4 embedded actuators A to D [131]; b) ACU C-scan presentation of the structure (before loading and before delamination is opened, lower left corner; 1-2: echo dynamic curve across the delamination; Figure 61); c) ACU C-scan presentation of the structure (after loading which opened the delamination, lower left corner; 1-2: echo dynamic curve across the delamination; Figure 61); d) ACU C-scan images (scanned area: 75 mm x 40 mm) of two actuators. Variable black areas on the ACU C-scan presentations are caused by tape used to attach wires on the structure (sample kindly provided by J. Duerr; EADS Dornier GmbH, Friedrichshafen).

The ACU C-scan images (Figure 60 b, c) display the difference between the intact actuators (C, D) and the damaged (A, B) ones, as well as the artificial defect inside the laminate [131]. A close look at the ACU C-scan presentation of actuator A (Figure 60 d, top) shows damage caused by electrical overload. The enlarged C-scan image of actuator C (Figure 60 d, bottom) also shows the structure due to electrical contacts, a rectangular spacer made out of plastic, and resin agglomerations around the actuator [129]. The delamination in Figure 60 b (lower left) can barely be seen because the boundaries were sticking together. With optical lockin thermography, the same features are detected [163] except the damage caused by electrical overload. By bending the sample, this defect was opened and could be detected with a higher contrast to the surrounding material in the C-scan image (Figure 60 c). This aspect is proved in Figure 61 in which the echo dynamic curve of the transmitted signal across the defect is shown before and after the bending test (1-2: Figure 60 b and c).

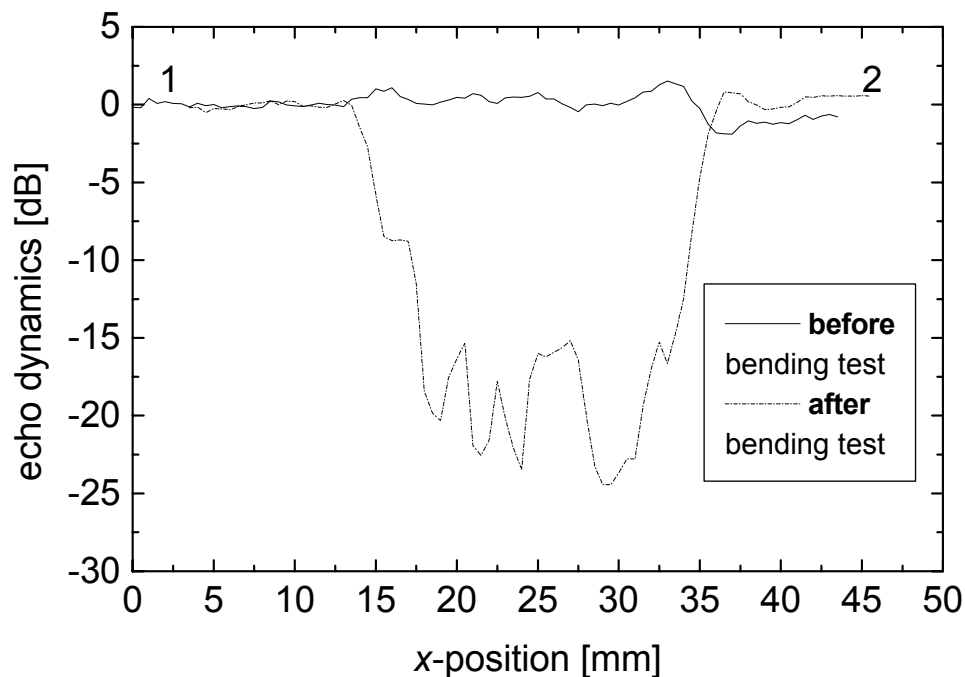


Figure 61: Echo-dynamic curve across an artificial delamination before and after bending test (1-2: Figure 60 b and c).

Before, the amplitudes across the imperfection are slightly higher than the amplitudes at the surrounding because in this area fibres are replaced by foil. Additionally, at the boundaries there are two peaks in amplitude. This slight increase may be due to a higher transmission coefficient (section 2.5) because of a specific d/λ -ratio of the two sticking together foils. After putting load on the laminate, there is an amplitude decrease by up to 25 dB due to impedance mismatch of the opened delamination. This

result confirms the opportunity to monitor load-induced changes in defects. The major disadvantage of the transmission arrangement is that access from both sides of the component is needed. This disadvantage is avoided if the integrated actuator itself is used as transmitter (Figure 62).

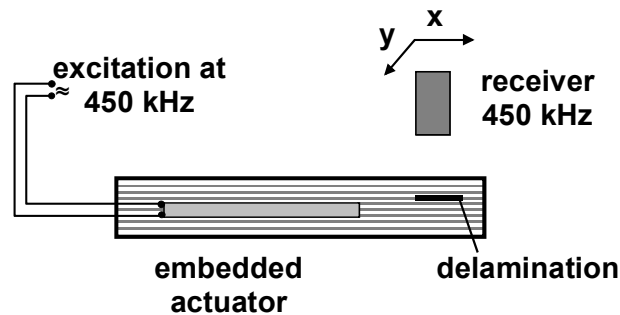


Figure 62: Embedded actuator used as transmitter for ACU inspection.

For comparison, the artificial delamination in the CFRP-laminate (Figure 60 a) was first measured in ACU transmission mode (Figure 63 a). Afterwards, the nearby actuator was operated as transmitter (driven by 450 kHz) to match the narrow-band receiver. The delamination is seen (Figure 63 b; black area) because waves do not propagate across the defect due to impedance mismatch between the laminate and the imperfection [164].

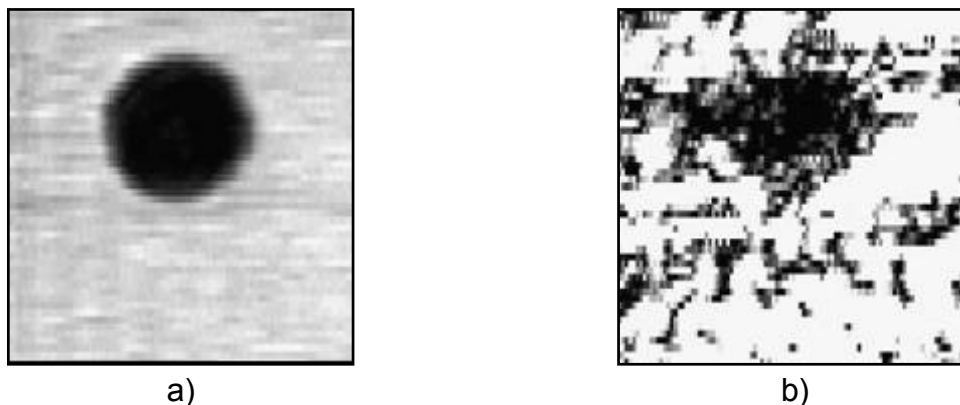


Figure 63: a) ACU C-scan image: artificial delamination measured in transmission mode; b) Scan image performed on the same delamination using the nearby piezo ceramic as transmitter (Figure 60 a); scanned area: 75 mm x 40 mm.

This technique can be applied not only for monitoring artificial delaminations but also for inspection of defects caused by overload during use. The defect occurred on top of an actuator embedded in a unidirectional GFRP-laminate (Figure 64 a). The delamination is detected on the ACU C-scan image measured in through-transmission (Figure 64 b), as well as on the image performed with the actuator used as transmitter (Figure

64 c). The image is not as sharp as the one performed in through-transmission because the waves are travelling from the embedded actuator to the delamination and the excitation therefore is not focused in one spot.

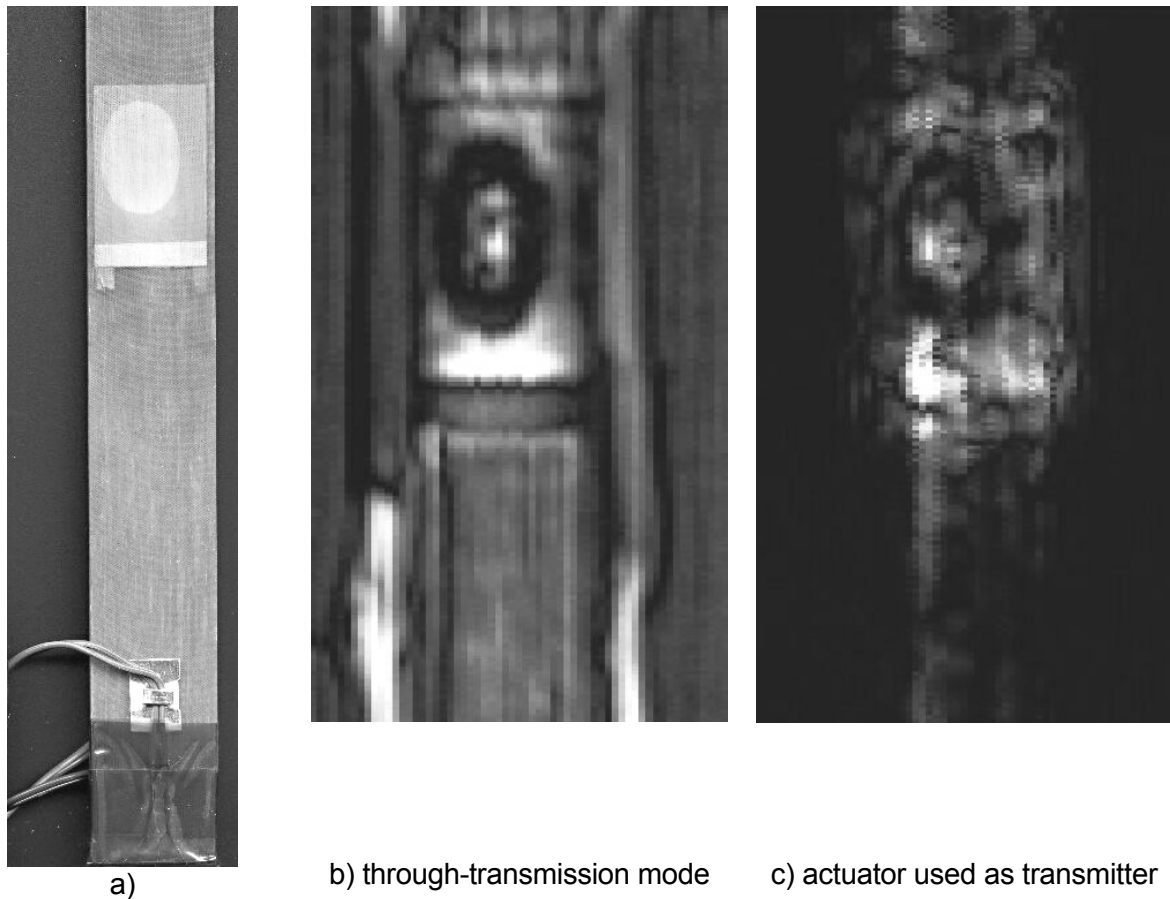
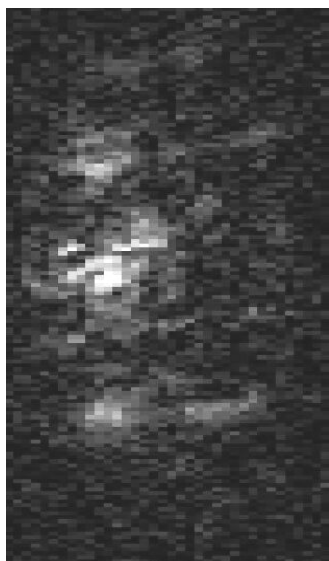
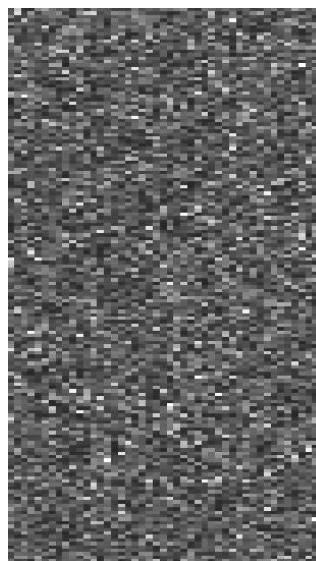


Figure 64: a) Optical image of shape adaptive structure (GFRP) with a delamination on top of an actuator caused by load; b) ACU C-scan image of the structure (through-transmission mode); c) scan image of the structure (scanned area: 28 mm x 60 mm) (sample kindly provided by M. Flock; Institut fuer Flugzeugbau, University of Stuttgart).

These two images display either the entire structure (the piezo ceramic and the delamination) or the delamination and the piezo ceramic. The more interesting question is whether this defect can also be selectively detected with non-linearity. To test the idea, the piezo ceramic was driven by 225 kHz, which has the receiving frequency of 450 kHz as a higher harmonic. On the 2nd harmonic image (Figure 65 a), the defect shows up selectively. Around the defect, there is only noise, while the delamination produces higher harmonics. Also, higher harmonics caused by the poorly-embedded actuator are recorded.



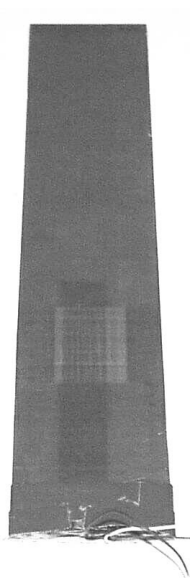
2nd harmonic image:
excitation frequency 225 kHz;
receiving frequency 450 kHz
a)



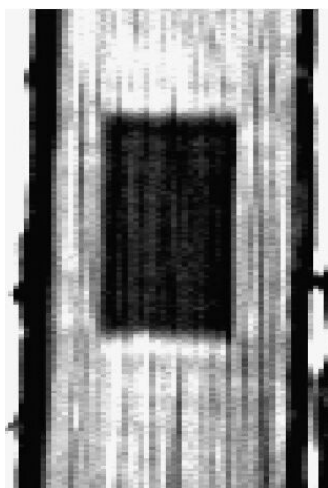
no higher harmonic:
excitation frequency 320 kHz;
receiving frequency 450 kHz
b)

Figure 65: Detection of higher harmonics on a shape adaptive structure with delamination and with not-well-embedded actuator; a) 2nd harmonic image, b) image with excitation frequency of 320 kHz (scanned area: 28 mm x 60 mm).

For further verifications of the defect-selective character of non-linear ACU inspection, a defect free GFRP-structure (Figure 66 a, b) was inspected in the same way.

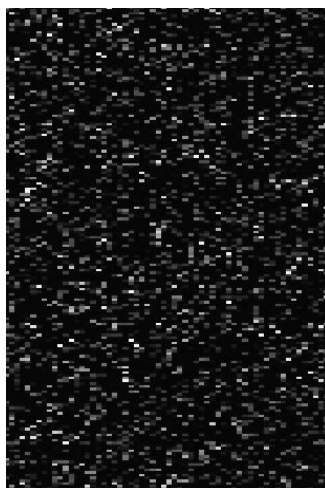


a)



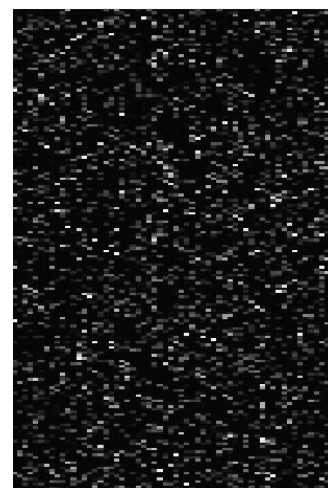
through-transmission mode

b)



2nd harmonic image:
excitation frequency 225 kHz; receiving frequency 450 kHz

c)



no higher harmonic:
excitation frequency 320 kHz; receiving frequency 450 kHz

d)

Figure 66: Reference inspection of a defect-free shape adaptive structure; a) optical image, b) ACU C-scan image, c) 2nd harmonic image, d) ACU image with excitation frequency of 320 kHz (scanned area: 50 mm x 80 mm).

For comparison, the same sample was inspected with a driving frequency of 320 kHz (close to the maximum sensitivity at 450 kHz, and no higher harmonic at 450 kHz). The image (Figure 65 b) displays only noise [164]. Thus, this result is indicating that the overtone is involved in image generation and not the fundamental frequency.

Because no harmonics were found (Figure 66 c, d), the defect-selective character of non-linearity is confirmed [164].

6.6.2 *Detection of cracks in shape adaptive structures*

As mentioned above, it is difficult to embed actuators into the laminate. The brittle piezo ceramic may break because of slight variations in roughness of the two layers between which it is fixed [165]. The embedded actuator can also be used to monitor cracks in the actuator itself. Measurements in water bath are reported in literature [166].

The air-coupled system provides the advantage that the shape adaptive structure does not need to be removed from a component in order to be measured in a water bath. The samples are GFRP-laminates (0° and 90° - fibre orientation) [167]. On the x-ray image (Figure 67 a), cracks of a defective piezo ceramic are shown. The scan (Figure 67 b) across this broken actuator, in which the actuator is operated by 450 kHz, displays only the connected part of it. The cracks prevent the entire actuator from vibrating. In comparison, on the C-scan image (Figure 67 c) performed in through-transmission mode, the cracks cannot be seen. The differences in contrast across the piezo ceramic are caused by heating wires being allowed to change the embedding conditions. In comparison, the entire crack-free actuator (x-ray image in Figure 68 a) can be seen on the scan image in which the actuator is used as a transmitter because the complete ceramic oscillates (Figure 68 b). On the image performed in through-transmission mode (Figure 68 c), the piezo ceramic looks much more homogeneous because no heating wires are embedded in this sample.

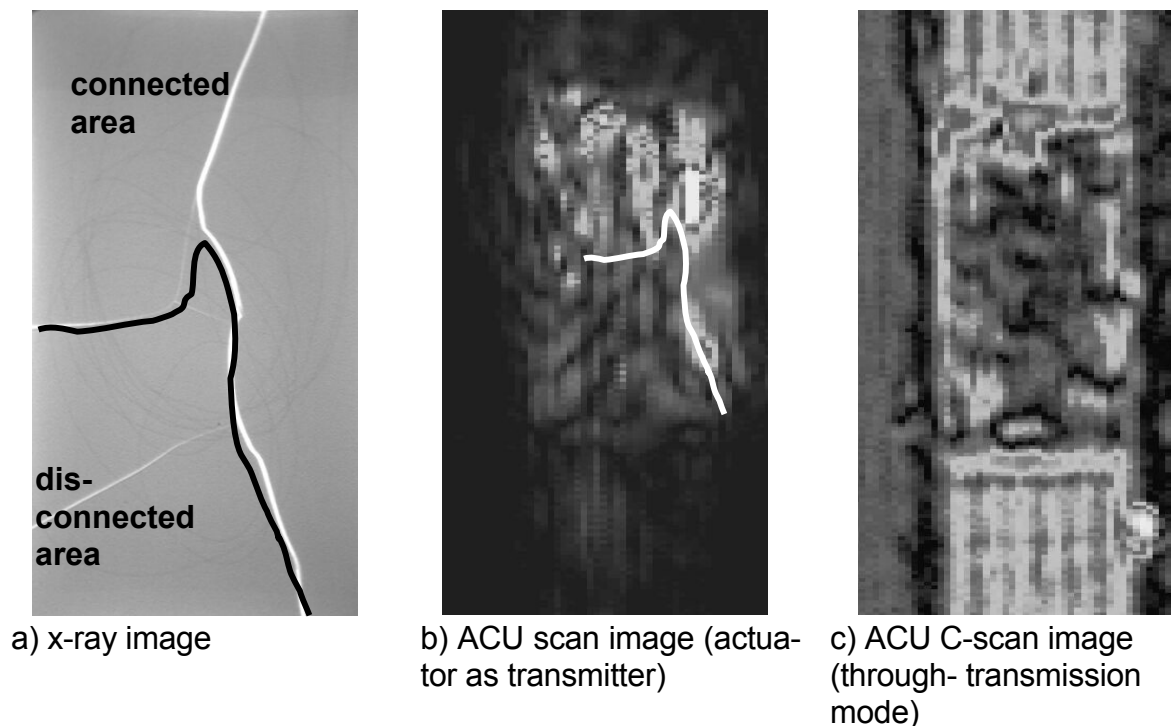


Figure 67: Monitoring of a defect shape adaptive structure using various kinds of inspection techniques [167] (scanned area: 30 mm x 60 mm).

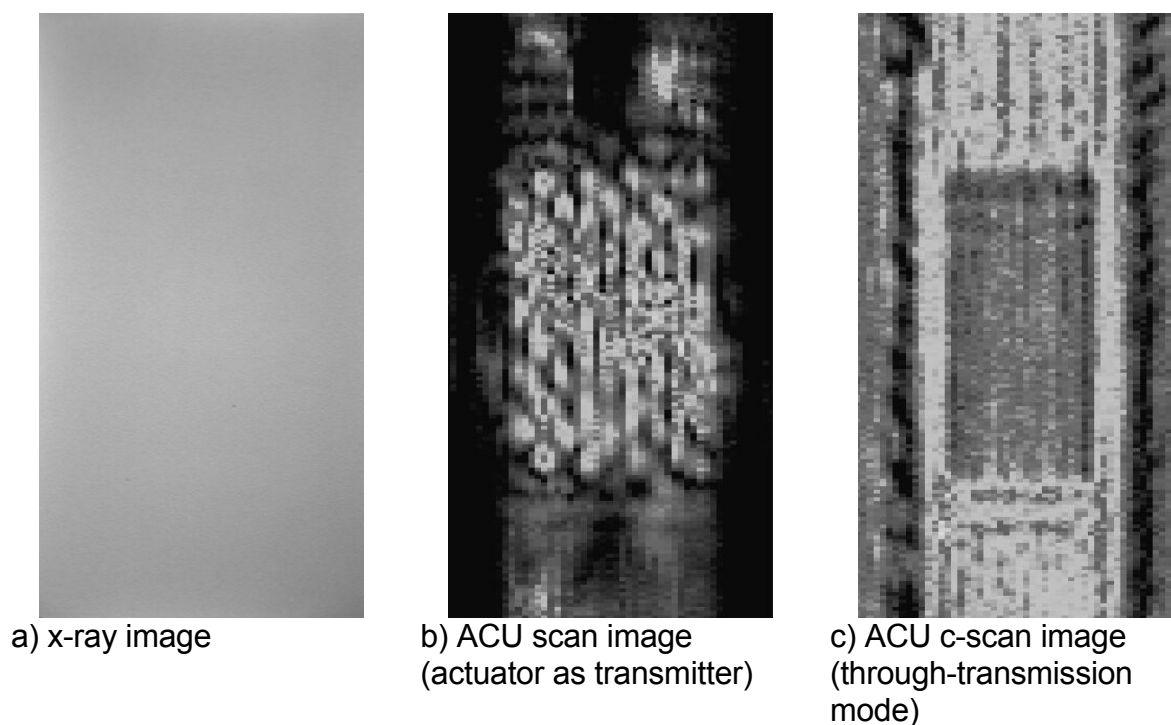


Figure 68: Reference measurement to Figure 67: Monitoring of an intact shape adaptive structure using various kinds of inspection techniques (scanned area: 30 mm x 60 mm) [167].

With increasing temperature the difference between the connected and disconnected parts becomes clearer because of increasing damping of the heated thermoplastic surrounding. As a result, the waves do not propagate further.

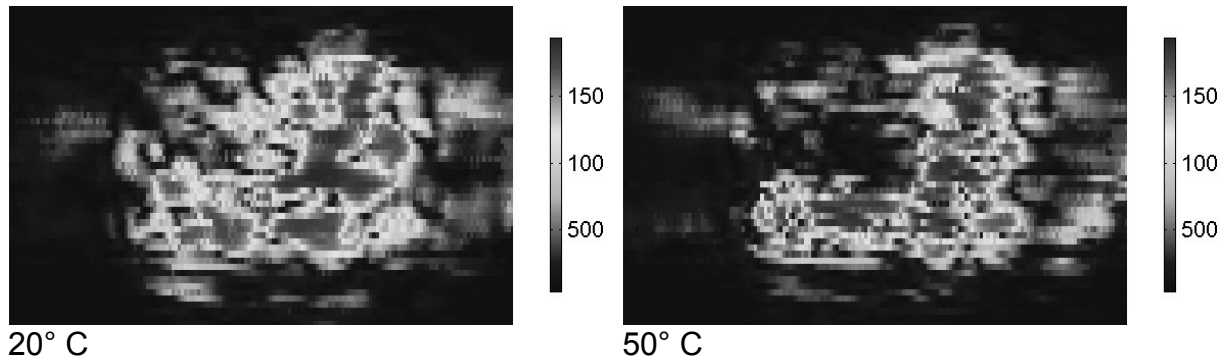


Figure 69: Monitoring of a defective shape adaptive structure during heating of the surrounding (ACU images; scanned area: 30 mm x 60 mm) [167].

7 Conclusions and Implications

7.1 Conclusions

This study demonstrates the ability of linear and non-linear ACU inspection as a new NDT tool for quality assurance. The scope of this thesis is to establish this novel non-contact technique into a non-destructive testing laboratory as well as to investigate both the potential and the limitations for industrial applications. Therefore, a variety of different materials and components were inspected and the results were compared with those of other established NDT techniques. These include:

- The results obtained on different kinds of materials would have been more difficult or even impossible to achieve in a water tank.
- Wood can be inspected and the annual structure, artificially made holes, hidden invisible knots, and the lack of glue in the interface between wood and the surface layer in wood veneer samples can be found. All features were clearly detected. These measurements are of great interest for the wood industry because they are performed by contact-free scanning across surfaces.
- CFRP is increasingly replacing metals, especially in aerospace applications. The wide potential of ACU techniques was proved by inspection of impact damages and delaminations between layers, which are the two most common defects of this new material. Also the ability to inspect repaired airplane components was successfully demonstrated. The results achieved with linear and non-linear ACU were compared with other techniques like ULT, OLT, optical microscopy, LSM, and non-linear vibrometry. All features found with these other techniques were also found either by linear or non-linear air-coupled techniques, or by both. Some additional information about the defects, like the core of impact damage, were found with ULT and with linear ACU, but not with the non-linear ACU and not with non-linear vibrometry. Linear ACU also allows the extent of defects to be measured, which is not possible with non-linear methods and only feasible with OLT with a reference and if the thermal conductivity is considered. In addi-

tion, in order to get an idea of the extent of a defect with OLT, two measurements from both sides of the sample are needed, while in through-transmission ultrasound technique, one measurement is sufficient. An artificially embedded foil was detected with linear air-couple ultrasound but not with non-linear methods. Non-linear ACU selectively detects impact damages and delaminations in some cases.

- Honeycomb sandwich structures are suited for lightweight construction. The focus in this work has been to detect disbond between skin and cells as well as to detect inclusions like resin agglomerations or water. All these three faults are detectable with linear ACU and this technique can compete with OLT which detects the same features.
- The monitoring of the curing process of epoxy resin, the ability to distinguish among different mixing ratios, and to detect disbonding is important to know for industry because more and more joining is done by gluing. In this case, ACU is a suitable technique that does not have an effect on the curing process.
- C/C-SiC is a newly developed and very promising material for high temperature resistant and safety-relevant components. Because major efforts are going on in characterizing this high potential material, improved testing techniques are also needed. The entire manufacturing process can be monitored which helps to understand the process. Also, defects like delaminations open to the edge can be identified in the CFRP, in the C/C, and in the C/C-SiC step. In addition to delaminations, heterogenic contribution of silicon content and disbonding of joined layers are also found. Other NDT techniques like OLT offer the same possibilities, but defect-selective methods like ULT and non-linear vibrometry are difficult to perform in the C/C-step because of the high output power of the sonotrode that must be clamped to the sample. Thus, there is a risk that the very brittle material (carbon) may become damaged.
- An interesting and exiting application for linear and non-linear ACU is monitoring of shape adaptive structures. In through-transmission mode, the structural integrity can be inspected in order to identify the position of actuators, delaminations on top of piezo-actuators, and in the laminate, as well as damages caused by

electrical overload. Also measurements at an artificially made delamination before and after bending tests prove the ability of ACU to monitor changes in defects during the usage of a component. More advanced inspections can be performed by using the embedded actuator itself as excitation source and to receive the signals with the receiver head. Thus, it is possible to detect broken ceramic actuators, delaminations on top of the piezo ceramic, and nearby delaminations. The next step in such monitoring is non-linear ultrasound to detect defects selectively. In all the cases mentioned above, the air-coupled technique is able to compete with other NDT methods which achieve equal results.

What general conclusions can be drawn out of the successfully obtained results? Are major demands of modern quality assurance (section 1.1) fulfilled and what are the limitations? Answers to these questions are summarized in the following table:

demands of modern quality assurance	air-coupled ultrasound inspection technique	
	linear	non-linear
knowledge of limitations	through-transmission technique, displays the structure and possible defects access from both sides of the sample is needed	CAN threshold for non-linearity needs to be passed
no effect of the inspection method on the result (disturbance)	remote and non-contact method	remote but not a non-contact method if an excitation sourced is attached
comparable to other inspection techniques	can easily compete with other NDT methods	after further research it can easily compete with other NDT methods
cost-effective methods	in comparison to other techniques the investment costs for equipment are lower	in comparison to non-linear vibrometry the investment costs are lower

FMEA: requires the ability and a possibility to evaluate the probability of detection	ability to detect all sorts of hidden defects in all kinds of materials and components	ability to detect such kinds of defects which respond non-linear to an excitation (e.g. clapping boundary)
SPC: collecting dates for process control	evaluations of size of defects and amount of defects	evaluation of size of defects and amount of defects is more difficult than in linear mode
easy to understand, no additional sources of faults because of lack of knowledge or incorrect calculations	easy to perform like standard ultrasound inspection but without liquid easy to handle and to understand because only changes of amplitude are considered, displayed with the help of a colour bar, and no further calculations are needed	fast, defect-selective method certain knowledge is needed to perform measurements
fully understood processes	monitoring production processes is possible	monitoring production processes is conceivable
cross-linked feedback loops of quality assurance	can be implemented into the loop	can be implemented into the loop
monitoring of existing defects	monitoring changes of defects is possible	monitoring changes of defects is possible
monitoring along the entire life-cycle of a product	can be used as a tool for quality assurance at all steps of the life-cycle of a product especially during manufacturing and in after sales service	can be used as a tool for quality assurance at all steps of the life-cycle of a product especially during manufacturing and in after sales service

Table 10: Comparison of demands of modern quality assurance with the potentials of linear and non-linear ACU inspection technique

7.2 Implications

Detailed research work has been conducted that presents various uses of ACU techniques. Many of these remain as interesting topics for further study. Linear ACU inspection has been restricted to the evaluation of changes of amplitudes caused by inclusions. Phase analyses would offer an increased sensitivity and would enhance the probability of detection as well as offer new possibilities to monitor growth of defects. Further investigations are also conceivable in the field of non-destructive testing of metals and of food.

In addition, this study demonstrates the first very promising results obtained with non-linear ACU. The measurements, however, are performed partly by glued-on actuators and the excitation amplitude is sometimes not high enough to pass the non-linear threshold. These limitations can be overcome in future by using a piezo stack clamped to the sample or by using two different transducers, a transmitter with a certain narrow band frequency (fundamental frequency) and a receiver with a centre frequency tuned to an overtone of the fundamental frequency. Nonetheless, the results obtained with linear and non-linear techniques are very encouraging and are important steps to overcome the lack of knowledge of this new promising method.

This thesis describes in detail the importance of a matching layer for air-coupled ultrasound transducers (section 2.6 and section 5.2). It suggests that if a matching layer is used for the transducer/air boundary, then one should also be used for the air/sample boundary for an additional reduction of losses. Using this idea, measurements were first performed with a PMMA-sample onto which textile adhesive tape strips were fixed on the surface. This kind of tape was chosen because it is expected to have an impedance value that is between the value for air and for PMMA. One strip was fixed on the front side (Figure 70; left), another one on the upper side and also one on the rear side (Figure 70; middle). The last strip was fixed to the rear side (Figure 70; right). The echo dynamic curve across the sample is shown in Figure 70 bottom. By using one strip, either on the rear or on the front side, the transmitted signal increases by around 10 dB to 11 dB. The doubled-sided arrangement even increases the sound amplitude up to 14 dB. These results are promising and can be the basis for further investigation in this direction. This may also be an interesting solution for measurements of highly sound-absorbent samples and for metals, which have higher impedance than plastics. These results can also be of interest for other non-destructive testing techniques such as ultrasound lockin thermography (ULT) or for measuring the transfer function of waves. Both techniques must couple elastic waves into a sample.

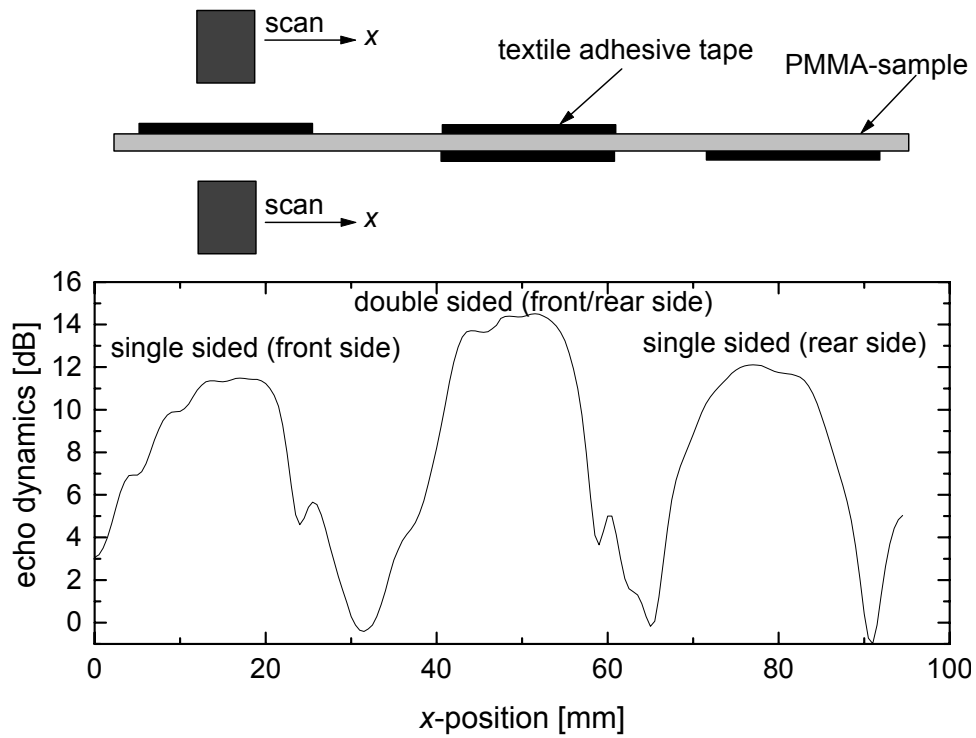


Figure 70: Measurements with textile adhesive tape strips used as matching layer at the air/sample boundary to reduce the losses. The experimental set-up is shown on the top of this figure. The echo dynamic curve of the transmitted ultrasound signal is shown on the bottom of this figure.

8 References

- [1] Weckenmann, A., *Qualitaetsmanagement I, 5. Fachsemester, Wintersemester*, Lehrstuhl Qualitaetsmanagement und Fertigungsmesstechnik, Universitaet Erlangen-Nuernberg, (1995), p. 2-2.
- [2] Richter, H. U., *Chronik der Zerstoerungsfreien Materialpruefung*, DGZfP, Deutsche Gesellschaft fuer Zerstoerungsfreie Pruefung e.V., Verl. fuer Schweissen und verwandte Verfahren, Berlin, (1999).
- [3] N. N., *Richtlinie des Rates vom 25.07.1985 zur Angleichung der Rechts- und Verwaltungsvorschriften der Mitgliedstaaten ueber die Haftung fuer fehlerhafte Produkte*, (85/ 374/ EWG), (1985).
- [4] N. N., *Gesetz ueber die Haftung fuer fehlerhafte Produkte*, Gesetz vom 15.12.1989 (BGBl. I S. 2198), Rechtsvorschriften Bundesrepublik Deutschland, zuletzt geaendert durch Gesetz vom 19.7.2002 (BGBl. I S. 2674) m.W.v. 1.8.2002.
- [5] Griffin, P., *What is Quality Assurance?*, <http://quality.co.uk>, (1995).
- [6] N. N., *DIN EN ISO 9000, Qualitaetsmanagementsysteme - Grundlagen und Begriffe (ISO 9000:2000), Dreisprachige Fassung EN ISO 9000, Ausgabe: 2000-12*, Deutsches Institut fuer Normung e.V., Beuth Verlag GmbH, Berlin, (2000).
- [7] N. N., *DIN EN ISO 9001, Qualitaetsmanagementsysteme - Anforderungen (ISO 9001:2000-09), Dreisprachige Fassung EN ISO 9001, Ausgabe: 2000-12*, Deutsches Institut fuer Normung e.V., Beuth Verlag GmbH, Berlin, (2000).
- [8] Jahn, H., "Erzeugnisqualitaet, die logische Folge von Arbeitsqualitaet", *VDI-Z*, 130, (1988), pp. 4-12.
- [9] N. N., *DIN EN ISO 9004, Qualitaetsmanagementsysteme - Leitfaden zur Leistungsverbesserung (ISO 9004:2000), Dreisprachige Fassung EN ISO 9004:2000, Ausgabe:2000-12*, Deutsches Institut fuer Normung e.V., Beuth Verlag GmbH, Berlin, (2000).
- [10] Busse, G., *Zerstoerungsfreie Pruefung*, Vorlesungsskript, Universitaet Stuttgart, 2002.

- [11] Deming, W. E., *Out of the Crisis*, Massachusetts Institute of Technology, Cambridge, USA, (1988).
- [12] Creath, K., *Digital Speckle-Pattern Interferometry*, Ph.D.-thesis, Optical Sciences Center, University of Arizona, Tucson, AZ, (1985).
- [13] Ritter, S., *Speckle-Pattern-Interferometrie und ihre Anwendungen in der zerstörungsfreien Pruefung*, Diploma, Fakultät 13, Universität Stuttgart, (1994).
- [14] Schubach, H. R., Ettemeyer, A., "Investigations on Aluminum Alloys with a 3D-ESPI-System", *Dr. Ettemeyer Application Report*, No. 01-97, (1997).
- [15] Hung, Y. Y., Taylor, C. E., "Measurements of slopes of structural deflections by speckle-shearing interferometry", *Experimental Mechanics*, 14, 7, (1974), p. 281.
- [16] Eisenberg, R. L., *Radiology: An illustrated history*, St. Louis, Mosby Year Book, (1991).
- [17] Roentgen, W. C., "Ueber eine neue Art von Strahlen", 1st announcement, December 1895, (Sitzungsbericht der Wuerzburger Physikalisch-Medizinischen Gesellschaft 1895), *Annalen der Physik*, 64, (1898), pp. 1-37.
- [18] Glocker, R., *Materialpruefung mit Roentgenstrahlen*, Springer Verlag, Berlin, (1971).
- [19] Stegmann, D., *Zerstörungsfreie Pruefverfahren, Radiografie und Radioskopie*, B. G. Teubner Verlag, Stuttgart, (1995).
- [20] Compton, A. H., Allison, S. K., *X-Rays in Theory and Experiment*, D. van Nostrand Company Inc., New York, (1949).
- [21] Hentschel, M. P., Hosemann, R., Lange, A., Uther, B., Bruechner, R., "Roentgenkleinwinkelbrechung an Metalldraehten, Glasfaeden und hartelastischem Polypropylen", *Acta Crystallographica*, A 43, (1987), pp. 506-513.
- [22] Zoughi, R., Ganchev, S., "Microwave non-destructive evaluation, state-of-the-art review", Austin, NTIAC, (1995).
- [23] Yeh, C., Zoughi, R., "Microwave detection of finite surface cracks in metals using rectangular waveguide sensors", *Research in Non-destructive Evaluation*, Vol. 6, No. 1, (1994), pp.35-55.
- [24] Diener, L., "Microwave near-field imaging with open-ended waveguide – comparison with other techniques of non-destructive testing", *Research in Non-Destructive Evaluation*, 7, 2/3, (1995), pp. 137-152.

- [25] Diener, L., Busse, G. "Non-destructive quality and process control in injection moulding polymer manufacture with microwaves", *7th Intern. Symposium on Non-Destructive Characterization of Materials*, 19-23.06.1995, Prague, (1996), 665-670.
- [26] Pfeifer, T., *Qualitätsmanagement, Strategien – Methoden – Techniken*, C. Hanser Verlag, Muenchen, (1993).
- [27] Fourier, J., "Théorie du mouvement de la chaleur dans les corps solides", *1^{re} Partie, Mémoires de l'Académie des Sciences*, 4, (1824), pp. 185-555.
- [28] Busse, G., "Optoacoustic phase angle measurement for probing a metal", *Appl. Phys. Lett.*, 35, (1979), pp. 759-760.
- [29] Thomas, R. L., Pouch, J. J., Wong, Y. H., Favro, L. D., Kuo P. K., Rosencwaig, A., "Subsurface flaw detection in metals by photoacoustic microscopy", *J. Appl. Phys.*, Vol. 51, (1980), pp. 1152-1156.
- [30] Lehto, A., Jaarinen, J., Tiusanen, T., Jokinen, M., Luukkala, M., "Amplitude and phase in thermal wave imaging", *Electr. Lett.*, Vol. 17, (1981), pp. 364-365.
- [31] Bennett, C. A. Jr., Patty, R. R., "Thermal wave interferometry: A potential application of the photoacoustic effect", *Appl. Opt.*, 21, (1982), pp. 49-54.
- [32] Beaudoin, J. L.; Mérienne, E.; Danjoux, R.; Egée, M.: Numerical system for infrared scanners and application to the subsurface control of materials by photothermal radiometry. In: *Infrared technology and applications SPIE 590*, (1985), pp. 287-292.
- [33] Rosencwaig, A., "Photoacoustic microscopy", *American Lab*, 11, (1979), pp. 725-727.
- [34] Carlomagno, G. M., Berardi, P. G., "Unsteady thermotopography in non-destructive testing", *Proc. 3rd Biannual Information Exchange*, Aug. 24-26. St. Louis, USA, (1976), pp. 33-39.
- [35] Kuo, P. K., Feng, Z. J., Ahmed T., Favro, L. D., Thomas, R. L., Hartikainen, J., "Parallel thermal wave imaging using a vector lock-in videotechnique", Hess, P., Pelzl, J. (Eds.), *Photoacoustic and Photothermal Phenomena*, Heidelberg, Springer Verlag, (1987), pp. 415-418.
- [36] Busse, G., Wu, D., Karpen, W., "Thermal wave imaging with phase sensitive modulated thermography", *J. Appl. Phys*, 71, (1992), pp. 3962-3965.

- [37] Rantala, J., Wu, D., Busse, G., "Amplitude Modulated Lock-In Vibrothermography for NDE of Polymers and Composites", *Research in Non-destructive Evaluation*, Vol. 7, (1996), pp. 215- 218.
- [38] Dillenz, A., Zweschper, T., Busse, G., "Elastic wave burst thermography for NDE of subsurface features", *Insight*, Vol. 42, No. 12, (2000), pp. 815-817.
- [39] Krohn, N., *Nichtlineares dynamisches Materialverhalten zur defektselektiven zerstörungsfreien Pruefung*, Ph.D.-thesis, Fakultät 13, Universität Stuttgart, (2002).
- [40] Sokoloff, S., "Zur Frage der Fortpflanzung ultraakustischer Schwingungen in verschiedenen Koerpern", *Elektr. Nachr.-Technik*, 6, (1929), pp. 454-461.
- [41] Krautkraemer, J., Krautkraemer, H., *Werkstoffpruefung mit Ultraschall*. 4. Verb. Aufl., Springer Verlag, Berlin, Heidelberg, New York, (1980).
- [42] Summerscales, J., *Non-destructive testing of fibre-reinforced plastics composites*, Elsevier Appl. Science, London and New York, (1987), I, (1990), II.
- [43] Luukkala, M., Merilainen, H., "Metal Plate Testing Using Airborne Ultrasound", *Ultrasonics*, Vol. 11, No. 5, (1973), pp. 201-208.
- [44] Dickson, J. K., "An Unconventional Method of Generation, Receiving and Coupling of Ultrasonic Waves for Testing Materials", Balteau-Sonotest, Milton Keynes, North Bucks, UK, (1977).
- [45] Dabirikhah, H., Turner, C. W., "Novel airborne ultrasound transducer", *Acoustical Imaging*, Vol. 21, edited by Jones, J. P., Plenum Press, New York, (1995), pp. 183-190.
- [46] Bhardwaj, M. C., Neeson, I., Stead, G., "Introduction to contact-free ultrasonic characterization and analysis of consolidated materials", invited presentation at the "Applications of non-destructive evaluation in powder metals seminar", Iowa State University, Ames, IA, USA, (2000).
- [47] Buckley, J., Loertscher, H. P., "Frequency considerations in air-coupled ultrasonic inspection", *BINDT Conference*, 16th September, (1999), pp. 405-410.
- [48] Zheng, Y., Maev, R., Solodov, I. Yu, "Nonlinear acoustic applications for material characterization: A review", *Can. J. of Physics*, Vol. 77, No. 12, (1999), pp. 927-967.
- [49] Morse, P. M., Ingard, K. U., *Theoretical Acoustics*, New York, McGraw-Hill, (1968).

- [50] Millner, R., *Ultraschalltechnik - Grundlagen und Anwendungen*, VEB Fachbuchverlag, Leipzig, (1987).
- [51] Ilshner, B., *Werkstoffwissenschaften*, 2. Auflage, Springer Verlag, Heidelberg, (1989).
- [52] Schatt, W., *Einfuehrung in die Wekstoffwissenschaft*, 6. Auflage, Huethig Verlag, Heidelberg, VEB Deutscher Verlag fuer Grundstoffindustrie, Leipzig, (1987).
- [53] Wedler, G., *Lehrbuch der physikalischen Chemie*, 3. duchgesehene Auflage, VCH-Verlag, Weinheim, (1987).
- [54] Sutilov, V. A., *Physik des Ultraschalls*, Wien, New York, Springer Verlag, (1984).
- [55] Rayleigh, Lord, *The theory of sound*, London, MacMillan u. Co., (1926); New York, Dover Publications, (1945).
- [56] Boyle, R. W., Lehmann, J. F., "The relation between the thickness of a partition in a medium and its reflection of sound waves by the ultrasonic method", *Phys. Rev.*, 2, Vol. 27, (1926), pp. 518-
- [57] Lohr J., *Moeglichkeiten zur Verbesserung von Luftultraschallsystemen*, PhD-thesis, Fachbereich 6, Verfahrenstechnik, Technischen Universitaet Berlin, (1998).
- [58] Gronauer, M., Fricke, J., "Acoustic Properties of Microporous SiO₂-Aerogel", *Acustica*, Vol. 59, (1986), pp. 177-180.
- [59] Yano, T., Tone, M., Fukumoto, A., "Range Finding and Surface Characterisation using High Frequency Air Transducers", *IEEE Trans. UFFC*, Vol. 34, No. 2, (1987), pp. 222-236.
- [60] Haller, M. I., Khuri-Yakub, B. T., "1-3 Composites for Ultrasonic Air Transducers", *IEEE Ultrasonics Symposium*, (1992), pp. 763-766.
- [61] Bhardwaj, M. C., "High Transduction Piezoelectric Transducers and Introduction of Non-Contact Analysis", Pre-print of a chapter submitted for the Encyclopaedia of Smart Materials, editor J. A. Harvey, Wiley, New York, (2000).
- [62] Stokes, G. G., "On the theories of the internal friction of fluids in motion, and of the equilibrium and motion of elastic solids", *Cambr. Trans. Phil. Soc*, Vol. 8, (1845), p. 287, papers I, (1880), pp. 75.

- [63] Kirchhoff, G., "Ueber den Einfluss der Waermeleitung in einem Gas auf die Schallbewegung", *Pogg. Ann. Phys.*, Bd. 209, (1868), pp. 177-193.
- [64] Biquard, P., "Les ondes ultrasonores", *Revue d'Acoustique*, Bd. 1, (1932), p. 93 and 315, Bd. 2, (1933), p. 288, Bd. 3, (1934), p. 104.
- [65] Stockes, G. G., "An examination of the possible effect of the radiation of heat on the propagation of sound", *Phil. Mag.*, (4), Vol. 1, (1851), pp. 3035-.
- [66] Kneser, H. O., "Schallabsorption in mehratomigen Gasen", *Ann. Phys.*, Leipzig, Bd. 16, (1933), pp. 337-343.
- [67] Kneser, H. O., "The interpretation of the anomalous sound absorption in air and oxygen in terms of molecular collisions", *J. Acoust. Soc. Amer.*, Vol. 5, (1933), pp. 122-128 .
- [68] Kneser, H. O., "Schallabsorption und -dispersion in Fluessigkeiten", *Ann. Phys.*, Leipzig, (5), Bd. 32, (1938), pp. 277-282.
- [69] Bermann, L., *Der Ultraschall und seine Anwendung in Wissenschaft und Technik*, 5. Auflage, (1949).
- [70] Birks, A. S., Green, R. E, McIntire, P., *Non-destructive Testing Handbook-Ultrasonic Testing*, Sec. Edit., Vol. 7, American Society for Non-Destructive Testing (ASNT), (1991).
- [71] Stanullo, J., *Anwendung digitaler Auswerteverfahren auf die Ultraschallpruefung von Polymerwerkstoffen*, PhD-thesis, Fakultae 13, Universitaet Stuttgart, (1999).
- [72] Banjavic, R. A., Zagzebski, J. A., "Ultrasonic pulse-echo beam width and axial response approximations for clinical broadband focused transducers", *Ultrasound in Med. Bio.*, 7, (1981), pp. 63-71.
- [73] Kuttruff, H., *Physik und Technik des Ultraschalls*, S. Hirzle Verlag, Stuttgart, (1988).
- [74] Born, M., Wolf, E., *Principles of optics*, 5th edition, chapter VIII, 8.8., Pergamon Press, Oxford, (1975).
- [75] Landau, L. D., Lifshitz, E. M., *Theory of elasticity*, Pergamon Press, Terrytown, New York, (1959).
- [76] Hamilton, M. F., Nonlinear wave propagation in mechanics, AMD-77, *The American Society of Mechanical Engineers*, New York, (1986).

- [77] Solodov, I. Yu., Asainov, A. F., Len, K. S., "Nonlinear SAW reflection: experimental evidence and NDE applications", *Ultrasonics*, 31, N2, (1993), pp. 91-96.
- [78] Smith, R. A., Jones, L. D., Zeqiri, B., Hodnett, M., "Non-linear propagation in water and its effects on NDT", CP497, *Non-destructive characterization of materials IX*, edited by Green Jr., R. E., American Institute of Physics, (1999), pp. 522-527.
- [79] Bjørnø, L., "Forty years of non-linear ultrasound", *Ultrasonics International UI01*, July 3-5, Delft, Ultrasonics, Vol. 40, No. 1-8, (2001), pp. 11-17.
- [80] Thurston, R. N., Shapiro, M. J., "Interpretation of Ultrasonic Experiments on Finite-Amplitude Waves", *J. Acoust. Soc. Am.*, 41, (1967), pp. 1112-1125.
- [81] Bacon, D. R., "Finite amplitude distortion of the pulsed fields used in diagnostic ultrasound", *Ultrasound in Med & Bio*, 10, (1984), pp. 189-195.
- [82] Zarembo, L. K., Krasilnikov, V. A., *Introduction to nonlinear acoustics*, Nauka, Moscow, (1966).
- [83] Bronstein, I. N., Semendjajew, K. A., *Taschenbuch der Mathematik*, Verlag Harri Deutsch, Thun, (1989).
- [84] Beyer, R. T., *Non-linear acoustics*, Naval Sea System command, Washington DC, (1974).
- [85] Solodov, I. Yu., "Ultrasonics of non-linear contacts: propagation, reflection and NDE-applications", *Ultrasonics*, 36, (1998), pp. 383-390.
- [86] Solodov, I., Yu., "CAN: an example of nonclassical acoustic nonlinearity in solids", *Ultrasonics International UI01*, July 3-5, Delft, Ultrasonics, Vol. 40, No. 1-8, (2001), pp. 621-625.
- [87] Ballad, E. M., Korshak, B. A., Solodov, I. Yu., Krohn, N., Busse, G., "Local non-linear and parametric effects for non-bonded contacts in solids", *16th International Symposium on Nonlinear Acoustics*, 19-23 August 2002, Moscow, Russia, (2002), forthcoming.
- [88] Mason, W. P., McSkimin, H. J., Shockley, W., "Ultrasonic observations of twinning in tin", *Journal of Physical Review*, 73, (1948), pp. 1213-1214.
- [89] Kaiser, J., *Untersuchungen ueber das Auftreten von Geraeuschen beim Zugversuch*, Ph.D.-thesis, Technische Hochschule Muenchen, (1950).

- [90] Finlayson, R. D., Friesel, M., Carlos, M., Cole, P., Lenain, J. C., "Health Monitoring of Aerospace Structures with Acoustic Emission and Acousto-Ultrasonics", <http://www.ndt.net/article/wcndt00/papers/idn755/idn755.htm>
- [91] Grosse, C., Motz, M., Luetze, S., Bidlingmaier, T., Reinhardt, H. W., "Neue Methoden bei der Anwendung der Schallemissionsanalyse", DACH-Jahrestagung, Innsbruck, May 2000, *DGZfP-Berichtsband*, 73, (2000), pp. 223-230.
- [92] N. N., DIN EN 1330-4, *Non-destructive testing-Terminology-Part 4: Terms used in ultrasonic testing; Trilingual version*, DIN Deutsches Institut fuer Normung e.V., Beuth Verlag GmbH, Berlin, (2000).
- [93] Deutsch, V., Platte, M., Vogt, M., *Ultraschallpruefung- Grundlagen und industrielle Anwendungen*, Springer-Verlag, Berlin, Heidelberg, (1997).
- [94] Split, G., "New Applications for Dry-Contact Probes", *Proceedings of the 4th European Conference on Non-Destructive Testing*, (1987), pp. 2300-2304.
- [95] Roye, W., Manthly, S., "Die Ultraschallpruefung von Schweißverbindungen im Automobilbau", DGZfP-Jahrestagung Berlin, 21. - 23.05. 01, *DGZfP*, 75, (2001), CD-ROM.
- [96] Hutchins, D. A., "Ultrasonic generation by pulsed lasers", *Physical Acoustics*, Vol. 18, Mason, W.P. and Thurston, R.N., eds., New York: Academic, (1988), pp. 21-123.
- [97] Corbel, C., Guillois, F., Royer, D., Fink, M. A., De Mol R., "Laser-generated elastic waves in carbon-epoxy composite", *IEEE Transactions on Ultrasonics, Ferroelectrics, and Frequency Control*, Vol. 40, No. 6, (1993), pp. 710-716.
- [98] Stratoudaki, T., Edwards, C., Dixon, S., Palmer, S. B., "Advances in laser based ultrasound in carbon fibre reinforced composites for aircraft inspection", *8th ECNDT*, Barcelona, (2002), CD-ROM.
- [99] Berner, K., Kugler, J., "Einfache Pruefanlagen fuer eine 100 % Fehleranzeigewahrscheinlichkeit bei der Ultraschall-Flaechenpruefung von Blechen und Baendern", *Materialpruefung*, 15, No. 2, (1973), pp. 43-49.
- [100] Thoma, C., Paassen, H., Moeller P., "Automatische Ultraschallpruefung von Schienen mittels Freiwasserstrahlankopplung im Produktionsfluss", *Berichtsband DGZfP-Jahrestagung*, (1995), pp. 279-286.

- [101] Hillger, W., von Wachter, F. K., "Ultraschallpruefung an Faserverbundkunststoffen – Grundlagen, Methoden der bildhaften Darstellung und Ergebnisse", *Mat.-wiss. u. Werkstofftech.*, 22, (1991), pp. 217-224.
- [102] Diener, L., Wu, D., Steegmueller, R., Busse, G., "Non-destructive evaluation of fibre orientation", Van Hemelrijck, D., Anastassopoulos, A. (Publ.), *Non-Destructive Testing*, Rotterdam, Brookfield: A.A., Balkema, (1996), pp. 245-249.
- [103] Degrieck, J., "Some possibilities of nondestructive characterisation of composite plates by means of ultrasonic polar scans", Van Hemelrijck, D., Anastassopoulos, A. (Publ.), *Non-Destructive Testing*, Rotterdam, Brookfield: A.A., Balkema, (1996), pp. 225-235.
- [104] Schuetz, J., *Akustische Anisotropie und Doppelbrechung bei kurzglasfaser-verstaerktem Polypropylen*, Studienarbeit, Institut fuer Kunststoffpruefung und Kunststoffkunde, Universitaet Stuttgart, (2001).
- [105] Grandia, W. A., Fortunko, C. M., "NDE Applications of Air-Coupled Ultrasonic Transducers", *IEEE International Ultrasonics Symposium*, Seattle, Washington, November 7-10, Proceedings, Vol. 1, (1995), pp. 697-709.
- [106] Bass, H. E., Sunderland, L. C., Percy, J., Evans, L., "Absorption of Sound in the Atmosphere", *Phys. Acoust.*, Vol.17, Academic Press, New York, (1984), pp. 145-232.
- [107] Bass, H. E., Sunderland, L. C., Zuckerwar, A. J., "Atmospheric Absorption of Sound: Update", *JASA*, 88(8), (1990), pp. 2019-2021.
- [108] Bass, H. E., Sunderland, L. C., Zuckerwar, A. J., "Atmospheric Absorption of Sound: Further Developments", *JASA*, 97(1), (1995), pp. 680-683.
- [109] N. N., *Sonda-007C[®] - The AIRSCAN[®] - Digital Ultrasonic Air Coupled Test Instrument*, brochure, QMI, Quality Material Inspection, INC, Costa Mesa, CA 92627, USA, (undated).
- [110] N. N., *Non-contact Ultrasound – A secondWave for a defect free world, brochure*, SecondWave Systems, Bouldsburg, PA 16827, USA, (undated).
- [111] N. N., *AirTech 4000 – Non-Contact Ultrasonic Imaging Technique*, brochure, Ing. Buero Dr. W. Hillger, 38110 Braunschweig, Germany, (undated).

- [112] Kuhl, W., Schodder, G. R., Schroeder, F. K., "Condenser transmitter and microphones with solid dielectric for airborne ultrasonics", *Acustica*, 4, (1954), pp. 519-532.
- [113] Hutchins, D. A., Schindel, D. W., "Advances in non-contact and air-coupled transducers", *Ultrasonic Symposium*, (1994), pp. 1245-1254.
- [114] McIntyre, C. S., Hutchins, D. A., Billson, D. R., Gregory, C., "Gas-coupled ultrasonic capacitance transducers at high pressure", *INSIDE*, 41, No. 2, (1999), pp. 80-86.
- [115] Haller, M. I., Khuri-Yakub, B. T., "A Surface Micromachined Electrostatic Ultrasonic Air Transducer", *Ultrasonic Symposium*, (1994), pp. 1241-1244.
- [116] Newnham, R. E., et al., "Composite piezoelectric transducers", *Mater. Eng.*, Vol. 2, (1980), pp. 93-106.
- [117] Gebhardt, W., "Airborne Ultrasonic Probes: Design, Fabrication, Application", *Proc. 7th ECNDT*, Vol. 3, Broendby, (1998), pp. 3098-3105.
- [118] Hayward, G., Gachagan, A., "An evaluation of 1-3 connectivity composite transducers for air-coupled ultrasonic applications", *J. Acoust. Soc. Am.*, 99, No. 4, (1996), pp. 2148-2157.
- [119] Splitt, G., "Piezocomposite Transducers- a Milestone for Ultrasonic Testing", *INSIGHT*, Vol. 40, No. 11, (1998), pp. 760-763.
- [120] Buckley, J., "Principles and applications of air-coupled ultrasonics", *INSIGHT*, 40, No. 11, (1998), pp. 755-759.
- [121] <http://www.ndt.net/article/dgzfp01/papers/p47/p47.htm>
- [122] Sandmeier, K. J., *Reflex - Programm zur Verarbeitung von seismischer, akustischer oder elektromagnetischer Reflexions- und Transmissionsdaten-V4*, scientific software development, Zipser Strasse 1, D-76227 Karlsruhe, (1993-1997).
- [123] Sandmeier, K. J., *ReflexW - Program for processing and interpretation of reflection and transmission data*, scientific software development, Zipser Strasse 1, D-76227 Karlsruhe, (1993-1999).
- [124] Bucur V., *Non-destructive characterization and imaging of wood*, Springer Verlag, Heidelberg, (forthcoming).
- [125] Klingsch, W.; Neum, U., "Zerstoerungsfreie Lokalisierung aeußerlich nicht sichtbarer Holzschaedigungen mittels Ultraschall", *Bauen mit Holz*, 6, (1989), pp. 421-423.

- [126] Steiger, R., "Festigkeitsortierung von Kantholz mittels Ultraschall", *Holzfor- schung und Holzverwertung*, Nr. 2, (1991), pp. 40-46.
- [127] Navi, P., Forêt, G., Dounau, D., Hue, C., "Experimental observations of mi- crostructural influences on the mechanics of wood cell bundles in tension", *Third Joint ASCE/ASME Mechanics Conf.*, University of California, San Diego, (1994), pp. 441-449.
- [128] <http://www.lht.fh-hildesheim.de/zfwf.html>.
- [129] Stoessel, R., Krohn, N., Busse, G., "Measurements with Air-Coupled Ultra- sound", *7th International Congress on Sound and Vibration*, July 4-7, Gar- misch-Partenkirchen, Proceedings, (2000), pp. II-795-802.
- [130] Berglind, H., Dillenz, A., "Detection of glue deficiency in laminated wood with thermography", *12th International Symposium on Nondestructive Testing of Wood*, Hungary, Sopron, 13-15 September 2000, The e-Journal of Non- destructive Testing - ISSN: 1435-4934, Issue Vol. 6 No. 3, <http://www.ndt.net/article/v06n03/berglind/berglind.htm>, (2001).
- [131] Stoessel, R., Dillenz, A., Krohn, N., Busse, G., "Defectselektive Abbildungs- Verfahren", *Materialpruefung*, Jahrg. 42, (2000), pp.38-44.
- [132] Pfaff, H., *Nichtlinearer luftgekoppelter Ultraschall zur Charakterisierung von Schaedigungsverläufen in faserverstaerkten Polymeren*, Diploma, Institut fuer Kunststoffpruefung und Kunststoffkunde, Universitaet Stuttgart, (2002).
- [133] Dillenz, A., Zweschper, T., Busse, G., "Burst phase angle thermography with elastic waves", *Thermosense 2002*, 1-5 April, Orlando, Florida, USA, (2002), forthcoming.
- [134] Geisse, D., Nixdorf, K., Busse, G., "Cure monitoring of thin adhesive layers", *5th International Congress on Sound and Vibration*, University of Adelaide, December 15th – 18th, (1997), CD-ROM.
- [135] Martin, B. G., "Monitoring the Composite Cure Cycle by Dielectric Analysis" *Materials Evaluation*, 34, (1976), pp. 49-54.
- [136] Hunt, B. J., James, M. I., *Polymer Characterisation*, Blackie Academic & Professional, London, (1993).
- [137] Assmann, W., Delpy, U., "Acoustic emission of epoxy resins during their cur- ing process", report, Institut fuer Kunststoffpruefung und Kunststoffkunde, Universitaet Stuttgart, (1988).

- [138] Geisse, D., *Charakterisierung der Vernetzung duenner Epoxidharzschichten und ihrer Schaedigungsmechanismen in Metallklebeverbindungen*, Ph.D.-thesis, Fakultae 13, Universitaet Stuttgart, (1997).
- [139] Rohklin, S. I., Lewis, D. K., Graff, K. F., Adler, L., "Real-time study of frequency dependence of attenuation and velocity of ultrasonic waves during the curing reaction of epoxy resin", *Journal of the Acoustical Society of America*, 79 (6), (1986), pp. 1786-1793.
- [140] Alig, I., Haeussler, K. G., Nancke, K., Taenzer, W., Wartewig, S., "Ultraschalluntersuchungen zur Bildung von diolmodifizierten Epoxidharznetzwerken", *Acta Polymerica*, 40, (1989), pp. 508-513.
- [141] Nancke, K., *Ultraschalluntersuchungen an vernetzenden Epoxidharzen*, Ph.D.-thesis, TH Leuna-Merseburg, Germany, (1991).
- [142] Vogt, T., Lowe J. S., Cawley, P., "Cure monitoring using ultrasound guided waves in wires", *Review of Progress in QNDE*, 20, Eds. D. O. Thompson, D. E. Chimenti, American Institute of Physics, (2001), pp. 1642-1649.
- [143] Doering, J., Bartusch, J., McHugh, J., Stark, W., "Contribution to Ultrasound Cure Control for Composite Manufacturing", *15th World Conference on Non-Destructive Testing*, Rome, (Italy) 15-21 October, <http://www.ndt.net/article/wcndt00/papers/idn482/idn482.htm>, (2000).
- [144] Fassbender, S. U., Arnold, W., "Measurement of adhesion strength of bonds using non-linear ultrasound", *Review of Progress in QNDE*, 15B, Eds. D. O. Thompson, D. E. Chimenti, Plenum Press N.Y., (1996), pp. 1321-1328.
- [145] Liu, G., Qu, J., Jacobs, L.J., Li, J., "Characterizing the curing of adhesive joints by non-linear ultrasonic technique", *Review of Progress in QNDE*, 18, Eds. D. O. Thompson, D. E. Chimenti, Plenum Press N.Y., (1999), pp. 2191-2199.
- [146] Robinson, A. M., Drinkwater, B. W., "Extending the frequency range of the wheel probe-application to adhesive bond inspection", *Review of Progress in QNDE*, 20, Eds. D. O. Thompson, D. E. Chimenti, American Institute of Physics, (2001), pp. 883-890.
- [147] Krohn, N., Geiße, D., Nixdorf, K., "Charakterisierung der Vernetzung polymerer Harze durch Resonanzmethoden", *16. Stuttgarter Kunststoffkolloquium*, 10.-11.03.1999, Artikel 4.2, (1999).

- [148] Hillger, W., Dietz, M., May, B., "Ultraschallpruefungen beruehrungslos mit Ankopplung ueber Luft – Illusion oder schon bald Realitaet?", *Berichtsband 63.1 der Jahrestagung DGZfP*, (1998), pp. 241-249.
- [149] Buckley, J., Loertscher, H. P., "Frequency Considerations in Air-Coupled Ultrasonic Inspection", *BINDT Conference*, 16th September, (1999), pp. 405-410.
- [150] Loertscher, H. P., Grandia, B., Strycek, J., Grandia, W. A., "Airscan Transducers, Techniques and Applications", reprint, online workshop on transducers, UT-online journal (1996).
- [151] Stoessel, R., Krohn, N., Busse, G., "Luftultraschalluntersuchungen an nichtmetallischen Werkstoffen", DGZfP Jahrestagung Berlin, *Berichtsband 75-CD*,(2001), V25.
- [152] Busse, G., *Keramische Werkstoffe*, Vorlesungsskript WS 94/95, Universitaet Stuttgart, (2002).
- [153] N. N., *Keramische Verbundstrukturen, Extremer Leichtbau mit Materialien aus der Raumfahrt*, brochure, Deutsches Zentrum für Luft- und Raumfahrt e.V., Stuttgart, (undated).
- [154] N. N., *Wiedereintrittstechnologie*, brochure, Deutsches Zentrum für Luft- und Raumfahrt e.V. Stuttgart, (undated).
- [155] Muehlratzer, A., Dogigli, M., „Steuerklappen aus faserverstärktem SiC fuer Wiedereintrittsraumfahrzeuge“, *Verbundwerkstoffe und Werkstoffverbunde*, Wiley-VCH, Weinheim, (2001), pp. 252-261.
- [156] N. N., *Vom Hitzeschutz zur Hochleistungsbremse*, brochure, Deutsches Zentrum für Luft- und Raumfahrt e.V., (1998).
- [157] Stoessel, R., Krohn, N., Pfeleiderer, K., Busse, G., "Air-Coupled Ultrasound as a tool for new NDE-applications", *27th Review of Progress in Quantitative Non-Destructive Evaluation (QNDE)*, Ames, Iowa, (2000), pp. 1592-1599.
- [158] N. N., *Faserverstaerkte Hochleistungskeramik C/C-SiC*, brochure, Deutsches Zentrum für Luft- und Raumfahrt e.V., Stuttgart, (undated).
- [159] Barrett, R., "Introduction to Adaptive Aerostructures", autumn course, Oct. 12th – 13th, Stuttgart, (1998).

- [160] Toulmay, F., Kloeppe, V., Lorin, F., Enekl, B., Gaffieri, J., "Active Blade Flaps - The needs and current capabilities", *American Helicopter Society 57th Annual Forum*, Washington DC, (2001).
- [161] Martin, W., "Adaptive Strukturen für die Luft- und Raumfahrt", *8. Nationales Symposium SAMPE Deutschland*, Kaiserslautern, (2002).
- [162] Barrett, R., *Aerospace Smart Structures the Coming Revolution*, paper presented at the *34th Aerospace Sciences Meeting and Exhibit*, Reno, (1996).
- [163] Krohn, N., Duerr, J., Dillenz, A., Doettinger, C., Luetze, S., Nixdorf, K., Herold-Schmidt, U., Busse, G., "NDT of smart structures", *2nd International Conference on Emerging Technologies in NDT*, Athens, 24-26 May, Balkema, Rotterdam, (1999), pp. 187-191.
- [164] Stoessel, R., Krohn, N., Pfeleiderer, K., Busse, G., "Air-coupled ultrasound inspection of various materials", *Ultrasonics International UI 01*, July 3-5, Delft, Ultrasonics, Vol. 40, No. 1-8, (2001), pp. 159-163.
- [165] Wierach, P., Struck, H., Sachau, D., "Strukturkonforme Integration von Piezokeramiken in Faserverbundwerkstoffe", *Verbundwerkstoffe und Werkstoffverbunde*, Wiley-VCH, Weinheim, (1999), pp. 576-581.
- [166] Pohl, J., Mook, G., Michel, F., Benziger, T., "Adaptive Werkstoffsysteme- Der Werkstoff sendet ZfP-Signale", *Materialpruefung*, 41, (1999), pp. 424-428.
- [167] Pfeleiderer, K., *Zerstoerungsfreie Pruefung adaptiver Strukturen mit variabler Aktor - Faserverbundwerkstoff – Kopplung*, Diploma, Institut fuer Kunststoffpruefung und Kunststoffkunde, Universitaet Stuttgart, (2000).